Dipl.Ing. Peter Neugebauer, BSc

Advanced Crystallization and Crystal Engineering in Continuously Operated Tubular Crystallizers

DISSERTATION

Zur Erlangung des akademischen Grades

Doktor der technischen Wissenschaften

Eingereicht an der

Technischen Universität Graz

Betreuer

Univ.-Prof. Dipl.Ing. Dr. techn. Johannes Khinast

Institut für Prozess- und Partikeltechnik

Peter Neugebauer

Advanced Crystallization and Crystal Engineering
in Continuously Operated Tubular Crystallizers

Dissertation

First assessor and supervisor
Univ.-Prof. Dipl.-Ing. Dr.techn. Johannes G. Khinast
Institute for Process and Particle Engineering
Graz University of Technology
and
Research Center Pharmaceutical Engineering GmbH

Second assessor
Prof. Dr. Jan Sefcik
Department of Chemical and Process Engineering
University of Strathclyde, Glasgow

STATUTORY DECLARATION

I declare that I have authored this thesis independently, that I have not used other than the declared sources/resources, and that I have explicitly marked all material which has been quoted either literally or by content from the used sources.

March, 2018 ……..

Dipl.-Ing. Peter Neugebauer, BSc

EIDESSTATTLICHE ERKLÄRUNG

Ich erkläre an Eides statt, dass ich die vorliegende Arbeit selbstständig verfasst, andere als die angegebenen Quellen/Hilfsmittel nicht benutzt, und die den benutzten Quellen wörtlich und inhaltlich entnommenen Stellen als solche kenntlich gemacht habe. Das in TUGRAZonline hochgeladene Dokument ist mit der vorliegenden Dissertation identisch.

März, 2018 ……..

Dipl.-Ing. Peter Neugebauer, BSc

Abstract

The focus of this thesis was to develop methods for advanced crystal engineering via next-generation continuous flow technology, based on previous work on tubular crystallization. Tubular reactors (typically with an inner diameter of < 1cm) can be used as continuously operated crystallizers and have a wide range of applications for the crystallization from a solution. In the first part of this thesis a novel tubular crystallizer for a continuous and possibly large-scale production of protein crystals is presented. Due to the negative impact of shear forces on the growth rate of protein crystals this work comprises initial studies on particle transport limitations while employing very low flow rates. In our system it is shown that the low shear forces in the reactor contribute to relatively high average growth rates.

However, current systems, while making it possible to continuously produce crystalline substances, have not been designed to enable scientists and companies to continuously engineer crystal properties. Thus, in this thesis a novel approach is presented for continuous engineering of crystalline particles, being capable of altering essential properties of starting materials, towards a desired quality attribute. A set-up was designed to operate such a tubular crystallizer in a temperature-cycling mode to facilitate crystal engineering via multiple cycles of growth and dissolution. Building on work about continuous crystallization of proteins the second part of this thesis presents a set-up to tune crystal shape towards a desired form, to realize a continuous process for polymorphism tuning and to demonstrate effective removal of fines from a crystalline sample with broad particle size distribution. Macromolecular properties, such as size and shape, determine the kinetic properties and the ability to handle crystalline material, and are therefore critical for every crystallization process. Compounds that can appear in different polymorphic forms are of high interest for the chemical and pharmaceutical industry due to their different solubility and other relevant properties.

However, processing solid particles in small flow devices remains a challenge, due to fouling of the crystallizer piping or sedimentation of particles, ultimately plugging the tube. To demonstrate how particle transport in a gas-liquid segmented flow is determined by the flow and particle properties, a setup was designed to monitor particle transport via a high-speed camera. Experiments showed that an increase in flow rate can improve particle dispersion within the segments but comes along with an increase in wall film thickness. This allows larger particles to travel between slugs.

Kurzfassung

Der Schwerpunkt dieser Doktoratsarbeit lag auf der Entwicklung von Methoden für kontinuierliche Proteinkristallisation und Kristall-Engineering. Kristallisation aus einer Lösung ist das vorherrschende Verfahren zur Trennung und Reinigung von Stoffen in der chemischen und pharmazeutischen Industrie. Da mehr als 90% aller pharmazeutischen Wirkstoffe im kristallinen Zustand verarbeitet werden, wurde ein experimenteller Aufbau zur gezielten Veränderung der Partikeleigenschaften von kristallinen Substanzen entwickelt. Zu den Qualitätsmerkmalen von Kristallen, die in der vorliegenden Arbeit behandelt wurden, gehören die Größe und Größenverteilung, die maßgeblich für die Fließeigenschaften des Pulvers verantwortlich sind, die polymorphe Form und der äußere Habitus der Kristalle, der unter anderem ihre Auflösungsgeschwindigkeit beeinflusst.

Basierend auf bisherigen Arbeiten bzgl. kontinuierlicher Kristallisation wurde ein neuartiger Aufbau entwickelt, der Kristall-Engineering durch Zyklen von Kristallwachstum und -auflösung ermöglicht. Der schlauchförmige Kristallisator wurde dazu in Schleifen aufgewickelt, die zwei Wasserbäder durchlaufen. Durch das Passieren dieser beiden Wasserbäder wurde eine kristalline Suspension abwechselnd und in definierter Weise gekühlt und erwärmt, wobei die Temperaturdifferenz und die Verweilzeit in jedem Bad exakt angepasst werden konnten. Im erwärmten Kompartiment wurde die Suspension untersättigt und Kristalle begannen sich aufzulösen. Die Rekristallisation fand auf den verbleibenden Kristallen statt, als sich die Suspension im gekühlten Abschnitt des Zyklus‘ befand.

Ein solcher schlauchförmiger Kristallisator, der eine große Anzahl an Temperaturzyklen in kurzer Zeit ermöglicht, bietet gegenüber einem entsprechenden diskontinuierlichen Prozessen einige Vorteile: (1) Die präzise Steuerung der Übersättigung ist der Schlüssel zu einer effektiven Prozesskontrolle. Dies kann durch die Nutzung der hohen Wärmeübertragungsraten des Setups erreicht werden. (2) Durch die Fähigkeit sehr rasch zwischen Über- und Untersättigung zu wechseln kann der Prozess gegenüber diskontinuierlichen Verfahren immens beschleunigt werden. (3) Die Kristallisation erfolgt ohne bewegliche Teile, wodurch Kristallbruch und Abrieb minimiert werden. Die experimentellen Arbeiten wurden von umfassenden Simulationen begleitet, um das Design des Kristallisators effizient zu unterstützen.

Die Verwendung von schlauchförmigen Kristallisatoren mit geringem Durchmesser wird oftmals durch Sedimentation von Kristallen und dadurch hervorgerufenes Verstopfen des Schlauches beschränkt. Ein weiteres Ziel dieser Arbeit war daher die Charakterisierung des Transportes von Partikeln.

Danksagung

Peter Neugebauer

Graz, März 2018

Contents

1 Introduction[a]

1.1 *Crystal Engineering*

The focus of this thesis was to develop methods for advanced crystal engineering via next-generation continuous flow technology. Crystal engineering is the ability to rationally tune the physio-chemical properties of crystalline matter. Specifically, crystal engineering is "the understanding of intermolecular interactions in the context of crystal packing and the utilization of such understanding in the design of new solids with desired physical and chemical properties."[1] This involves the arrangement of the crystal's building blocks, i.e., atoms or molecules. In addition, the polymorphic state, the presence of defects and the size and shape of individual crystals (habit) are concerned. While the lattice structure and associated defects determine the crystal's thermodynamic properties, macromolecular properties, such as size and shape, determine the kinetic properties and the ability to handle the crystalline material. Understanding interactions at the molecular level, as well as knowledge about process parameters and performance is essential in engineering tailored product particles, as condensed in Figure 1.

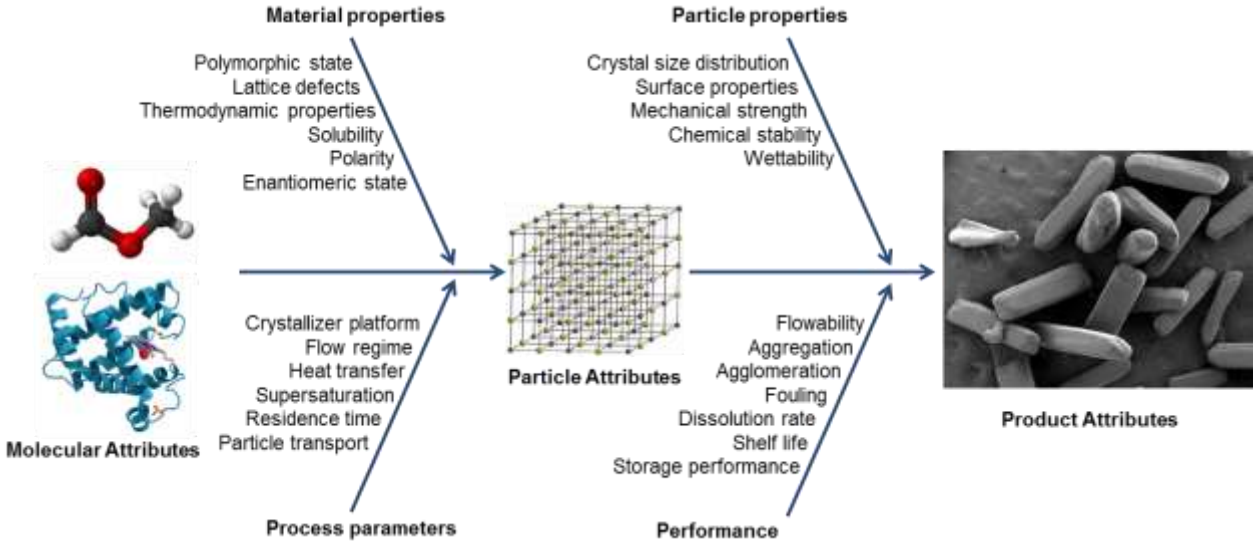

Figure 1: Process parameters and material attributes are critical for the performance of the final crystalline product

[a] The chapter 1 of this work is to some extend based on the FWF proposal Continuous Crystal Engineering in an Advanced Plug-Flow Crystallizer System' by Neugebauer, Khinast and Gruber-Wölfler. It has to be acknowledged that all parts included in this thesis were written by the author of this thesis.

Presently, many new drugs on the market and in the drug pipeline have a poor solubility, which is a significant challenge for drug delivery.[2] While the solubility depends on the crystalline structure (including amorphous forms which usually provide the highest solubility), the dissolution rate is also affected by the crystal size distribution (CSD), i.e., the total surface area of the crystalline phase, and crystal shape,[3] since different shapes expose different crystal faces. The shape of the crystal and the fraction of different faces are described by the crystal habit. It is well known that different faces dissolve or grow at different rates. A typical example is Celecoxib (trade name: Celebrex®), which is a nonsteroidal anti-inflammatory drug (NSAID). Two crystal habits of this BCS (Biopharmaceutics Classification System) class-II drug molecule (i.e., poor solubility, high permeability), obtained by controlled crystallization, differ significantly in terms of dissolution kinetics and wettability due to the relative exposure of the different crystalline faces to the aqueous environment of the intestinal tract.[4] Thus, engineering of the crystal form, polymorphic state, and crystal habit has significant impact on the performance of drugs *in vitro*.

Tight supersaturation control is not trivial and traditional batch crystallizers quickly reach their operational limits, if high supersaturation levels and rapid changes of the latter are required.[5]

1.2 *Objectives of this Thesis*

In the framework of this thesis the development of a novel tubular crystallizer for continuous production of protein crystals was pursued, using Lysozyme as a model protein. Water baths to fine-tune the temperature and thus the supersaturation promised to be suitable to control nucleation and following crystal growth.

Besides the establishment of a robust process for continuous crystallization of proteins, a novel setup was designed to facilitate crystal engineering via multiple cycles of growth and dissolution. Such a tubular crystallizer was supposed to offer several advantages over the corresponding processes in batch: (1) Precise control of the supersaturation is key for rational control of the crystallization and the material transformation. This can be achieved by utilizing the high heat transfer rates in tubular crystallizers. (2) Crystallization will occur in the absence of any moving parts and at minimum agitation, thus minimizing complexity, crystal breakage/attrition and undesired secondary nucleation. Particularly concerning particle engineering another advantage can be mentioned for operation in a temperature-cycling mode: (3) High levels of super- and under-saturation, and the ability to switch between them within

seconds allows for rapid dissolution and growth, yet preventing secondary and/or primary nucleation.

Such a setup was planned to be used to tune the physio-chemical properties of crystalline matter in a minimum of time without using any additives. Targeting a simple setup, crystal engineering should be made possible via a continuous process with a considerable volume (~litres per hour) and residence times in the range of several minutes. Moreover, the critical processing issues, such as fouling and pipe plugging were planned to be addressed by applying novel approaches.

Building on preliminary experiments and modeling efforts this thesis aimed to achieve the following objectives:

- To address the topic of **blocking due to particle accumulation, incrustation and fouling in tubular crystallizer setups**. Lab-scale experiments, as well as industrial applications using tubular crystallizers, have shown that such systems are susceptible to blocking as particles tend to settle and accumulate inside the tube. Furthermore, solutes start to deposit on tube walls in long-term experiments, limiting the continuous production time and necessitating periodic cleaning. It was intended to investigate particle transport in tubular reactors with inner diameters in the mm-range to find new ways for minimizing fouling via gas-liquid segmented flow. Effects of flow rates, solvent type (density, viscosity, polarity, e.a.) and dispersed crystals' properties should be investigated.

- To demonstrate **effective removal of fines** from a crystalline sample with broad particle size distribution. A setup is presented generating compartments which allow for alternating crystal growth and dissolution. Fine material up to a desired size is dissolved completely during passage through such a compartment at elevated temperature. In the subsequent cooling compartment remaining crystalline material grows at the expense of dissolved particles, thereby narrowing the PSD.

- To use the setup for cycles of growth and dissolution intend to **tune crystal shape** towards a desired final form. Controlling crystal shape via this approach can be achieved via additives or solvent selection during growth of crystals from solution, as well as via supersaturation control. Pharmaceutically relevant model substances crystallizing in an unfavorable shape is a common obstacle during formulation. In this thesis tailoring particle shapes should be addressed using the model substance acetylsalicylic acid. Starting with crystals showing an undesired habit (i.e. needles, rods), crystals of a more compact form (platelike or cubic) were targeted to offer

superior handling properties, such as enhanced flowability and better processability (i.e., tabletability) or altered dissolution behavior.

- Due to the supersaturation-dependence of the dissolution rates, growth rates, and nucleation rates (including secondary nucleation), temperature cycling can be utilized to control solvent-mediated (polymorphic) transformation (SMT). As such a continuous process employing cycles of crystal growth and dissolution provides a powerful tool for speeding up a polymorphic transition under highly controlled process conditions. Since the crystal structures of the polymorphs of D-Mannitol are known and their difference in free energy and solubility have extensively been reported it was decided to choose it as a model substance. Because SMT proceeds via nucleation rather large temperature differences were targeted to promote nucleation events which is avoided for the fines removal and shape tuning studies.
- To develop tools for **control and analysis (inline and online)** of the tubular crystallizer, via particle size analysis in real time and advanced process control methods.

This thesis comprises work on continuous tubular crystallization and crystal engineering of more than three years. However, many problems need to be solved before the technology can be deployed in industry, and several novel applications remain to be developed and pioneered. This thesis addresses some of these relevant factors but is not meant to be a comprehensive essay of continuous crystallization. Promising ideas were realized in small-scale setting, providing the ability for basic research to be applied in industry.

2 Continuous Crystallization of Proteins in a Tubular Plug-Flow Crystallizer[b]

Abstract. Protein crystals have many important applications in many fields, including pharmaceutics. Being more stable than other formulations, and having a high degree of purity and bioavailability, they are especially promising in the area of drug delivery. In this contribution, the development of a continuously operated tubular crystallizer for the production of protein crystals has been described. Using the model enzyme lysozyme, we successfully generated product particles ranging between 15 – 40 µm in the size. At the reactor inlet, a protein solution was mixed with a crystallization agent solution to create high supersaturations required for nucleation. Along the tube, supersaturation was controlled using water baths that divided the crystallizer into a nucleation zone and a growth zone. Low flow rates minimized the effect of shear forces that may impede crystal growth. Simultaneously, a slug flow was implemented to ensure crystal transport through the reactor and to reduce the residence time distribution.

[b] This chapter is based on a journal article by Neugebauer et al. in Crystal Growth and Design in 2015.

2.1 *Introduction*

In the past, protein crystallization was mainly used for protein structure determination. To date, about 90% of all protein structures have been determined via employing protein crystals for X-ray crystallography.[6] Based on their 3D structure, protein crystals are considered fragile since they lack a spherical interaction field present in small molecules and rather depend on attractive forces of specifically arranged amino acid residues.[7] Nevertheless, the protein crystallization has become increasingly important and new applications have been developed, for example, purification of single proteins from complex protein extracts. In this context, crystallization can partly replace other purification techniques, such as preparative chromatography which usually is more expensive and time-consuming.[8] In contrast to X-ray crystallography, here the production of large crystals free from lattice imperfections is no longer required, but focus lies on the separation from dissolved impurities in a rapid and economic manner.[9]

Other applications include the use as biocatalysts, where protein crystals in the form of cross-linked enzyme crystals (CLECs) are often more suitable than soluble or conventionally immobilized enzymes since they have a high activity-to-volume ratio. Moreover, stability is improved with respect to various denaturants (e.g., heat, mechanical shear forces, organic solvents and pressure).[10] Cross-linkers, such as glutaraldehyde, prevent the crystals from re-dissolving and make them easy to handle and recyclable.[11]

Significant research efforts have been devoted to protein crystals used in drug delivery. In this field, their mechanical stability and other favorable characteristics enable efficient delivery options beyond intravenous infusion. The crystalline state offers protection from proteolytic enzymes, and thus, may increase bioavailability. Proteins may be used directly in inhalation therapy, as the lung can be accessed for the drug delivery of large molecules, without the need for parenteral routes. Dissolution characteristics are more predictable and sustained release may be obtained.[12] Moreover, they offer high purity, which is essential in applications as pharmaceutical formulations. In addition, based on the high stability, protein crystals greatly facilitate storage and transport, being another option beyond lyophilization. Pechenov et al.[13] demonstrated that crystallized α-amylase incorporated into in situ formable gels remained fully active after 260 days at 4°C, in contrast to amorphous formulations that lost 43-45% of their activity. Similar results for protein crystals were reported earlier.[14,15] These findings suggest that they can be used in injectable controlled-release systems, offering a number of

advantages (e.g., convenience of use due to reduced number of applications, simplicity of system fabrication and improved process economics).[13] As the most concentrated form of protein, the crystalline state is considered to be very effective when high drug doses have to be applied to a certain delivery site.[16]

Based on the rising demand for protein crystals, large-scale crystallization processes are increasingly important, particularly as the range of biotechnologically-produced proteins is expanding. However, a systematic understanding of large-scale protein crystallization processes, especially with respect to scale-up, control and optimization, is scarce. In general, scale-up of crystallization processes is not straightforward. This is even more true for protein crystals, as their structure and quality is highly dependent on the process conditions. Impeller tip speed, mean power input and agitation rate are typically used as criteria for scale-up in technical-scale stirred batch crystallizers.[17] However, it is well known that for all scale-up methods, mixing times, maximum shear rates and local dissipation rates of turbulence vary vastly between small and large-scale systems. For mechanically fragile systems (such as proteins) this is problematic as in order to reach the same macro-mixing, much higher maximum shear rates are realized in the impeller zone.

Batch processes range from mL-vessels in the laboratory to crystallizers with volumes in the range of cubic meters. Several studies with baffled/unbaffled and agitated/non-agitated vessels reported varying results concerning the growth rate, crystal habit and average crystal size. High stirrer energy input and higher shear forces needed to disperse the particles and to eliminate the diffusion limitation proved to be detrimental for the formation of large protein crystals.[18,19,20] Most likely thereby the attachment of growth units to the surface of crystals is hindered[19] and crystal breakage may be initiated.

Over the last three decades, numerous studies have addressed the impact of shear forces on the growth rate of protein crystals. Even at very low fluid velocities, crystal growth rates have been shown to be influenced considerably. Durbin and Feher[21] were among the first to publish data on lysozyme crystals grown in a flow system. Here, convection currents were generated by recirculation of a lysozyme solution through a glass crystallization cell with continuous filtration using a peristaltic pump. With liquid velocities ranging between 0.04 mm/s and 0.6 mm/s inside the crystallization cell they reported constant growth rates. Contrasting results were obtained by Pusey et al.[18] who introduced crystals of lysozyme of <20 µm into a

convective plume flow of lysozyme solution at 0.01-0.05 mm/s and observed a decrease in the growth rate by 90% or more after 8 to 20 h. These findings were confirmed by Nyce et al.[19] who used a closed-loop thermosyphon. Crystals were suspended at the velocity range of 5-15 mm/s, and facets became frosted, i.e., no more growth occurred. The authors suggested that shear forces limited the attachment of growth units. Underlining these conclusions, other authors reported that a weak forced convection had an inhibitory effect on the growth rate of crystals in the size range of 100-300 µm.[22] Vekilov and Rosenberger[20] suspected that the influence of "flow-enhanced transport of growth inhibiting impurities to the interface" was responsible for the decrease in the crystal growth rate. At two supersaturation levels ($\sigma_1 = 1.0$ and $\sigma_2 = 1.4$ with $\sigma = \ln(c/c^*)$), they observed significantly decreased growth rates and step velocities at relative flow velocities of >0.25 mm/s. Thus, in summary even small shear forces and the micro-fluidic environment have significant impact on the growth rate of protein crystals.

The influence of stirrer power input on the crystal size distribution and protein concentration in the supernatant was investigated using small-scale agitated batch crystallizers.[23] By applying a low impeller power input of 12 W/m^3, after more than 40 hours a mean crystal size of ~25 µm was reached, compared to ~20 µm at 640 W/m^3. The yield of the process, however, was not negatively affected by the increased power input. According to the literature, higher stirrer speeds can reduce the onset time of batch crystallization and decrease the formation of crystal agglomerates.[24]

Depending on the NaCl concentration and temperature, the solubility of lysozyme varies drastically, from beyond 100 g/L to close to zero at pH4.6.[25,26] To date, several studies have been published identifying temperature as a crucial parameter for protein crystallization (in addition to control of supersaturation via crystallization agent or pH).[27,28,29,30,31] A series of proteins has shown pronounced susceptibility to temperature regarding crystallization behavior, particularly at low salt concentrations.[29,32,33,34] This suggests its use to alter supersaturation in a rapid and reversible way and offers advantages, such as precise control and constant solution composition.

Based on the previous work of our group,[35,36,37,38] we developed a novel tubular crystallizer for a continuous (and possibly large-scale) production of protein crystals. Lysozyme was used as a model protein. With sodium chloride (NaCl) as a crystallization agent, the temperature

and thus, supersaturation, were fine-tuned via water baths to achieve controlled nucleation followed by crystal growth. Lorber et al.[39] reported that a desired supersaturation can be achieved by modifying different parameters (e.g., temperature, pH, protein and crystallization agent concentration). Thus, for the same supersaturation growth can occur at different rates. Furthermore, they showed that high supersaturation promotes nucleation and that high growth rates were observed at the lowest supersaturation levels. In contrast, Forsythe et al.[40] suggested that impurity effects of commercial lysozyme were hampering crystal growth at low supersaturation levels and stressed the importance of high supersaturation for high growth rates. In our work, the temperature profile in the continuous reactor was designed according to the latter findings.

One advantage of our system is that the supersaturation profile can be easily controlled via the local temperature along the tubular crystallizer. Moreover, support of crystal transport in the crystallizer via a slug flow ensures a narrow residence time distribution. Scale-up is not necessary in such crystallizers as high product quantities can be obtained by installation of parallel tubes and/or running the systems for longer times. Thus, no differences between crystals made in the development phase and during production are expected and surprises during process scale-up are eliminated. Lastly, the setup minimizes shear forces. Several studies (cited above) showed that high shear rates are detrimental for crystal growth. In our system we assume that the low shear forces in our reactor contribute to relatively high average growth rates.

2.2 *Materials and Methods*

Lysozyme from hen egg white was purchased from Sigma-Aldrich, Vienna, Austria (No. 62971). Other chemicals used were of reagent grade. Buffer solution was prepared by dissolving 16 g/L NaCl in deionized (DI) water containing 100 mM of acetate buffer at pH 4.6. Lysozyme was added to the buffer solution to reach a concentration of 100 g/L. The crystallization agent solution was prepared by dissolving 64 g/L NaCl in DI water. Solutions were filtered through a 0.2 µm filter (Rotilabo®, cellulose acetate, Ø 25 mm, sterile, Carl Roth, Karlsruhe, Germany) and filled into syringes (Omnifix® Solo 50 mL, B Braun, Maria Enzersdorf, Austria). A syringe pump (HLL Landgraf, LA-120, Langenhangen, Germany) was used to continuously mix the lysozyme solution and the crystallization agent solution via a Y-fitting (PTFE, d_{in} = 2 mm) located at the inlet of the tubular reactor. Silicone tubing with an inner diameter (d_{in}) of 2.0 mm and an outer diameter of 4.0 mm was obtained from Carl

Roth (Versilic®). Microscope analysis was performed using a Leica DM 4000 microscope together with a Leica DFC 290 camera. Each solution was pumped into the reactor at a flow rate of 0.15 mL/min, resulting in a 1:1 (v/v) mixture with 50 g/L lysozyme, 40 g/L NaCl and 50 mM acetate buffer. These initial concentrations ensured crystallization temperatures to be around room temperature. The overall setup of the continuous crystallizer is schematically shown in Figure 2.

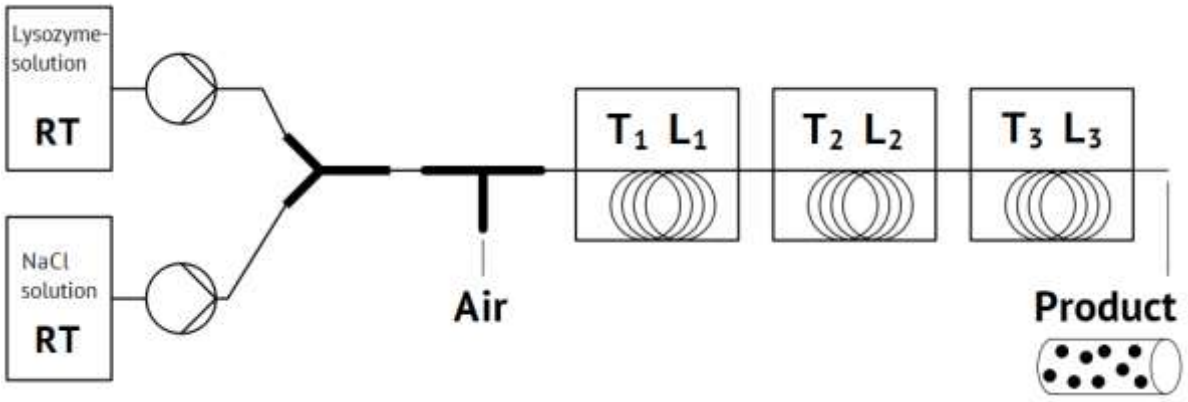

Figure 2: Set-up of the tubular crystallizer (schematic), T = temperature, L = length of tube in the respective water bath, RT = room temperature

A segmented flow was established by introducing air bubbles into the two-phase flow. A T-fitting (PTFE, d_{in} = 2 mm) was placed approximately 20 mm downstream of the mixing point of the lysozyme solution and the crystallization agent solution. Every 15 seconds, an air bubble of ~15 mm^3 was injected into the liquid-solid flow using a 1 mL syringe (Omnifix®-F 1 mL, B Braun), providing a small and reproducible volume. This resulted in bubbles of about 5 mm in length and liquid slugs of 25 mm length (Figure 3). The total volumetric flow rate (liquid + gas) was 0.36 mL/min which equals to a total linear flow rate of 1.9 mm/s.

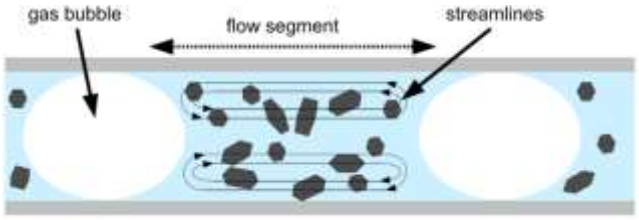

Figure 3: Implementation of the slug flow. Gas bubbles separate the liquid flow into segments to achieve the optimal transport of crystals along the reactor and a narrow residence time distribution (adapted from Besenhard et al.[36])

In the tubular reactor, three sections with different temperatures were selected in order to induce different phenomena, i.e., nucleation in the first section, crystal growth in the second and then final growth to achieve a high yield in the third section. These sections were designed based on solubility data from literature as shown in
Table 1 with lysozyme solubility data at 4% NaCl.

Table 1: Solubility of lysozyme in buffered NaCl solutions from various groups; buffer is NaOAc (sodium acetate)

pH	NaCl [%]	T	NaOAc [M]	Solubility [g/L]	Resource
4.6	4	22.3	0.1	3.68	Forsythe 1999[26]
4.6	4	23.6	0.1	4.22	Forsythe 1999[26]
4.6	4	18.2	0.1	2.30	Forsythe 1999[26]
4.5	4.1	18.0	0.05	4.3	Guilloteau 1992[41]
4.5	4	20.0	0.05	11	Howard 1988[25]
4.5	4	25.0	0.05	11	Howard 1988[25]
4.6	4	22.0	0.1	3.27	Cacioppo 1991[42]
4.6	4	23.0	0.1	3.64	Cacioppo 1991[42]
4.6	4	18.0	0.1	2.15	Cacioppo 1991[42]

Although the concentration of NaOAc-buffer in Table 1 varies between 0.05-0.1 M, which has a significant influence on ionic strength and lysozyme solubility, we could – based on these data – design a supersaturation trajectory for the proposed setup. The concept of our continuously operated tubular crystallizer was to achieve high supersaturation at the inlet in order to induce nucleation in a particle-free solution. Reportedly, the supersaturation barrier for the formation of protein crystal nuclei can be significantly larger than 1 due to their structural complexity.[29] Based on solubility data from Cacioppo et al.[42] and Forsythe et al.,[26] the initial supersaturation of our experiments was chosen to be about S=10. S equals the actual concentration (c) divided by the equilibrium concentration (c*), i.e., S = c/c*. The same

commercial lysozyme product was chosen by Hekmat et al.[43] for vapor diffusion experiments and batch crystallization in agitated ml-scale vessels. By performing a series of experiments they were able to draw a quantitative phase diagram in order to define precipitation curves for different vessel geometries and agitation frequencies. With increasing agitation rates the precipitation boundary moved towards lower supersaturations, thereby reducing the nucleation zone. In their proposed phase diagram our process settings are chosen to be well inside the nucleation zone.

The temperature of the first water bath was determined by the supersaturation ratio (S) required for nucleation (around 10). A reduction of the initial lysozyme concentration by 10% (to 45 g/L) was intended to occur in the first water bath, determining the length of the first section. In the next sections, supersaturation was chosen to be below the critical nucleation level in order to promote growth of nuclei to macroscopic crystals. Accordingly, the supersaturation is reduced from S = 10 at the entrance of the first water bath to S = 8 (values estimated from solubility data, see Table 2) in the second water bath. This was found to minimize further nucleation, leading to optimal growth in the second section of the crystallizer. The temperature in the third water bath was chosen to account for the low lysozyme concentration and to increase crystal growth. A summary of the chosen design parameters is provided in Table 2. A diagram showing the experimentally determined concentration levels and the estimated saturation gradient along the tubular crystallizer is provided in Figure 4.

Table 2: Settings of the tubular crystallizer

	Water bath 1	**Water bath 2**	**Water bath 3**	**Σ**
Temperature [°C]	21.5	22.5	20.0	-
Tube length [m]	3.0	5.0	5.0	13.0
Residence time [min]	26.2	43.6	43.6	113.4

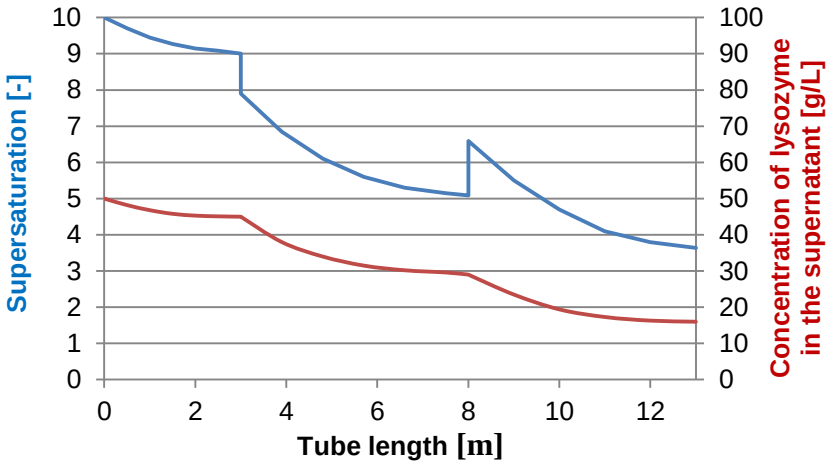

Figure 4: Saturation and concentration gradient along the tubular reactor. Lysozyme concentrations were determined experimentally. Supersaturation was estimated based on the solubility data shown in Table 1.

To obtain good heat transfer and to avoid the formation of folds and creases that may potentially obstruct free particle flow, the reactor tube was loosely coiled on metal cylinders (Ø = 21.5 cm) immersed in the water baths. At the outlet of the crystallizer, samples were collected for analysis. For the microscopic examination samples of the suspension were directly dripped on the microscope slides. The yield of the process was determined via spectrophotometric measurements. Product samples were taken by dripping the product suspension into Eppendorf tubes. Crystals could now be separated from the suspension via centrifugation (15000 g, 20°C, 2 min, centrifuge: Hettich 320R, Tuttlingen, Germany), and the remaining concentration of lysozyme in the supernatant was determined photometrically at 280 nm by comparing it to a lysozyme standard (extinction coefficient A_{280nm} = 2.48).
For every experimental condition five identical experiments were carried out.

2.3 *Results and Discussion*

Yield and crystal size distribution of the continuous crystallization process

The concentrations of lysozyme in the supernatant at the exit of each water bath are shown in Table 3 together with standard deviation between 5 experiments at a total linear flow rate of 1.9 mm/s.

Table 3: Concentrations and estimations of supersaturation at various points in the tubular crystallizer

Location		Concentration [g/L]	Standard deviation of concentration [g/L]	Supersaturation S (estimated)
Water bath A (21.5°C)	inlet	49.9	0.8	10
	outlet	45.1	2.3	9
Water bath B (22.5°C)	inlet	45.1	2.3	7.9
	outlet	29.5	2.9	5
Water bath C (20.0°C)	inlet	29.5	2.9	6.6
	outlet	15.8	4.1	3.6

The yield of the process was calculated by analyzing the concentration of lysozyme at the inflow and outflow. Starting at 49.9 g/L, the concentration in the supernatant dropped to 45.1 g/L after the first water bath (nucleation zone). After the second water bath which had a slightly higher temperature, the concentration dropped to 29.5 g/L. At the outlet of the crystallizer, the final concentration was 15.8 g/L, which corresponds to an overall yield of the process of 68% with a residence time of 113.4 min. Although the differences in operating temperatures in the three zones of the continuous crystallizer may appear small, they are optimal to minimize nucleation in water bath 2 and 3 and to simultaneously guarantee high growth rates throughout the reactor. This was confirmed by microscope analysis when increased numbers of microcrystals obtained during experiments at lower temperature in water bath 2 and 3, respectively.

Obviously, the length of the nucleation zone has an impact on the product crystals and can be adapted to meet particular requirements. The chosen value is a good compromise between the size of crystals produced, the crystal size distribution and the obtained yield. The overall length of the crystallizer was limited by non-uniform flow patterns potentially caused by exceeding air volumes inside the reactor. The use of bigger air slugs or smaller bubble intervals contributed to this phenomenon, coupled with higher flow rates or smaller production rates.

Figure 5 and 6 show a microscope picture and the number density distribution $q_0(x)$ of the product (image data analysis of 1383 crystals by ImageJ).

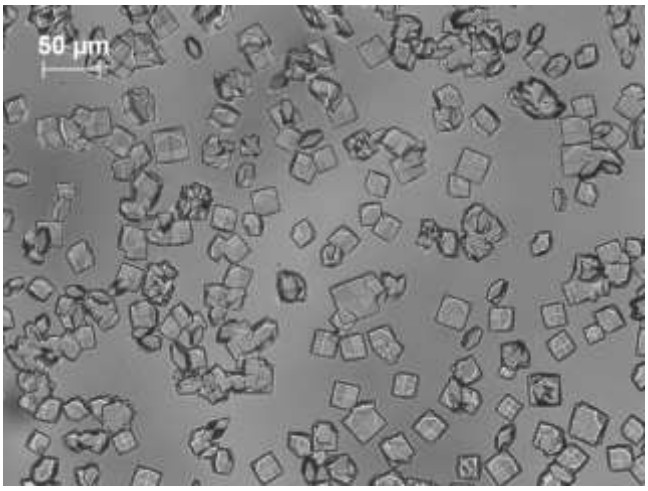

Figure 5: Microscopic picture of crystals produced in the continuous crystallizer.

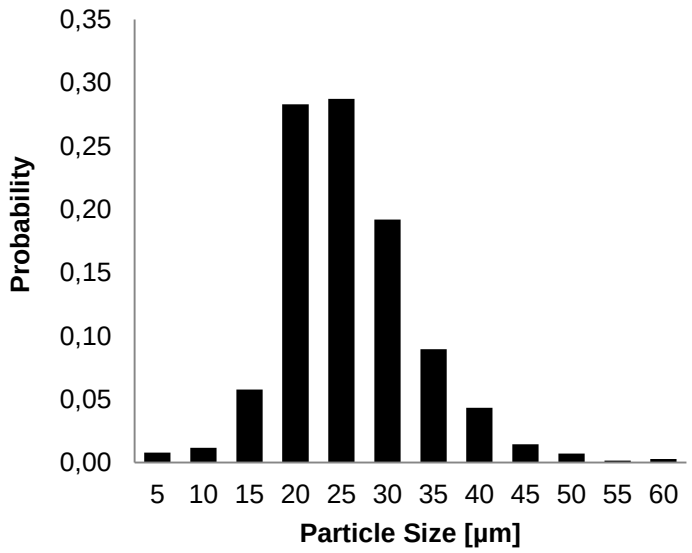

Figure 6: Number density distribution of product crystals.

In contrast to agitated systems (data not shown here) we achieved the formation of well-defined crystals and high yields within short residence times in a tubular crystallizer. Running the crystallizer at a low average velocity of 1.9 mm/s ensured a laminar flow and very low shear forces at the surface of the particles. Mixing induced by the air bubbles proved to be sufficient to overcome sedimentation of crystals inside the reactor. In experiments without introduction of air slugs, crystal transport was ineffective, leading to a high residence time

distribution and possible accumulation of crystals inside the crystallizer. Moreover, product analysis of these experiments showed increased numbers of crystals aggregates.

In our experiments, apparent growth rates of up to 25 µm/h were observed, which agrees well with the data obtained by Forsythe et al.[26,44] who performed growth rate studies at pH4.0, 5% NaCl and 22°C. Face growth rates were about 35 µm/h for very high supersaturation levels of S = 25 and were below 1 µm/h at supersaturation levels <10 in a quiescent fluid (apparatus described by M.L. Pusey[45]). We conclude that nucleation of lysozyme crystals at high supersaturation levels (S=10) was achieved in our continuous crystallizer. Comparing our results to experiments referenced above, where shear forces proved to be detrimental to protein crystal growth, in our reactor the attachment of growth units to form macroscopic crystals was not significantly hindered by shear. Furthermore, formation of amorphous protein precipitate was avoided.

In the experiments crystal aggregation was observed in individual samples of 2 out of 5 experiments. The overall number of crystal aggregates, though, was small and therefore did not impact the number density distribution significantly. Sizes of aggregates were found to range from 50 µm to as large as 250 µm. The effect was increased at reduced flow rates (see Figure 7). Thus, low shear forces inside the reactor support the formation of crystal aggregates as contact times between crystals are considerably increased, facilitating intergrowth. At elevated flow rates (average velocity of 3.8 mm/s), aggregation was inhibited and there was a substantial decrease in average crystal size and yield.

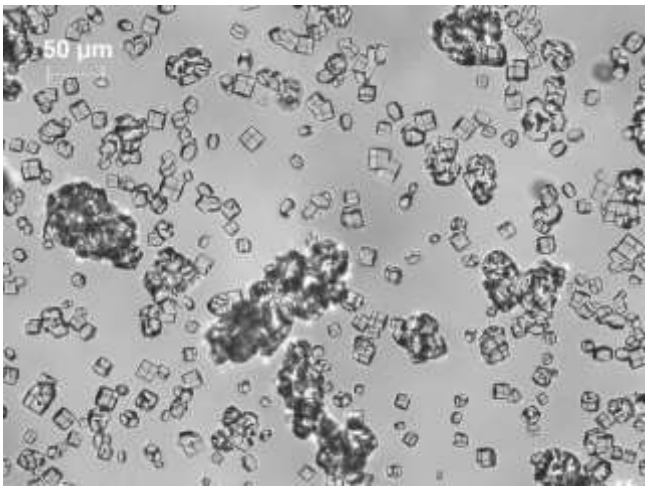

Figure 7: Low flow rates (v less than 1.9 mm/s) regularly led to crystal aggregation.

These findings are in line with preliminary tests using batch reactors (see supporting information) in our study. Without agitation, crystals of over 100 µm in size (most of which were sticking to the wall) were obtained within 24 h in the 10 mL batch experiments. An agitation speed of 180 rpm led to the formation of a crystalline suspension with crystals not exceeding 100 µm within the same time range. Higher power input led to the formation of mostly amorphous protein precipitate. Agitated batch crystallizers of industrial scale impart high shear forces which are detrimental to the fragile 3D structure of proteins and their respective crystals. Moreover, by interaction with surfaces (potentially enhanced by agitation) the formation of amorphous precipitate is likely to be induced.[46] This confirms the need for the development of new high-throughput protein crystallization processes.

Initial concentrations in our experiments allowed crystallization temperatures around room temperature. This is advantageous considering the general sensitivity of proteins to high temperatures (less relevant for the model protein we used) and the potential to increase the yield by cooling the suspension to lower temperatures.

2.4 *Summary and Conclusion*

In our work, we describe a novel tubular crystallizer for protein crystallization, which operates in a continuous way. Its dimensions (inner diameter: 2 mm, overall length: 13 m) and a total linear flow rate of 1.9 mm/s allowed crystal growth at a rate found for quiescent conditions and the production rates of close to a g per hour (0.72 g/h). Lysozyme was chosen as a model protein since it can be crystallized in a straightforward manner. Moreover, its solubility can be controlled over a wide range via changes in the solution temperature. Using a syringe pump, a solution of 100 g/L lysozyme at pH4.6 was mixed with a crystallization-agent solution of NaCl. The resulting concentrations of 4% NaCl, 50 g/L lysozyme and 0.05 M acetate buffer led to a supersaturation of S = 10 to allow nucleation. By using water baths with various temperatures for supersaturation control, the nucleation zone of the crystallizer was separated from the growth zone where supersaturation was kept at S ≈ 8-5.

Specifically, the main results of our work are:

Lysozyme crystals of 15 - 40 µm with intact shapes were produced with a residence time of less than 2 hours in a continuous system.

Production rates of 0.72 g/h were obtained.

Shear forces inside the reactor proofed to be low enough to allow crystal growth at a high rate and crystal breakage was prohibited.
Formation of amorphous precipitate was prevented during the process.

Protein formulations based on crystallized proteins may have better properties than current protein formulations, such as lyophilizates or aqueous solutions. In terms of resuspendability, syringeability and injectability, crystalline material of this size may be well suited for pharmaceutical applications.[47]

3 Crystal Engineering in Continuous Plug-Flow Crystallizers[c]

Abstract. Size, shape, and polymorphic form are the critical attributes of crystalline particles, and represent the major focus of today's crystallization process design. This work demonstrates how crystal properties can be tuned efficiently in solution via a tubular crystallizer that facilitates rapid temperature cycling. Controlled crystal growth, dissolution, and secondary nucleation allow a precise control of the crystal size and shape distribution, as well as polymorphic composition. Tubular crystallizers utilizing segmented flow such as the one presented in our work, can provide plug flow characteristics, fast heating and cooling, allowing for rapid changes of the supersaturation. This makes them superior for crystal engineering over common crystallizers. Characterization of particle transport, however, revealed that careful selection of process parameters, such as tubing diameter, flow rates, solvents, etc., is crucial to achieve the full benefits of such reactors.

3.1 *Introduction*

Crystal engineering involves the ability to specifically tune the physico-chemical properties of crystalline matter. As such, crystal engineering is based on an "understanding of intermolecular interactions in the context of crystal packing and the utilization of such understanding in the design of new solids with desired physical and chemical properties."[1] This involves the arrangement of the atoms or molecules that comprise the crystal, as well as the size and morphology of individual crystals. While the lattice structure and associated defects determine a crystal's thermodynamic properties, the macromolecular properties such as shape determine the kinetic effects.

Pharmaceutical applications typically involve organic crystals of small molecules with a molecular weight < 500 g/mol that can crystallize in several polymorphic forms, i.e., the same molecule(s) arranged in a different crystal lattice. Most new drugs on the market and in the development pipelines fall into class II biopharmaceuticals, and as such, exhibit a high permeability but low solubility. The low solubility poses significant challenges for drug release.[2] While the solubility depends on the crystal structure (with amorphous forms usually

[c] This chapter is based on the journal article by Neugebauer, Besenhard et al. in Crystal Growth and Design 2017.

providing the highest solubility), the dissolution rate is also affected by the total crystal surface area. The surface energy of a crystal is face-specific[48,49]. Therefore, the crystal shape also affects the dissolution kinetics.[50] This highlights the importance of the intra- and macromolecular properties of crystalline matter for a drug's bioavailability. Furthermore, crystal properties play a key role in pharmaceutical process development and production. Crystal size and shape determine the design of downstream operations, such as filtration, drying washing, mixing, tabletting, capsule filling and powder flow properties in general. Different crystal facets expose the molecules at different orientations which can influence a wide range of properties such as catalytic activity, the tendency for electrostatic charging, wettability, hydrophobicity, and chemical stability. [51–54] Therefore, crystal shape engineering can improve the long-term stability and extend the shelf life of crystalline pharmaceuticals. It should be pointed out, that size and shape of crystalline matter are always distributions, which will affect the use of this particulate system dramatically.

Crystallization from solution is the prevailing process for separation and purification in pharmaceutical manufacturing. Tuning the crystals' physio-chemical properties at this stage allows to define the product crystals' attributes at the beginning of the production.

A common approach to crystal engineering in solution involves the use of additives.[55–57] However, an addition of chemicals might require further separation steps and poses additional regulatory and quality control challenges for pharmaceutical production. An alternative approach is supersaturation control, which provides a non-chemical route to change crystal properties during the crystallization process, or directly after, while the crystals are still in solution. Tight supersaturation control is not trivial and traditional batch crystallizers quickly reach their operational limits, if high supersaturation levels and rapid changes of the latter are required.

Tubular crystallizers (typically with an inner diameter of < 10 cm and a length > 1m) are characterized by a high surface-to-volume ratio which facilitates faster heat transfer than in equivalent batch reactors.[35,38,58–60]

As the tube diameter gets smaller, the heat transfer rates increase. Tubular crystallizers are suitable for continuous operations and have successfully been applied to a wide range of applications for crystallization from solution.[36,61–68]

What these crystallizer designs have in common is that supersaturation is controlled via a predefined temperature trajectory along the flow direction. However, processing solid particles in small channels is challenging and becomes impossible as the tube diameter approaches the size of manufactured crystals.[69] Depending on the process conditions, fouling

or localized accumulations can result in clogging the reactor. Better particle dispersion and plug flow characteristics for the solid phase can be achieved via segmented flow, i.e., by feeding a gas or an immiscible liquid phase.[61,70,71]

The latter is less common in crystallization due the limited number of green non-polar solvents of appropriate viscosity and miscibility. In addition, heating rates are reduced due to an additional heat capacity of the second fluid and the (generally) thicker wall film. Moreover, phase separation is required downstream.

In this work we demonstrate that a tubular crystallizer, operated in gas-liquid segmented flow mode, can carry out three important crystal-engineering processes continuously, and within minutes, by rapid changes of the supersaturation. First, particle transport in gas liquid segmented flows is discussed, followed by three sections on (i) the removal of fine crystals, (ii) the tuning of crystal shapes, and (iii) the transition between polymorphic forms. Other particle engineering challenges, including the engineering of the solvates/hydrate form or amorphous-crystalline transformations, can be addressed as well and will be the focus of future work.

3.2 *Particle Transport in Gas-Liquid Segmented Flow*

As the tubing diameter decreases, surface tension forces become more relevant in multi-phase flows, leading to various flow patterns depending on the gas- and liquid-flow rates as shown in Figure 8. At low gas flowrates, relative to the liquid phase, bubbles appear in the reactor, i.e., bubbly flow is observed. An increase in the gas flow rates leads to segmented flow (also referred to as gas–liquid Taylor flow or bubble train), which consists of elongated bubbles that can be many times longer than the channel diameter. At high gas-flow rates, annular flow is observed. If both liquid and gas flow rates are high, highly turbulent churn flow can occur.[72] Besides the relative flow rates, the occurrence of a specific flow pattern depends on the fluid properties (e.g., viscosity μ and surface tension σ) affecting the liquid's behaviour on the tube walls,[73] and on the dimensions of the channel and junction.[74–76]

Since the 1960s, several groups have been able to successfully predict the flow patterns via flow maps using dimensionless parameters.[77–82] However, most flow maps are applicable only close to the conditions for which they were obtained.[83] For stable gas-liquid flow at flow rates >1 mL/min capillaries with an inner diameter of < 1 cm are required. Thus, tubing of d_{in} = 2 mm was chosen for this study to process crystals between 1-500 µm in segmented flow.

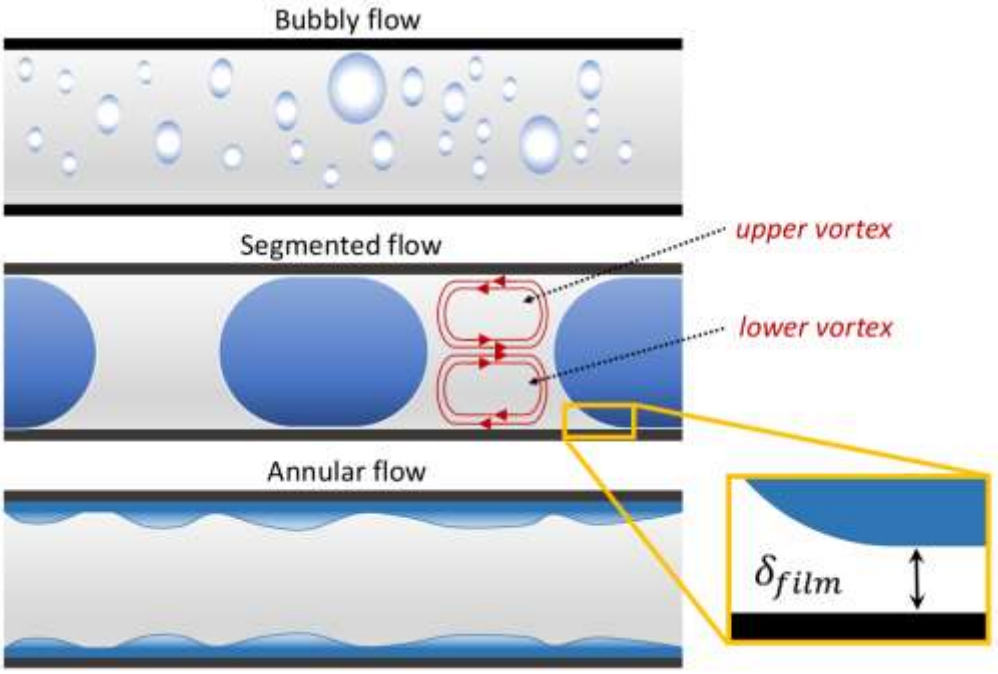

Figure 8: Gas liquid flow pattern in small channels. More details of the hydrodynamics can be found in the literature for slug flow[84,85] and for annular flow[86].

In gas-liquid segmented flows, heat and mass transfer[87,88], as well as particle transport in the slugs, is determined by a wetting film adjacent to the tubing wall (Figure 8, inlet). This phenomenon has been extensively studied, and several expressions correlating film thickness to the channel diameter d and the Capillary number Ca ($= \mu \cdot v/\sigma$) have been proposed.[89–92] The film thickness increases with Ca, i.e., with increasing flow rates/fluid velocities v. The effect of gravity on the film thickness is negligible, especially at small values of $Ca < 10^3$,[93] but cannot be neglected for particle transport. The relative magnitudes of gravity, buoyancy and drag forces determine if particles are suspended homogeneously within a slug or if they accumulate in the rear of the slug.[88]

To demonstrate how particle transport in a gas-liquid segmented flow is determined by the flow and particle properties, a D-mannitol suspension was pumped through a d_{in} = 2 mm tubing and monitored via a high-speed camera.

3.2.1 Materials and Methods: Particle Transport in Small Tubing

Three sieved fractions of D-mannitol (non-commercial sample of high α-form content, spray-dried type, Roquette, France) were suspended in a saturated solution of 60% ethanol (ethanol: 99.8%, denaturized, Carl Roth GmbH, Germany) and 40% water (w/w) or saturated water. The size fractions were: large (150-180 µm), medium (90-150 µm) and small (50-80 µm).

The solid mass fraction was 0.1 g/100 g solution. The suspension was pumped through a tubing of 10 m with a peristaltic pump at various flow rates, $\dot{V}_{Susp}$. We used polysiloxane tubing (Versilic, Saint Gobain, France) with an inner diameter d_{in} of 2.0 mm and an outer diameter (d_{out}) of 4.0 mm. The segmented flow was generated by injecting air via a syringe pump using a T-fitting. The ratio of suspension- to gas-flow rates was fixed to $\dot{V}_{Susp}/\dot{V}_{Air} = 1.6$. After 1 m the tube was passing the field of view of a high-speed camera recording at a frame rate of 500 fps, as described by us recently[36] and as illustrated in Figure 17.

3.2.2 Results and Discussion: Particle Transport in Small Tubing

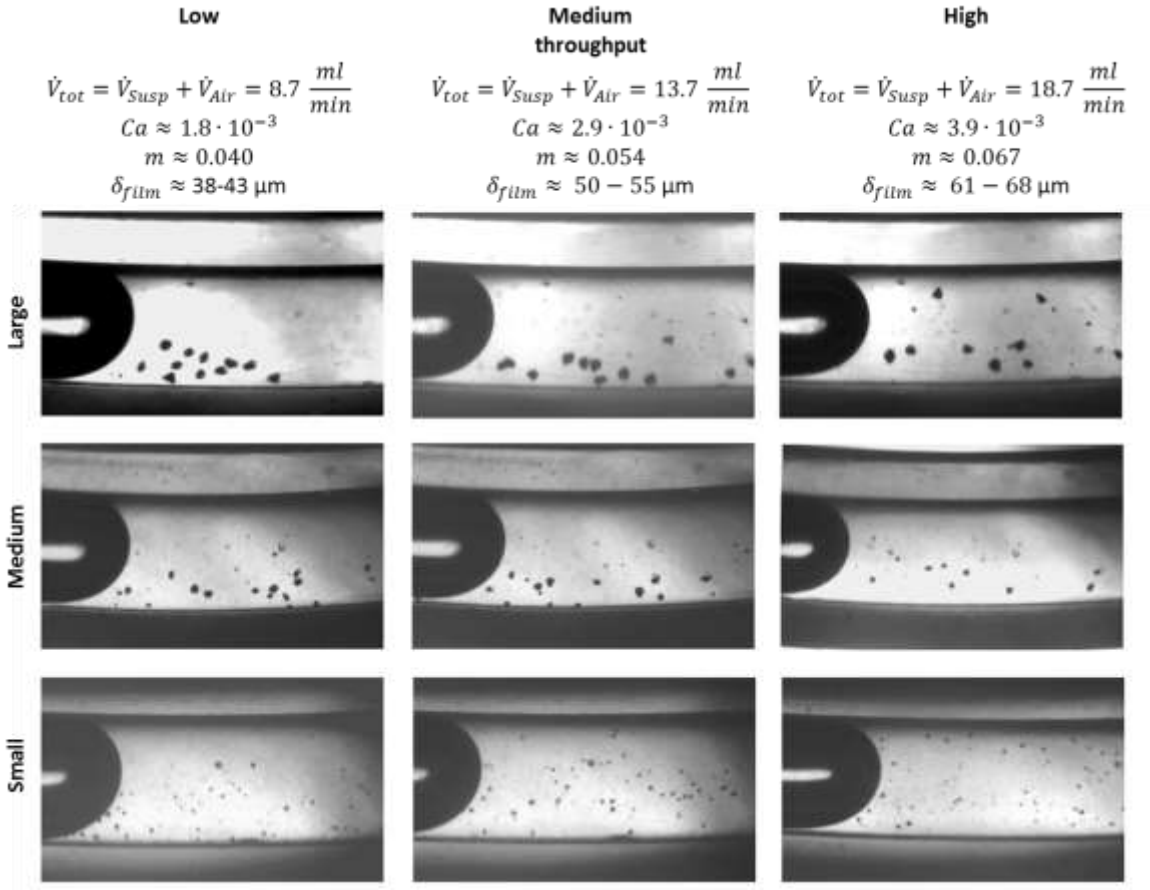

Figure 9: Particle dispersion in a gas (air) liquid (40% water, 60% ethanol) segmented flow. Direction of flow is from left to right. In each sub-image air bubbles can be recognized entering from the left (dark black). For all flow rates (slow, moderate & fast), top row: large particles (150-180 µm), middle row: medium particles (90-150 µm), bottom row: small particles (50-80 µm);

$$\dot{V}_{Susp}/\dot{V}_{Air} = 1.6\ .$$

Images taken from the videos are shown in Figure 9. They highlight the influence of the flow rate and particle size on the dispersion of particles in the segments. Only at the highest flow rate ($\dot{V}_{tot} = 18.7$ ml/min), the large D-mannitol crystals were dispersed throughout the slug, although not homogeneously. Low ($\dot{V}_{tot} = 8.7$ ml/min) and moderate ($\dot{V}_{tot} = 13.7$ ml/min) flow rates caused accumulation of crystals in the lower part of the slug. Moreover, crystals accumulated at the rear end of the slug at the lowest flow rate. Also, medium-sized crystals spread more homogeneously at the highest flowrate, yet they were not perfectly dispersed throughout the segments. For low and intermediate flow rates, the particle concentration was higher in the lower vortex, but no accumulation in the rear end was observed even at the lowest flowrate. The smallest crystals were suspended almost homogenously at the moderate flow rate. However, accumulation at the bottom was still observed at the lowest flow rate. In this context, accumulation should not be confused with sedimentation, i.e., crystals trapped in the wall film at the bottom of the slug that are not recirculated.

Yet, the results indicate that increasing the flow rates is an obvious choice for improving the dispersion of particles in the liquid segments separated by gas.

However, not only the flow rates impact the dispersion of particles, but also the wall film thickness increases with the increase in flow rates, as discussed above. The wall film thickness δ_{film} can be calculated using well-known semi-empirical expressions, summarized in [72]. The range of wall thickness calculated via these expressions is shown for every case in Figure 9. A surface tension of $\sigma_{EtOH\,60\%} = 25.26 \cdot 10^{-3} N/m$ was identified, based on the contact angle measurements. Surface tension data of all liquid phases in this study are presented in Table 3. Crystals can pass from one slug to another via the wall film (see Figure 8) if sedimented crystals are of similar or smaller size compared to the film thickness. As the film thickness increases at higher flow rates, larger crystals might travel between slugs, despite the improved dispersion. The images in Figure 9 (and the related videos) show that medium and especially small D-mannitol crystals can travel between neighbouring slugs if they become trapped in the wall film at the bottom. The consequence is a broader residence time distribution (RSD) of particles. Hence, deviations from an ideal plug flow reactor were strongest for the small D-mannitol crystals, with a considerable number of crystals passing through the wall film. In contrast, the largest D-mannitol crystals remained in the original slug and did not pass through the liquid wall film for all studied flow rates. Thus, a very narrow RSD of the particulate phase in the tube is obtained although the large particles were not dispersed homogeneously within each segment.

In summary, an increase in flow rate can improve particle dispersion within the segments but comes along with an increase in wall film thickness. This might allow larger particles to travel between slugs. In order to achieve ideal plug flow characteristics for the particulate phase, the film thickness should be significantly smaller than the particle diameter. This can be addressed for example by the solvent selection. Using pure water as a solvent significantly improves particle transport (minimizing/avoiding crystals passing through the liquid wall film) compared to ethanolic solutions. Due to its high surface tension $\sigma_{H_2O} \sim 70 \cdot 10^{-3}\ N/m$, the liquid wall film thickness is reduced significantly, e.g., ~50% compared to the 60% ethanolic solution used for this study. As a consequence, sedimentation of small crystals could be avoided using pure water as shown in Figure 18.

Apart from an increase in the total flow rate, particle dispersion can also be improved by reducing the length of the liquid segments, e.g., by decreasing the ratio of $\dot{V}_{Susp}/\dot{V}_{Air}$ as shown in Figure 18. In addition, an increase in the density of the liquid allows for a better dispersion as demonstrated in the electronic SI providing additional videos of glass beads and sand dispersed in various solvents differing in density.

3.3 *Fines Removal*

As reported by several groups,[94–101] temperature cycling via single or multiple cycles is a simple, yet effective procedure for tuning the crystal size distribution (CSD), and eliminating fines. Tubular crystallizers operated in segmented flow mode offer several advantages for temperature-cycling. They allow for sharp residence time distributions of the crystals in each stage of the reactor if operated properly, (section 3.2), and facilitate particle dispersion at minimum agitation. This minimizes crystal collisions and hence, possible aggregation or agglomeration events during the cooling stages, i.e., where the suspension is supersaturated. Agitation is also well known to reduce the induction time for primary[102] and secondary[103] nucleation. Furthermore, there are no moving parts (e.g., stirrers) that could lead to attrition.

The concept of fines removal via subsequent heating and cooling cycles is as follows: a temporary increase in the temperature causes an overall decrease in the crystal size due to dissolution, with the smallest particles disappearing completely. The subsequent cooling stage(s) introduce(s) recrystallization, allowing the remaining crystals to grow back to their initial size and larger (assuming no new nuclei are formed).[94,96] Consequently, the CSD is shifted towards larger crystals. If fines cannot be removed within a single temperature cycle, the maximum temperature can be increased. However, excessive dissolution needs to be

avoided due to the high supersaturation levels during the successive cooling stage and the low surface area of remaining crystals. This makes the process slow and requires the temperature difference to be adjusted each time the size of the initial crystals change. Whether multiple temperature cycles are superior to a single temperature cycle to remove fines is determined by the size dependence of the crystal growth and dissolution rates. If the growth and dissolution rates are independent of the crystal size, the CSD does not change with more than one cycle. This is demonstrated in Figure 10 showing *in-silico* results (of a population balance model) how multiple temperature cycles influence the CSD in case of size-independent and size-dependent growth rate. Details of the population balance model are shown in section 3.7. Such population balance equation models have been used by several groups to understand the effect of cycling on the CSD and the crystal shape.[104–107]

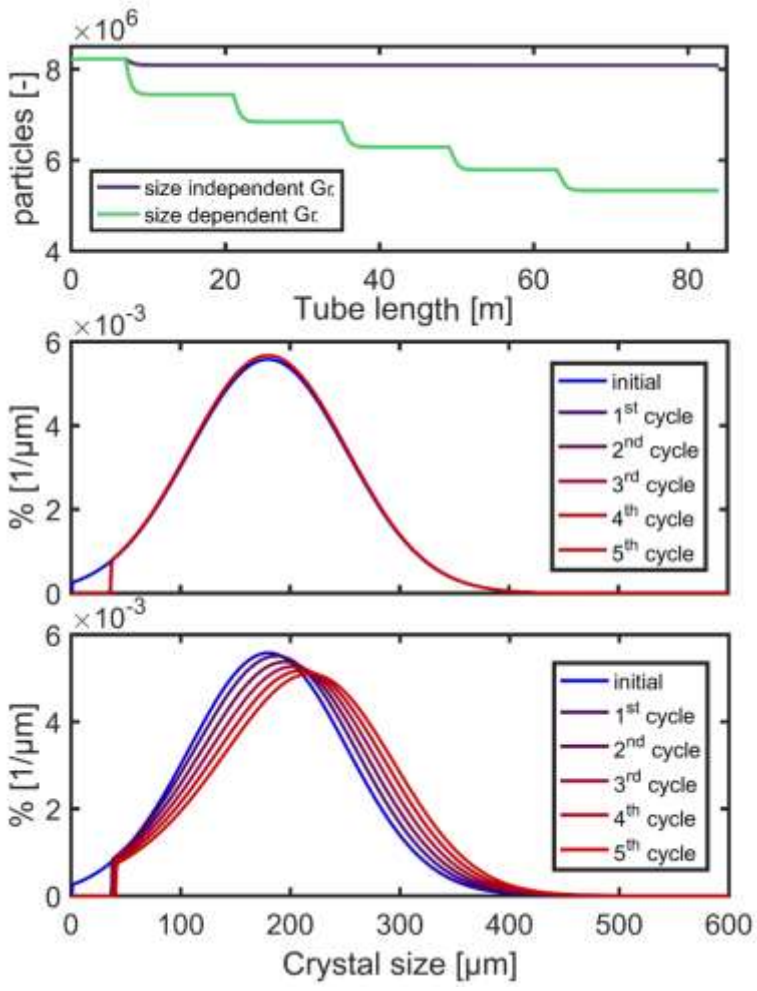

Figure 10: Changes in the number of particles (*top*) and PSD during temperature cycling determined via a Population Balance Model assuming size-independent (*middle*) and size-dependent dissolution rates *(bottom*). The tube length (0.875 m in the heating and cooling bath) did not allow equilibration (S=1) after every heating and cooling step. The related supersaturation profile is shown in bottom of Figure 23.

Many systems show a clear size dependence of growth or dissolution rates, which is why most experimental and computational studies conclude that effective elimination of fines or efficient tuning of CSD cannot be achieved within a single cycle. Reasons for this size dependence are discussed e.g. in [108–111]. Hence, multiple cycles allow for significant changes in the CSD. The same effect, i.e., a continuous change in the CSD with more cycles, is also expected for growth rate dispersion (different crystals of the same size exhibit different growth or dissolution rates) which is sometimes mixed up with size-dependent growth or dissolution kinetics.

Here we demonstrate effective removal of fines from a commercial D-mannitol sample via the tubular crystallizer using multiple temperature cycles. Due to the fast heating and cooling rates high values of supersaturation could be achieved temporarily at a time scale way below the induction times, i.e., in the absence of primary or secondary nucleation events, allowing distinct changes in CSD within minutes.

3.3.1 Materials and Methods: Fines Removal from a Commercial D-Mannitol Sample

The D-mannitol powder used in our study (Pearlitol 160C, Roquette, France, used as received) has a broad CSD. The starting suspension was prepared by dispersing the D-mannitol powder (0.3 g per 100 g) in 500 ml of a saturated ethanolic (50% ethanol 50% water) solution (w/w) in a 1000 mL round bottom flask. Solubility data in the used solvent mixture were determined as described in section 3.7. The flask was briefly immersed in an ultrasonic bath to homogeneously disperse particles and separate aggregates formed during storage. The starting suspension was continuously stirred at 22.0°C with a magnetic stirrer during the process. The stirrer bar and its speed of rotation were carefully selected to avoid the cone effect, i.e., sedimentation of larger particles in the bottom region, resulting in accumulation of larger particles in the flask when withdrawing from the suspension. The test measurements (using the set-up for laser diffraction measurements described below) showed that a uniform dispersion was achieved using a 4 X 0.5 cm stirrer bar at 500 rpm, regardless of the fluid level in the flask. The CSD of the starting suspension changed only marginally, even after two hours of stirring, as shown via FBRM (FBRM field unit, Mettler Toledo, Leicester, UK), see Figure 19.

To study the effect of various temperature profiles on the CSD, the temperature cycling set-up was assembled as explained in Figure 4, path A. The tube was aligned horizontally, with a

maximum curvature of ~0.4 cm^{-1} at the turns and initially filled with a saturated but crystal free solution. Two thermostatic baths at different temperatures generated compartments with temperature differences of 2°C, 4°C or 6°C, depending on the respective experiment. The tubular crystallizer (polysiloxane tubing, d_{in} 2 mm) comprised 15 loops of 186 cm. In each loop, the suspension was heated at first with the tube immersed in a warm bath (47 cm; 24/26/28°C), and subsequently cooled in the cooling water bath (113 cm, 22°C = room temperature). 2 x 13 cm of tubing per loop were used for crossovers from one bath to the other (room temperature = temperature of cooling bath). The unequal partitioning of the tube between the two water baths was used since the dissolution of crystals was expected to be faster than their growth. 1 m of tubing was added before the inlet and after the outlet of the reactor. Thus, the total length of the tubular crystallizer was 30 m.

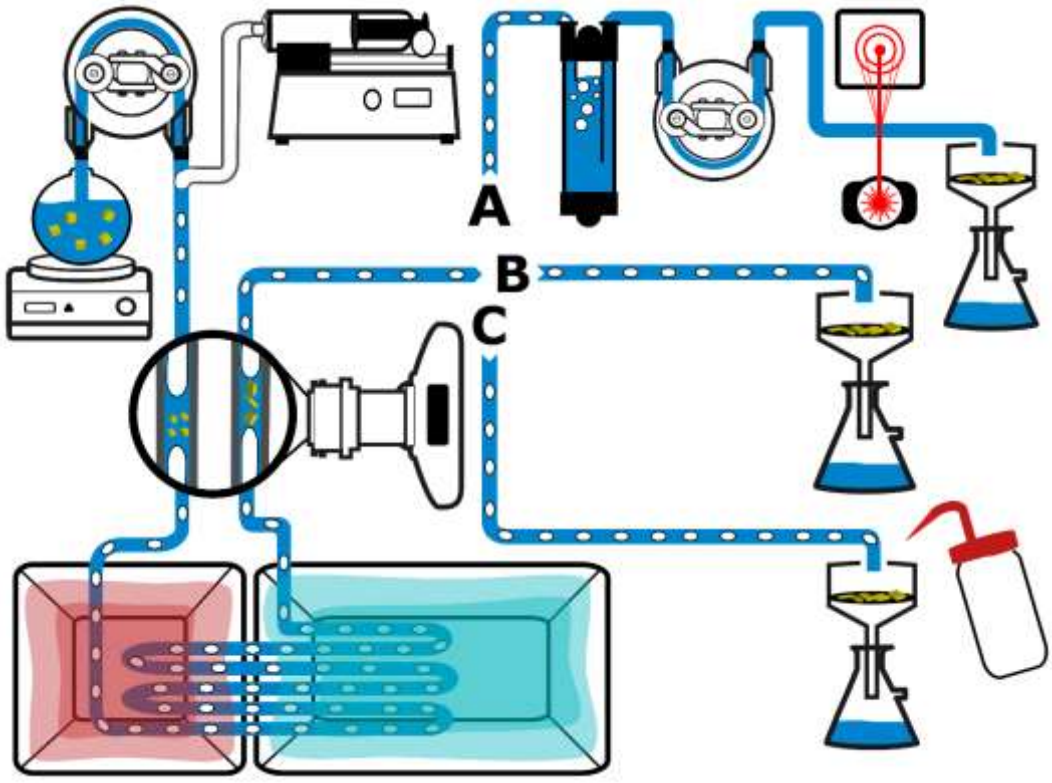

Figure 11: Schematic draft of set-up used for fine removal (A), crystal shape (B), and polymorphism (C) studies. All three process start at the top left of the figure. A crystalline suspension is cycled through water baths via a peristaltic pump alternately passing two temperature- controlled water baths. Compartmentalization is achieved by introducing air bubbles via a syringe pump (2X100ml syringes) keeping the pressure almost constant for >> 30 min. After passing the high-speed camera (monitoring crystals before and after temperature cycling simultaneously), the slurry was A: separated from the gas phase and pumped through the laser diffractometer before filtration; B: filtered; C: filtered while rinsing with Acetone.

Suspension and air flow rates were set to $\dot{V}_{Susp} = 8.5\, ml/min$ and $\dot{V}_{Air} = 5.2\, ml/min$, respectively (i.e., moderate flow rates according to section 3.2). For all settings, initial tests were performed to ensure the absence of primary nucleation by pumping clear saturated solutions through the tubular crystallizer passing the camera.

In order to quantify the changes in the fines content, the CSD was measured immediately. Instead of (error-prone) offline analysis, online laser diffraction was utilized (HELOS, Sympatec GmbH, Germany equipped with a LIXELL flow cell). The product suspension, i.e., the suspension exiting the tubing, was fed into a round 30 mL bottomed flask kept at 22°C via a thermostatic bath to remove the gas phase before passing the suspension through a flow cell (measurement duration: 15 s, measuring range of size: 4.5 – 800 µm), see Figure 11, path A.

To compare the multiple-cycles process to a single-cycle one, additional batch experiments were performed. For the batch experiments, the starting suspension was prepared as described above and heated at 0.1°C/min, i.e., considerably slower than via the tubular crystallizer due to the smaller heat transfer rate in batch, to a temperature of 22.5°C or 23°C at which it was kept for 3 minutes before being cooled to the initial temperature of 22.0°C at 0.1°C/min. Higher temperatures were not possible due to complete dissolution. The suspension was analysed immediately after the cycle via laser diffraction as described above.

3.3.2 Results and Discussion: Fines Removal from a Commercial D-Mannitol Sample

Figure 12**Fehler! Verweisquelle konnte nicht gefunden werden.** (top) shows the CSD of the starting suspension compared to products after temperature cycling in the tubular crystallizer at temperature differences of 2°C, 4°C, and 6°C. Respective microscope pictures of the product crystals can be found in Figure 13. Clearly, with an increasing temperature difference the number of fines decreases. Simultaneously, particles of more than 400 µm appear in the product.

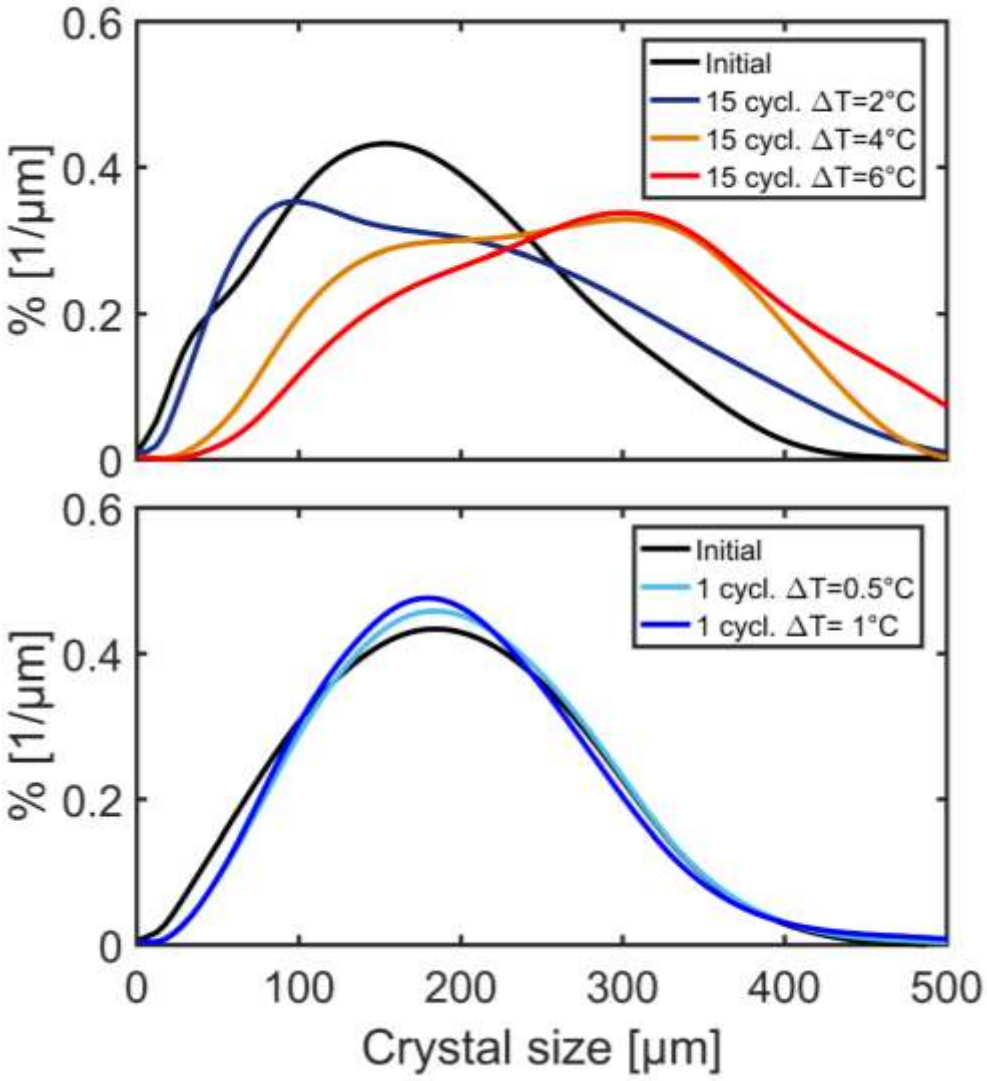

Figure 12: Measured crystal size distributions of the D-mannitol suspension cycled (*top*) multiple times via the tubular crystallizer and (*bottom*) once in batch.

Due to the fast cycling, < 45 s per cycle, the suspension was not in equilibrium at the end of each cycle, i.e., $S \neq 1$ (supersaturation is defined as the ratio of concentration and solubility, $S = c(w/w)/c^*(w/w)$, throughout this work). The temperature profile was calculated using the model described in section 3.7, yielding minimum and maximum temperatures of $T_{min} =$ 22.1 and $T_{max} = 24.9$°C (see Figure 29). This T_{max} corresponds to an under saturation of $S_{min} = 0.87$. Rapid temperature cycling in the tubular reactor allowed for high average super- and undersaturations, $\frac{1}{t_{end}-t_{start}} \int_{t_{start}}^{t_{end}} |S(t) - 1|\, dt \gg 1$, enhancing dissolution and growth.

a) **b)**

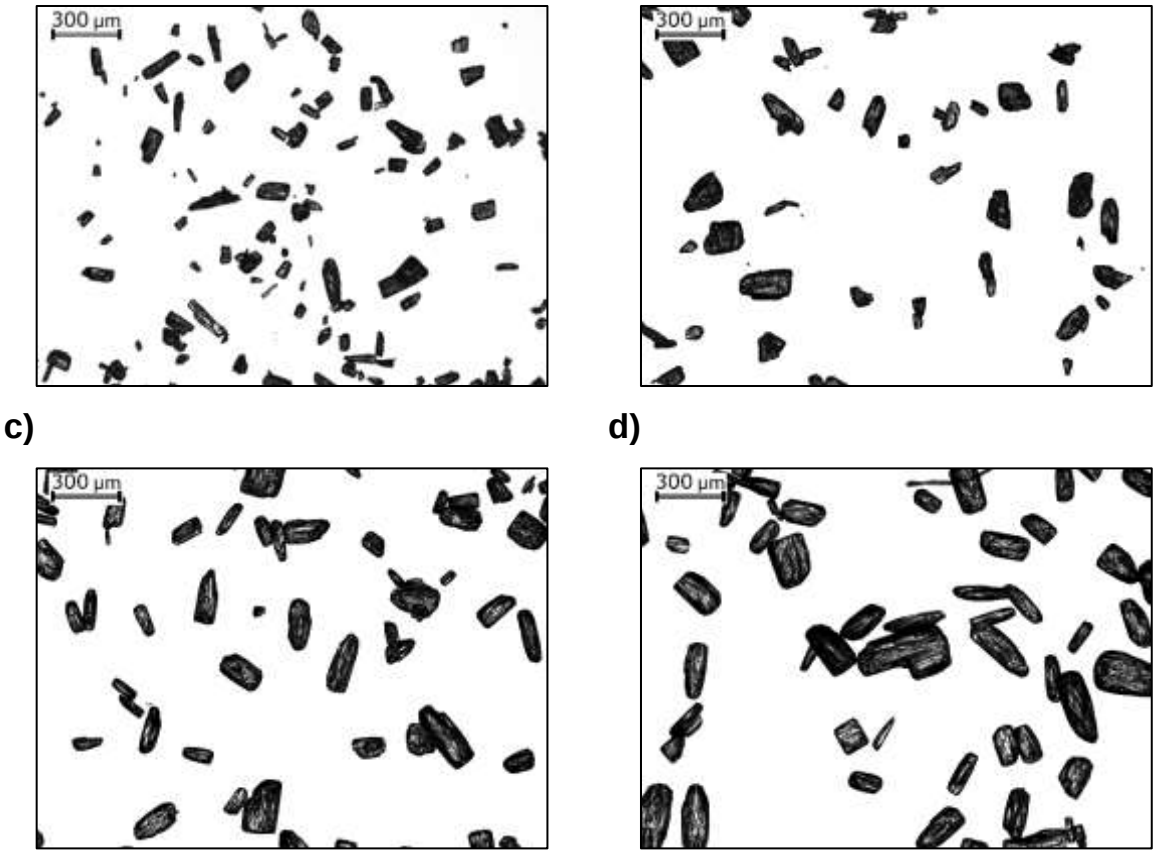

Figure 13: Microscope pictures of product crystals after passing through the tubular crystallizer for different temperature gradients. (a) ΔT=0°C (constant temperature in both baths, i.e., 22 °C). (b) ΔT=2°C. (c) ΔT=4°C. (d) ΔT=6°C

These high average super- and under-saturations facilitated a more significant change in the CSD via rapid temperature cycling in the tubular crystallizer than via a single temperature cycle performed in batch (see Figure 12, bottom) within shorter time. Tubular crystallizer: 15 cycles, 11 min; Batch: 1 cycle, 13 or 23 min). However, fines removal considering the achieved minimal crystal size after cycling, was only superior to batch, if the temperature differences exceeded $\Delta T = 2$°C.

3.4 *Crystal Shape Tuning*

Controlling crystal shape is commonly achieved via the addition of growth inhibitors. The face-selective adsorption of these additives decelerates or even blocks growth of the specific facets to control the crystal shape. However, additives increase costs, and may add to the complexity of the process. Additives are frequently toxic and require further down-stream processes, such as recrystallization and separation.[54] Furthermore, the solvent can influence

the integration of solute molecules into the crystal surface, and hence, the crystal shape. This effect is particularly pronounced if the chemical structure of the solvent and the solute are related. The molecular conformation, solvation and clustering of the solute is also affected by the solvent.[112,113] However, the occurrence and stability of polymorphic forms does strongly depend on the solvent which is one reason for the usually very limited number of suitable solvent candidates.

Yet, one more strategy for engineering the shape involves manipulation of the supersaturation, for example by temperature cycling of the slurry. Employing adequate saturation control in batch processes is known as a simple and highly effective method to control crystal size.[54,114] Only recently, attempts have been made to influence not only the size, but also the shape of crystals via this approach.[53,54,101,115,116] Still, most studies on crystal shape tuning are of theoretical nature. Limitations of analytical tools to quantify the multidimensional shape of microcrystals have been recognized as a major bottleneck in controlling the crystal shape.[115,117] However, recent advances in 2D-image particle analysis allow the study of 3D crystal shapes.[118–121] All these studies demonstrate that the morphology of a growing crystal evolves towards a steady-state. In contrast, dissolving crystals do not evolve towards such a steady-state. Hence, a crystals shape after multiple dissolution and recrystallization cycles is the combination of the stable steady-state growth morphology and the non-steady dynamic dissolution morphology. This explains why a considerable change in crystal shape, i.e., a change in the relative surface area of the crystal facets sufficient to shift the physio-chemical properties, via temperature cycling requires many cycles, each with significant dissolution during the heating stage. As such, crystal shape control via temperature cycling usually requires long process duration, which makes it frequently impractical.[1]

In the current study, we present how the crystal shape of acetylsalicylic acid (a model substance commonly used for shape control studies) can be changed within minutes using a tubular crystallizer. Its ability to go from a dissolution stage at low undersaturation to a growth stage and then reverse this process within seconds allows for significant dissolution in a minimum amount of time without dissolving entire crystals.

3.4.1 Materials and Methods: Shape Tuning of Acetylsalicylic Acid Crystals

The starting material for shape-tuning experiments was obtained from the commercial acetylsalicylic acid (ASA) powder (ASS 3020, G.L. Pharma, Lannach, Austria) by sieving a fraction of 200-250 µm (size refers to mesh size). Crystals of this size were rather uniform in shape, i.e., rods with a maximum length between 500-800 µm (see Figure 14b). In all ASA shape-tuning experiments, a saturated 96% ethanol solution (ethanol: 96%, denaturized, Carl

Roth GmbH, Germany) was used. A solid mass fraction of 0.5 g powder per 100 g solution was chosen, not to have more than five crystals per segment. This was done to prevent accumulation at the rear ends of the segments which is likely to occur at such low flow rates, (see section 3.2: moderate flow rates) and can promote aggregation. Since the crystals sizes were considerably larger than the wall film thickness, ideal plug flow characteristics were achieved for the cycled crystals (see section 3.2).

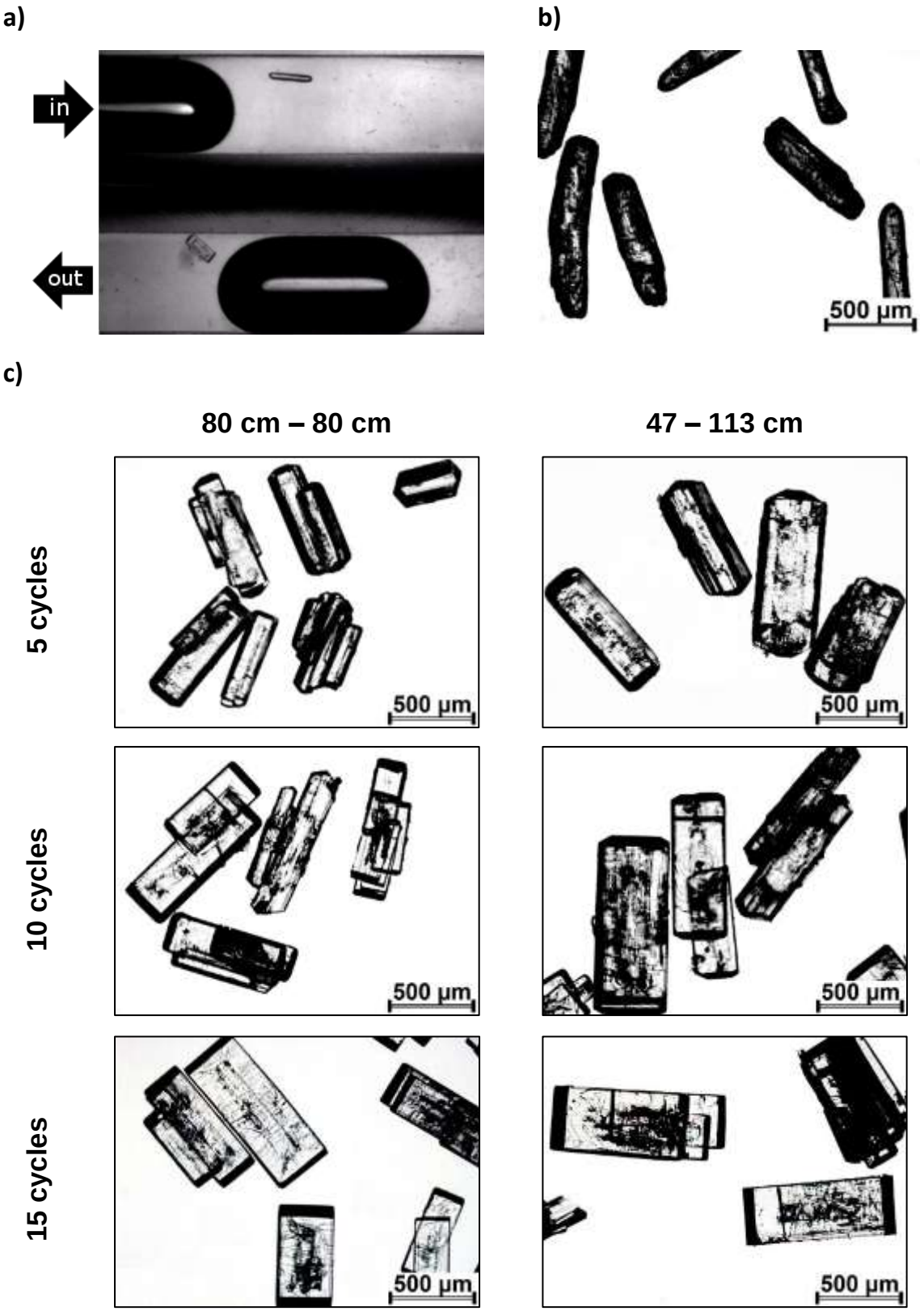

Figure 14: (a) High-speed camera image of a crystal entering the reactor (upper half, movement from left to right) and another crystal after shape tuning (lower half, movement from right to left. Microscope pictures of (b) feed and (c) product crystals after 5, 10 and 15 cycles, compared to a feed sample and a non-cycled sample. Length specifications correspond to the tube length distributions per loop over the two water baths.).

The tubular crystallizer was designed and operated using the flow rates and unequal partitioning of the tube length as described in section 3.3. In addition, experiments were performed with an equal partitioning, i.e., 80 cm of tubing in the warm and cold bath. A process schematic is shown in Figure 11, path B. Experiments were performed using 5, 10 and 15 cycles. The technical limit of the number of cycles or tube length depends on the maximum pressure the pumps can provide and the pressure drop of the used tube. With the described set-up, there were no technical difficulties even when using longer tubing of up to 40 m (data not shown).

The process settings and information about concentration and supersaturation along the temperature cycler are provided in Table 4. The supersaturation values refer to an immediate change in temperature, not considering changes in concentration due to dissolution or growth. The solubility data for ASA were obtained from our previous studies.[36] Temperatures in the water baths were chosen based on high-speed camera videos, monitoring the inlet and outlet, see Figure 14a. The images allowed an initial estimation of successful shape tuning and the absence of nucleation events. The absence of primary nucleation was also tested by cycling a crystal free solution saturated at 22°C. Crystals were filtrated right after the outlet for further analysis.

Table 4: Settings and initial supersaturation levels of shape tuning experiments

	cold water bath (17.0°C)	warm water bath (25.0°C)	starting suspension (22.0°C)
Solubility c* [g/100g solvent][36]	18.4	25.5	22.6
Supersaturation [-]	1.23	0.89	1

3.4.2 Results and Discussion: Shape Tuning of Acetylsalicylic Acid Crystals

Figure 14b and 14c show micrographs comparing the rod-like ASA feed and the product crystals, i.e., those after temperature cycling in ethanol. A change in the shape was apparent already after five cycles (3.5 min residence time). The surface roughness decreased significantly and the crystals lost their round shape and became rectangular and plate-like.

This effect was clearly enhanced after ten cycles and became even more pronounced after 15 cycles showing a significant change in shape. Experiments with the unequal partitioning of the tubing (47 cm cold, 113 cm warm basin) showed a more efficient change of the crystal shape at the same number of temperature cycles.

In a typical batch processes, grinding effects by the stirrer can lead to a decrease in aspect ratio due to smoothening of elongated particles.[122] In our experiments, product crystal shape

was not affected by any moving parts. Plate-like crystals were obtained and no abrasion was observed, resulting in a narrow CSD and well-defined crystals. The described tubular crystallizer design, with each temperature cycle lasting < 1 min, allows facile control of the crystal shape by increasing or reducing the number of cycles.

3.5 *Polymorphism Control*

Following Ostwald's rule of stages, the rate of nucleation of a metastable form is higher than that of the stable form. However, the polymorphic form with the fastest growth rate (which depends on the material, but is frequently the most stable polymorph) will eventually prevail regardless of the rate of primary or secondary nucleation. In addition, kinetic nucleation theory indicates that the primary nucleation rate of a metastable form is never the highest over the entire supersaturation range.[123,124] Thus, the occurrence of a specific polymorph after crystallization is largely determined by its nucleation and growth kinetics in competition with other polymorphic forms. Conversion between polymorphs can occur during various processes and even during handling of the dry powder (e.g., milling). Polymorphic conversion may take anywhere between seconds and decades, making the control of the specific polymorph an important quality parameter of manufacturing.

The conversion of a metastable into the most stable form in solution is likely to follow via a solvent-mediated (polymorphic) transformation (SMT).[125,126] This is a reliable route for obtaining the most stable polymorph in the solvent used. Due to the difference in free energy, the solubility of polymorphic forms differs from each other. SMT starts with dissolution of the metastable form followed by nucleation or growth of the more stable form. Most studies on SMT of small-molecule crystals report nucleation of the more stable form to be the rate-limiting step.[127–129] Since secondary nucleation is frequently reported to dominate SMT, i.e., nucleation of a more stable polymorph on a less stable polymorph (often referred to as cross nucleation), the transition kinetics depend not only on the temperature and supersaturation but also on the number and CSD (i.e., the total crystal surface) of both phases.

Due to the supersaturation-dependence of the dissolution rates, growth rates, and nucleation rates (including secondary nucleation), temperature cycling can be utilized to control SMT.[130–132] As such, the tubular crystallizer described in this work provides a powerful tool for speeding up a polymorphic transition under highly controlled process conditions. The continuous process benefits from a number of advantages discussed above.

In this study, we use the described tubular crystallizer to study SMT. D-Mannitol was chosen as model substance since the crystal structures of the polymorphs are known[133] and their difference in free energy and solubility have extensively been reported.[134,135] Because SMT proceeds via nucleation rather large temperature differences were chosen to promote nucleation events which was avoided for the fine removal and shape tuning studies.

3.5.1 Set-Up: Polymorphism Control of D-Mannitol

Among the three polymorphs of D-mannitol, the most stable under environmental conditions and water is the β form, followed by the α-form. The least stable is the δ-form. The α-form has little energetic difference from the β-form and similar physio-chemical properties.[136,137] The δ-form was shown to be kinetically stable during milling and after 5 years of storage at 25°C and dry conditions. In pharmaceutical products, the β-form prevails since it is thermodynamically stable at RT, although the δ-form is increasingly used due to its superior compaction properties, e.g., for tableting[138] and roller compaction[139].

The (absolute) difference in free energy between these three polymorphs diminishes at lower temperatures and in ethanol-water mixtures, i.e. difference in solubility decreases with higher ethanol fractions. Therefore, a 60% ethanol and 40% water solution (w/w) solution was used for all polymorphism control experiments, preserving the stability of the α-polymorph (solid mass fractions, as described below) in the initial suspension for several hours, as shown in Figure 19. Solubility data for β-form in the used solvent mixture were determined as described in section 3.7.

The experimental procedure for the polymorphism studies of D-mannitol using a tubular crystallizer is shown in Figure 11, path C. Similar to the experiments shown in section 3.3 the solvent was saturated with D-mannitol (β-form) at 22°C. Defined powder mixtures of two polymorphs (α-form: non-commercial, spray-dried type; β-form: Pearlitol 160C, both from Roquette, France) were added to the saturated solution (saturated with β-form of D-mannitol at 22°C) to a solid mass fraction of 0.8% (w/w). Hence, the total amount of processed crystalline material was > 5 g/h which is enough for microscopic studies. However, industrial applications would require higher solid mass production rates. In order to minimize any size effects, sieved fractions of D-mannitol (80 – 120 µm) were used in all polymorphism-control experiments. Rapid temperature cycling was performed by pumping the suspension through the tubing (same flow rates and length as used in the previous studies) immersed in water baths, cooled up to 10°C and heated up to 40°C. Due to the flow rates and the tube lengths the temperature in the suspension did not reach the respective temperature of the water baths.

Using the model described in the section 3.7, the minimum and maximum temperatures were estimated as T_{min} =11.6°C and T_{max} =30.9°C at the biggest temperature difference (see Figure 30), corresponding to super- and under saturations of $S_{max} = 1.90$ and $S_{min} = 0.71$.
Products samples were obtained by immediately filtering the product suspension while rinsing it with acetone in order to avoid that residual water induces additional polymorphic transitions after the filtration. The polymorphic composition of the samples was determined via Raman spectroscopy (Perkin-Elmer Raman Station 400, Waltham, USA) and multivariate data analysis, i.e., by applying a PLS model. Details of the procedure, including processing of spectral data, generation and analysis of calibration sample, as well as a thorough description of the PLS model and its evaluation, are presented in section 3.7.

3.5.2 Results and Discussion: Polymorphism Control of D-mannitol

The mixtures of the α- and β-forms in the starting suspension and the composition of the product suspension after temperature cycling are listed in Table 5. For both powder mixtures, the fraction of the β-form in the product suspension increased and the α-form decreased. The higher the temperature difference of the water bath was, the more pronounced was this effect. The formation of the δ-form was never observed. Higher supersaturation is associated with higher nucleation rates, which agrees with an increase in the fraction of the β-form, associated with an increase in the temperature difference.
Primary nucleation was marginal as evident from preliminary studies cycling crystal free solutions while monitoring the outlet with the high-speed camera and the micrographs of collected samples. As can be seen in Figure 15c and 15d and from quantification, the product crystals clearly show secondary nucleation of the β-form on the surface of the α-form crystals, indicating cross-nucleation. A comparison of micrographs shows a subsequent growth resulting in sea-urchin-like particles for all initial compositions and all temperature differences, but no significant number of fines. Although, the quantity of the β-form in the second starting suspension (50% w/w) was higher than in the first one (20% w/w), a similar or even higher amount of the β-form was generated during cycling, especially for the highest temperature difference. This indicates that SMT is governed by cross nucleation rather than by the growth of the seeded β-form crystals. For D-mannitol, it has been reported that an α form seed crystal always induces the crystallization of the α-form and the β-polymorph seed yields the β- or α-form, whereas the δ-form seed yields the α-form.[140] However, the β-form can nucleate on the α-form at high supersaturations, e.g., during quench-cooling.[123] This

agrees with our results showing cross nucleation of the β-form as was confirmed via Raman microscope studies on single particles as shown in Figure 16.

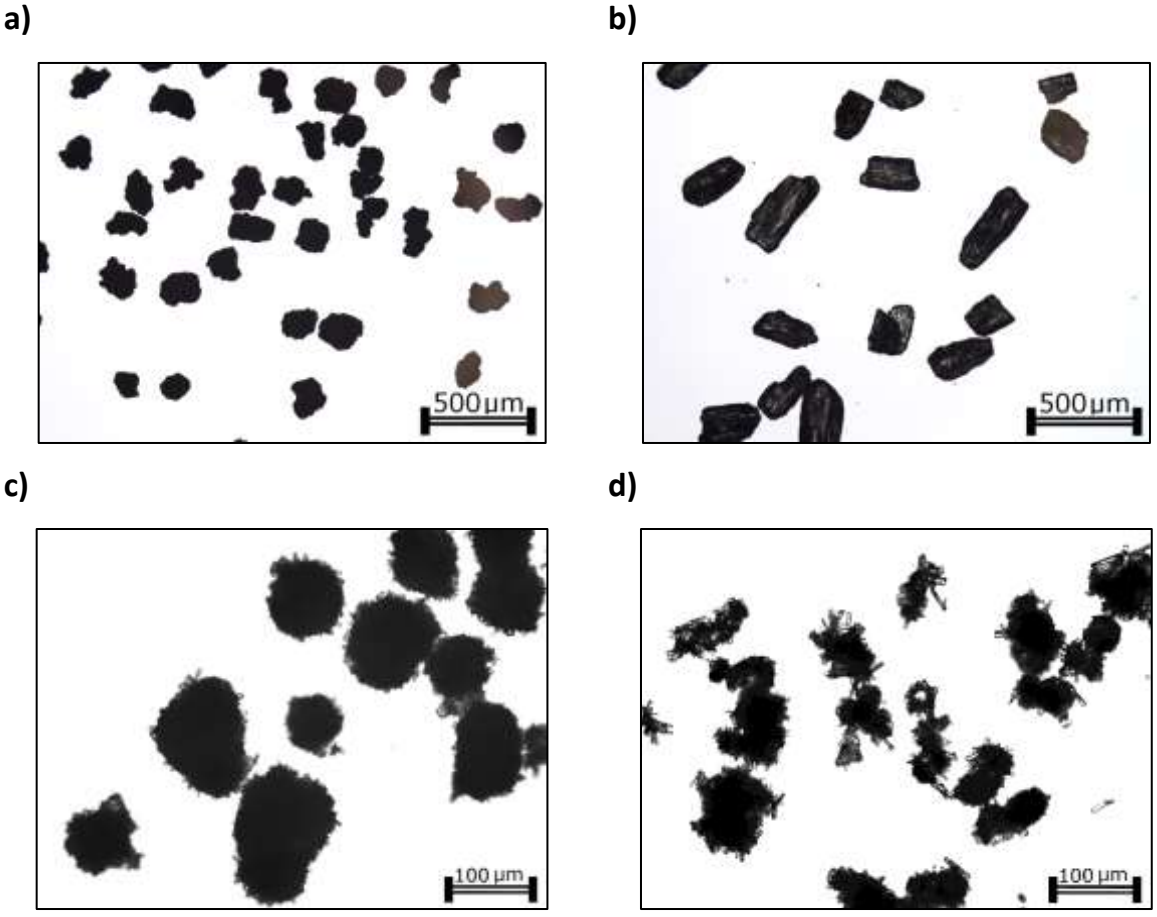

Figure 15: *(a)* Microscope picture of spray-dried α-mannitol as received. (b) β-D-mannitol (Pearlitol 160C, Roquette, as received. Product crystals after temperature cycling (starting suspension: 80% α-form, 20% β-form) (c) ΔT = 20°C, (d) ΔT = 30°C

Table 5: Experimental data polymorphism control.

	mass fractions in the starting suspension (as prepared)		Temperature water bath 1	Temperature water bath 2	mass fraction in the product suspension obtained from Raman spectra and PLS model	
	α-form	β-form			α-form	β-form
starting susp. t=0min	80%	20%	-	-	82±4%	18±4%
starting susp. t=60min	-	-	-	-	77±4%	23±4%
ΔT=30°C	80%	20%	10°C	40°C	59±4%	41±4%
ΔT=20°C	80%	20%	15°C	35°C	66±4%	34±4%
ΔT=10°C	80%	20%	20°C	30°C	68±4%	32±4%
starting susp. t=0min	50%	50%	-	-	53±4%	47±4%
starting susp. t=60min	-	-	-	-	56±4%	44±4%
ΔT=30°C	50%	50%	10°C	40°C	34±4%	66±4%
ΔT=20°C	50%	50%	15°C	35°C	39±4%	61±4%
ΔT=10°C	50%	50%	20°C	30°C	49±4%	51±4%

The tubular crystallizer can significantly accelerate SMT via temperature cycling as the difference in temperature increases, which is assigned to excessive secondary nucleation. Primary nucleation was prevented by keeping the time at supersaturation below the induction time. More cycles at high (or even higher) temperature differences seem to be the most convenient way to achieve a complete conversion to the β-form. This and the absence of moving parts with associated attrition facilitated the acceleration of SMT yielding big particles that can be filtered easily.

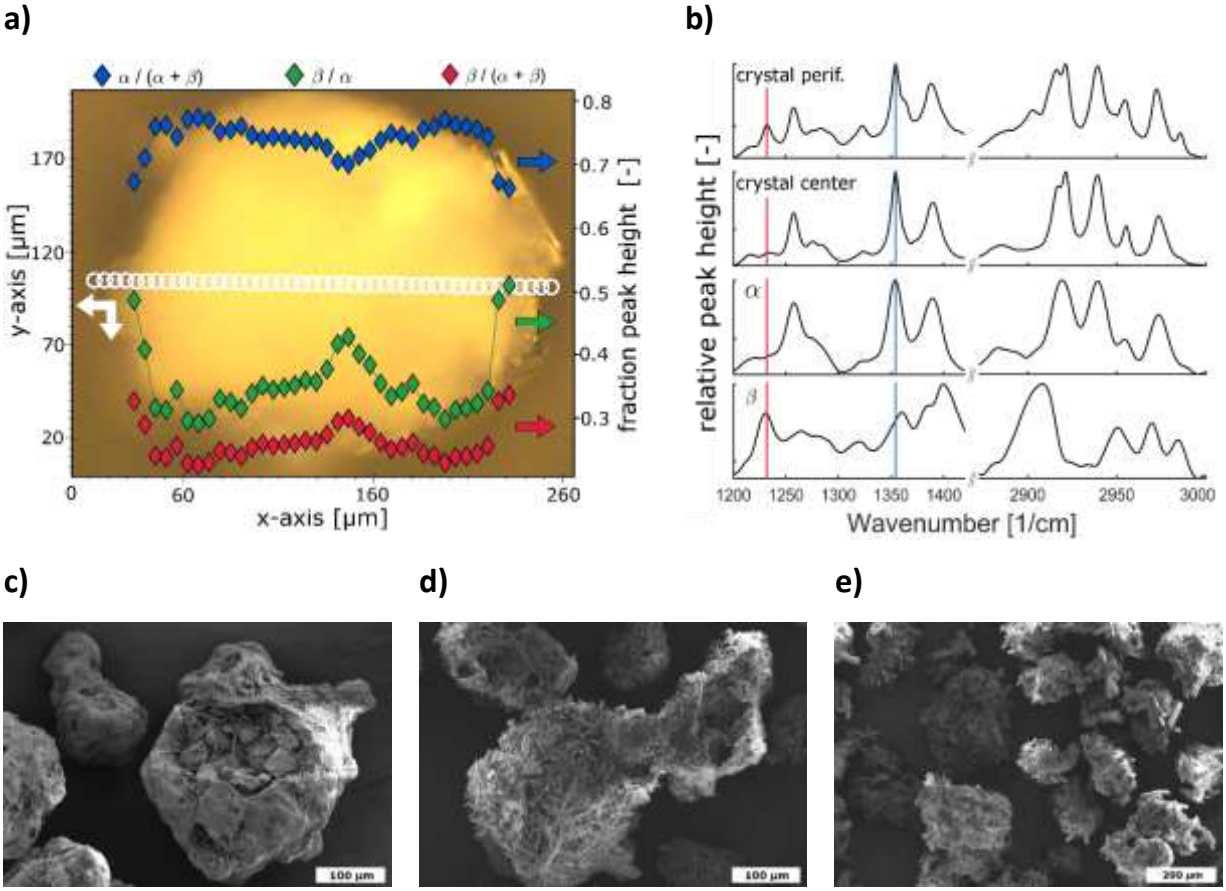

Figure 16: (a) Raman microscope studies on a single particle (initially mostly α form) after temperature cycling at $\Delta T = 30°C$. The white circles on the microscope image show where Raman spectra were recorded. The relative heights of the peaks assigned to the α (1355 cm^{-1}) and β (1233 cm^{-1}) form[134] are superimposed. (b) Raman spectra recorded at the periphery and at the center of the product particle compared to spectra of the seeded α and β form. (c-e) SEM images of (c) seeded particles, (d) cycled at $\Delta T = 20°C$, and (e) $\Delta T = 30°C$. Details on the experimental procedure are provided in section 3.7.

3.6 *Summary and Conclusion*

In this work a flexible tubular crystallizer operated in (gas-liquid) segmented-flow mode was developed. Four different objectives of advanced particle-engineering were successfully demonstrated, i.e., dispersed particle transport, fines removal, shape tuning and polymorphic composition. Despite the simple set-up, crystal engineering could be performed via a continuous process with a considerable volume (~litres per hour) and residence times in the order of several minutes.

Precise control of the supersaturation is key for rational crystallization. By utilizing the heat transfer rates achievable in tubular crystallizer's precise supersaturation levels could be obtained. Moreover, high levels of super- and undersaturation, and the ability to switch between them within seconds allows for rapid dissolution and growth, while preventing primary nucleation, as well as secondary nucleation if needed. This occurs in the absence of any moving parts and at minimum agitation, while segmented flow allows for narrow residence time distributions.

However, achieving ideal plug flow characteristics for the particulate phase is not trivial as described above. Crystals can travel between slugs, if they become trapped in the wall film. Therefore, the wall film thickness should be smaller than the diameters of processed particulate matter. As shown in this chapter, the film thickness can be efficiently minimized by reducing the flow rates (which impairs particle dispersion in the segments), or using solvents with a higher surface tension (which is not always possible). Hence, the desired plug flow characteristics for liquid and solid phases in tubular reactors operated in segmented-flow mode can only be achieved at the right process settings in consideration of throughput and particle dispersion.

Fines removal via tubular crystallizers using segmented flow was studied via online laser diffraction, showing the potential of fast temperature cycling to shift the crystal size distribution significantly towards larger crystals within minutes. For the studied model system (D-Mannitol, β form) fines could be removed efficiently by increasing the temperature differences for cycling experiments. Other control options would be the number of cycles or the quantity of fed particles.

With respect to crystal shape tuning we showed how fast temperature cycling (at temperature/supersaturation differences way smaller than used for fines removal) can be used to tune the shape of crystals. The studies using acetylsalicylic acid proved that facile control of the crystal shape is possible by manipulation of the number of cycles or the partitioning of heating and cooling segments. Other promising control options to tune crystal shapes in

solution would be the temperature difference during cycling and changes in the solvent composition (not shown here).

The final chapter on describes how fast changes in temperature, and hence switches between super- and under-saturation, affect solvent mediated phase transitions. For the tested transition, i.e., the transition from D-Mannitol's α-form to its β-form, cross nucleation of the β-form on the initially seeded α–form showed to be the rate-limiting step. Transitions became more efficient with increasing differences in temperature during cycling. Hence, the temperature difference during cycling can be used to control the transition kinetics. Since primary nucleation should be avoided (depending on the desired product crystal size distribution) this difference in temperature cannot be increased arbitrarily. Nevertheless, the number of cycles used provide a convenient design tool to further control the final polymorphic composition.

In summary, tubular crystallizers can be used to tune the physio-chemical properties of crystalline matter in a short amount of time without using any additives.

3.7 *Supplementary Information*

3.7.1 Materials (additional information)

For assembly of the tubular crystallizer, straight and T-fittings consisting of PTFE with an inner diameter of 2.0 mm were used. Folded filters and round filters (Type MN 615, Macherey-Nagel, Germany) were used to separate the liquid from the crystalline phase. A sieving tower (AS200, Retsch, Germany) was used for isolating seed crystals (mesh sizes: 200 and 250 µm) from the commercial product.

The high-speed camera was an IDT NX-7-S2 (Imaging Solution GmbH, Germany) equipped with a 12X zoom lens system (Navitar, USA).

Microscope analysis was performed using a Leica DM 4000 microscope together with a Leica DFC 290 camera.

Raman spectroscopy was performed with a Perkin-Elmer Raman Station 400, Waltham, USA) and a Bruker Senterra Raman Microscope (Senterra II, Bruker, Karlsruhe, Germany).

FBRM measurements were performed using a FBRM field unit (Mettler Toledo, Leicester, UK).

3.7.2 Additional information about Experiments and Results

This section presents further details on the experimental set-ups, the data evaluation and material characterization, which are not provided in the main article.

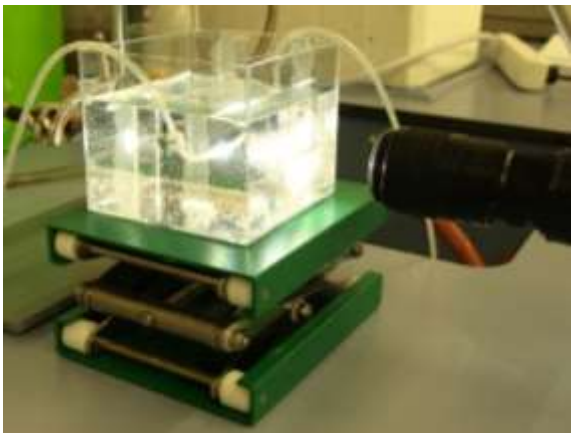

Figure 17: Positioning of high speed camera to record crystals in the tubing. The tubing was immersed in a liquid (water ethanol mixture) of which the refractive index was adjusted to match the refractive index of the solution in the tubing. The light source was placed opposite and in line with the objective.

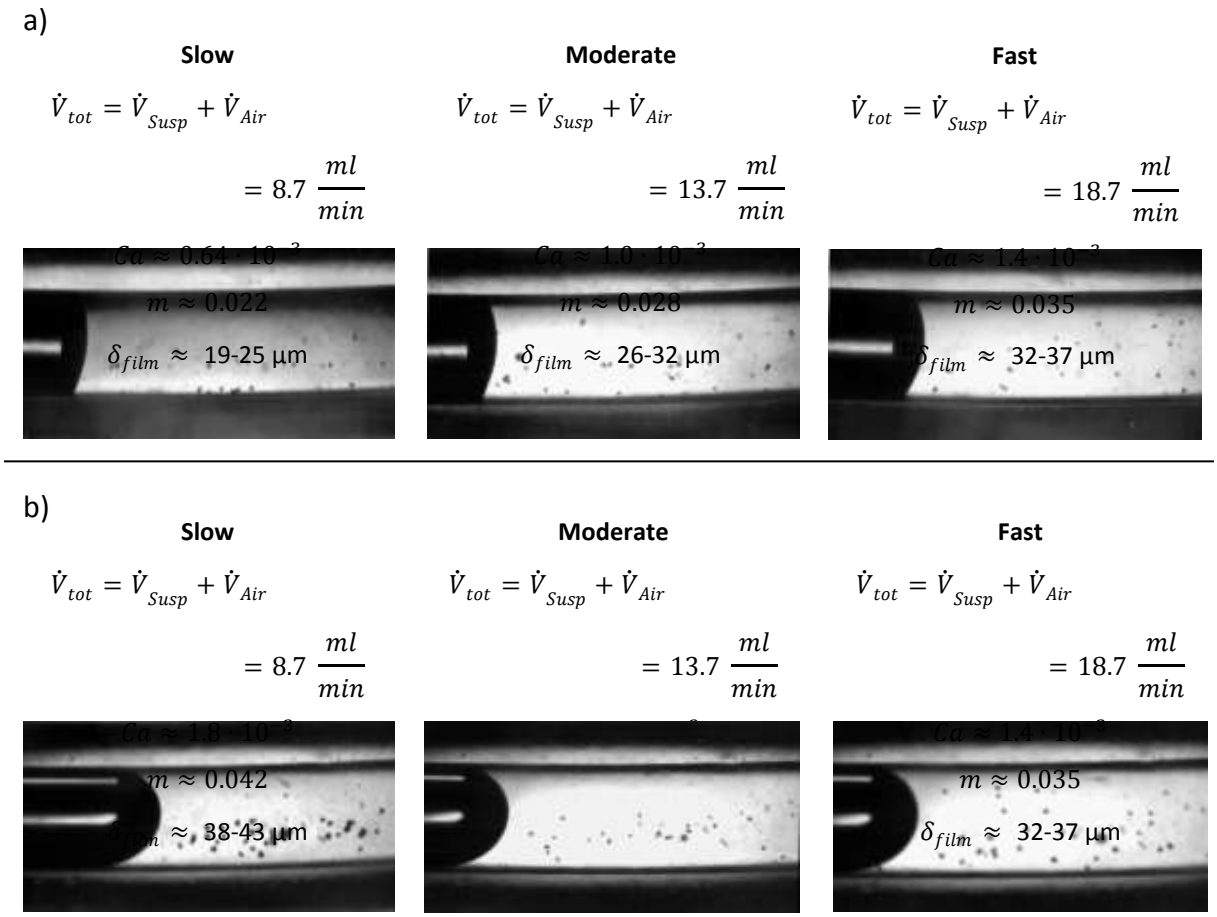

Figure 18: (a) Dispersion of small D-Mannitol particles (50-80 µm) in an air-liquid (saturated solution of mannitol in water) segmented flow. For all flow rates (slow, moderate & fast) $\boldsymbol{\dot{V}_{Susp}/\dot{V}_{Air} = 1.6}$ no sedimentation, and hence transport of crystals to subsequent segments was observed. (b) Dispersion of small D-Mannitol particles (50-80 µm) in a gas (air) liquid (saturated solution of mannitol in 40% water, 60% ethanol) segmented flow. For all flow rates (slow, moderate & fast) $\boldsymbol{\dot{V}_{Air}/\dot{V}_{Susp} = 1.6}$.

The surface tension was determined from contact angle measurement using the Easydrop (Krüss, Germany). All measurements were performed at room temperature (= 22°C).

Table 6: Surface tensions of pure and saturated ethanol-water solutions

Solution	Measurement 1 $[10^{-3} \cdot N/m]$	Measurement 2 $[10^{-3} \cdot N/m]$	Measurement 3 $[10^{-3} \cdot N/m]$	Measurement 4 $[10^{-3} \cdot N/m]$	Measurement 5 $[10^{-3} \cdot N/m]$	Average $[10^{-3} \cdot N/m]$
Water (deionized)[141]						~72
Ethanol 11%, water 89% (w/w)[141]						~46
Ethanol 50%, water 50% (w/w)	27.48	27.57	27.39	27.54	-	27.50 ± 0.08
Ethanol 50%, water 50% (w/w) saturated with (β) D-Mannitol	27.27	27.84	27.90	28.12	27.84	27.79 ± 0.32
Ethanol 60%, water 40% (w/w)	26.14	26.27	26.30	26.22	26.39	26.26 ± 0.09
Ethanol 60%, water 40% (w/w) saturated with (β) D-Mannitol	25.13	25.38	25.36	25.17	-	25.26 ± 0.13
Ethanol saturated with ASA	22.67	22.70	22.68	22.51	22.34	22.53 ± 0.18
Ethanol (99.8%)	21.73	21.83	21.74	21.69	21.81	21.76 ± 0.06

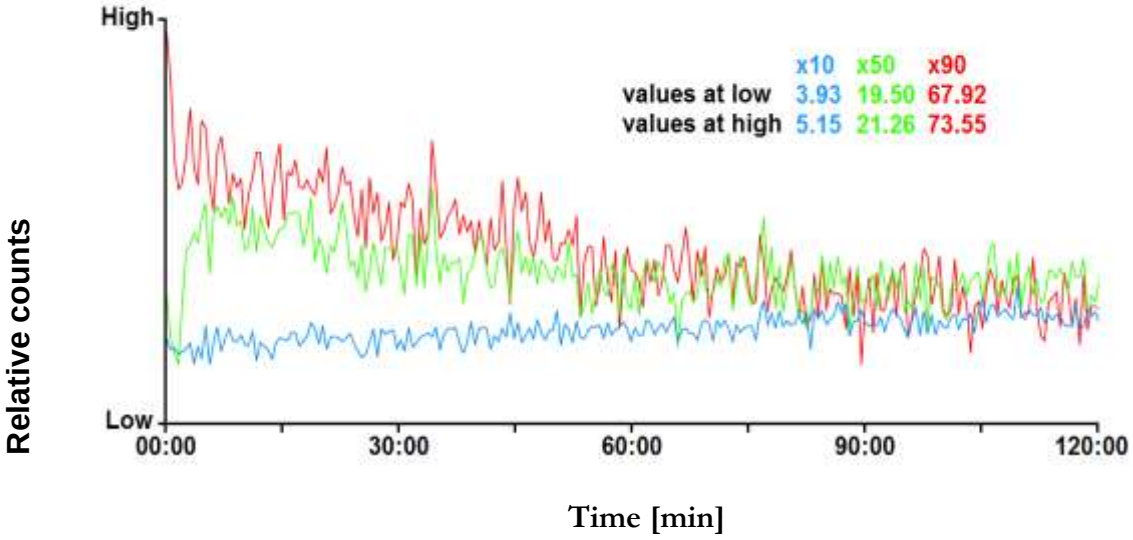

Figure 19: Results from the FBRM measurements, while stirring a D-mannitol suspension over 2h (mass fraction of solid D-mannitol in a saturated solution = 0.3 g/100g).

The stability of α-mannitol (non-commercial spray dried D-mannitol of high α-form content, Roquette, France) in a saturated solution of 60% ethanol and 40% water was investigated over a period of 60 minutes. A sieved fraction of α-mannitol (80 – 120 µm, mass fraction: 0.8 g/100 g solution) was suspended in 300 mL of the respective solution. The suspension was continuously stirred at 22°C using a magnetic stirrer. Samples of 20 ml were taken every 10 minutes, and filtrated while rinsing with acetone to eliminate water residuals. The Raman spectra of collected samples show no significant transition to the β-form, see Figure 20.

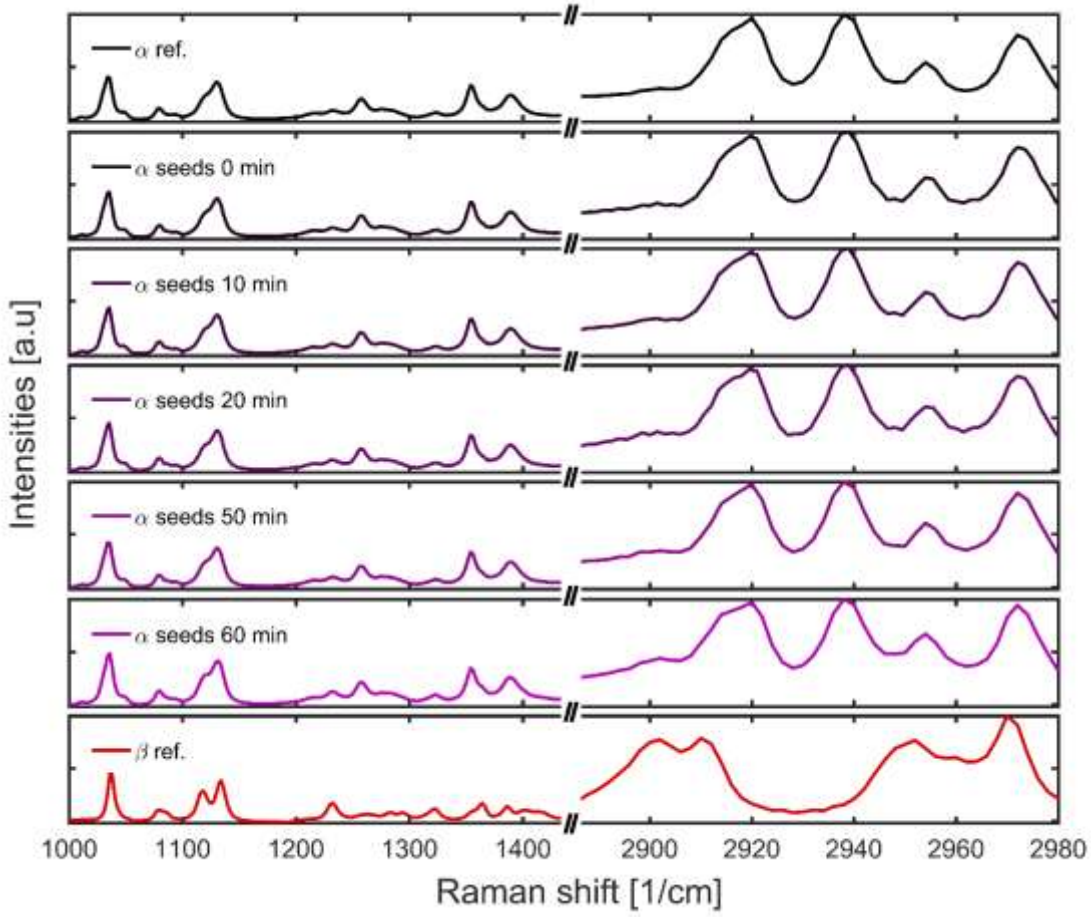

Figure 20: Raman spectra of the samples taken after 0, 10, 20, 50 & 60 min together with reference spectra of the α (non-commercial spray dried D-mannitol obtained from Roquette, France) and β (Pearlitol 160C, both from Roquette, France) form.

Seed particles and products crystals from experiments employing temperature cycling at ΔT = 20°C and ΔT = 30°C were examined using a scanning electron microscope (SEM) (Zeiss Ultra 55, Zeiss, Oberkochen, Germany) operated at 5 kV. The particles had been sputtered with gold-palladium prior to analysis. Results are shown in Figure 16 c-e.

Population balance equation model to model crystal size distribution during temperature cycling

This section presents the mathematical framework of the population balance model used to model the behavior of the crystal size distribution during temperature cycling. The results of this model are discussed in the article.

Table 7: Parameters used to calculate the Temperature profile.

Parameter	Value	Definition
d_{out}	0.004 [m]	outer diameter of the tubing
d_{in}	0.002 [m]	inner diameter of the tubing
α_{outer}	1000 $[\frac{W}{m^2 \cdot K}]$	outer heat transfer coefficient of the tubing
λ_{tubing}	0.3 $[\frac{W}{m \cdot K}]$	heat conductivity of the (silicone) tubing
$c_{p,slurry}$	2482 $[\frac{J}{kg \cdot K}]$	heat capacity of the slurry (~heat capacity of EtOH at 30°C)

The used population balance model assumes cubic crystals. Hence, the volume of a crystal is defined by

$$V_{cryst}(L) = k_v \cdot L^3 \quad (1)$$

with a volume shape factor of $k_v = 1$.

The initial crystal size distributions (= normal distributions with μ = 180 μm and σ = 180/2.5 μm) are shown in Figure 12. For all simulations, a solid mass ratio of 100 g/L was initialized. The solution was assumed to be saturated when starting the cycling procedure. For this model the solubility was adopted from the ASA solubility in ethanol using the Nývlt model presented by Maia.[142]

As discussed formerly by our group the population balance equation describing the temporal behavior of the crystal size distribution in a single segment (each segment is assumed to be a single decoupled reactor) moving through the tube of length x_tube at a speed of u_s=x_tube/t can be written as

$$\frac{\partial f(L,t)}{\partial t} + \frac{\partial (G(L,t) \cdot f(L,t))}{\partial L} = 0 \quad (2)$$

Here f denotes the number of particles with the internal coordinate L (i.e., the length of the cubic crystals, see Equation 1) at time $t = x_{tube}/u_s$. The used model solves equation 2 with f being number of particles per liter of suspension. G is the crystal growth rate which is positive in the case of growth and negative in the case of dissolution. Equation 1 does not account for changes in f due to aggregation and/or breakage or nucleation. If the growth rate is modelled to be size independent, Equation 1 can be simplified further by placing G in front of the brackets, i.e., not differentiate G with respect to L.

In the used model concentrations of the solute (c_{diss}), i.e., the dissolved molecules which are not in the crystalline phase, are presented in mol/L and changes were calculated via

$$\frac{\partial c_{diss}}{\partial t} = \frac{\partial c_{diss}}{\partial \left(\frac{X_{tube}}{u_{fs}}\right)} = -\frac{3}{M_w} \cdot k_v \cdot G \cdot \varrho_c \cdot \int_0^\infty f(L,t) \cdot L^2 \cdot dL \tag{3}$$

with the molecular weight MW = 180 g/mol and the density of the crystalline phase ρ_c = 1400 kg/m^3.

The PBE was solved using the class-method (CM) by Kumar and Ramkrishna[143] with more than 20,000 classes to discretize the crystal size distribution. The CM translates the partial differential equation 2 into a set of ordinary differential equations which was solved together with the mass balance equation 3 using Matlabs ode45 solver.

For positive growth rates, i.e., if the solution was supersaturated, a semi-empirical expression for G was used as in Lindenberg et al.[104]

$$G = k_{G1} \cdot e^{\left(-\frac{k_{G2}}{R \cdot T}\right)} \cdot c_{diss} \cdot \left(\frac{c_{diss}}{c^*} - 1\right)^{k_{G3}} \tag{4}$$

In equation 4 c^* denotes the solubility of ASA, c_{diss} is the actual concentration of the solute, T the temperature (here in Kelvin) and R the gas constant in $J/(mol \cdot K)$. The used parameters are listed in Table 8. These parameters were chosen to have crystal growth of $\sim 3\ \mu m/s$ if the supersaturation $S = c_{diss}/c^* = 1.5$.

Table 8: Growth rate parameters for crystal growth (Equation 3)

Parameter	Value
k_{G1}=	$22.47 \cdot 10^4$ $[\frac{\mu m}{s}]$
k_{G2}=	$2.58 \cdot 10^4$ $[\frac{J}{mol}]$
k_{G3}=	1.00 [−]

For negative growth rates, i.e., if the solution was undersaturated, a semi-empirical expression for G was similar to Nagy et al.[99]

size independent dissolution rate

$$G = k_{D1} \cdot \left(\frac{\varrho_{sol}}{M_w} \cdot (c^* - c_{diss})\right)^{k_{D2}} \cdot (1 + k_{D3})^{k_{D4}} \tag{5}$$

size dependent

$$G(L) = k_{D1} \cdot \left(\frac{\varrho_{sol}}{M_w} \cdot (c^* - c_{diss})\right)^{k_{D2}} \cdot (1 + k_{D3})^{k_{D4}} \cdot (1 + 1/e^{(1/100 \cdot L)}) \tag{6}$$

The used parameters are listed in Table 9. These parameters were chosen to have crystal dissolution of ~ 6 µm/s if the supersaturation $S = c_{diss}/c^* = 0.5$.

Table 9: Growth rate parameters for crystal growth (Equation 5)

Parameter	Value
k_{D1}=	51.216 $[\frac{\mu m}{s}]$
k_{D2}=	0.9801 [−]
k_{D3}=	0.0202 [−]
k_{D4}=	0.8604 [−]

Results not shown in the main article

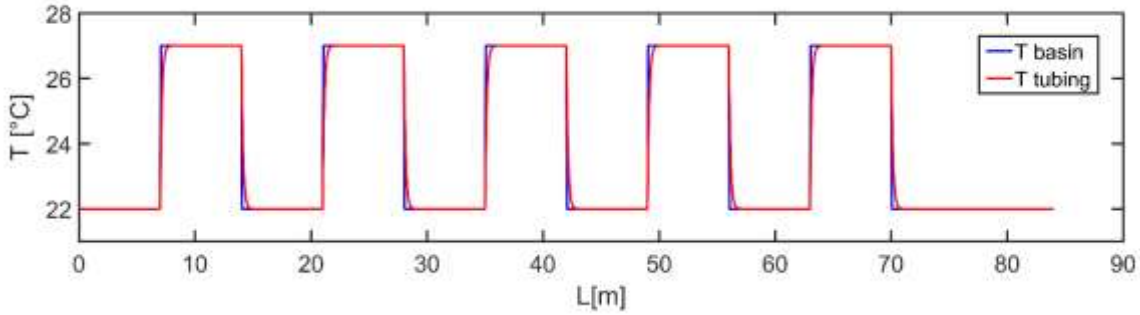

Figure 21**:** Temperature profile in the tubing, i.e. the segments, during temperature cycling.

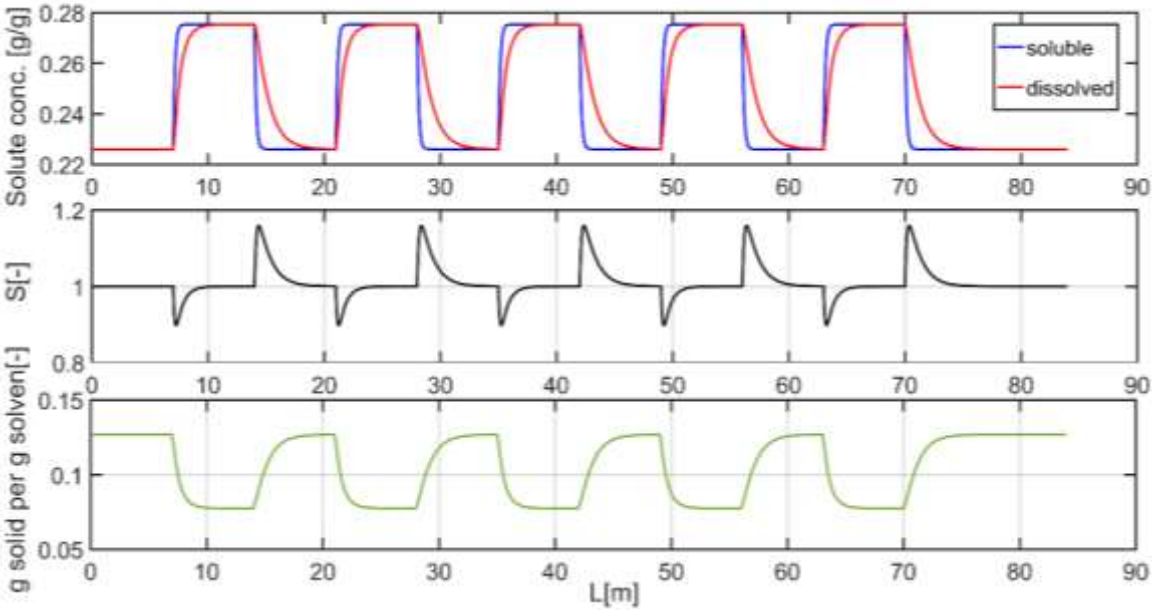

Figure 22: Concentration of dissolved species, supersaturation and amount of solid material during temperature cycling (size independent dissolution rate). The tube length (7.5 m in the heating and cooling basin) were chosen to allow equilibration (S=1) after every heating and cooling step.

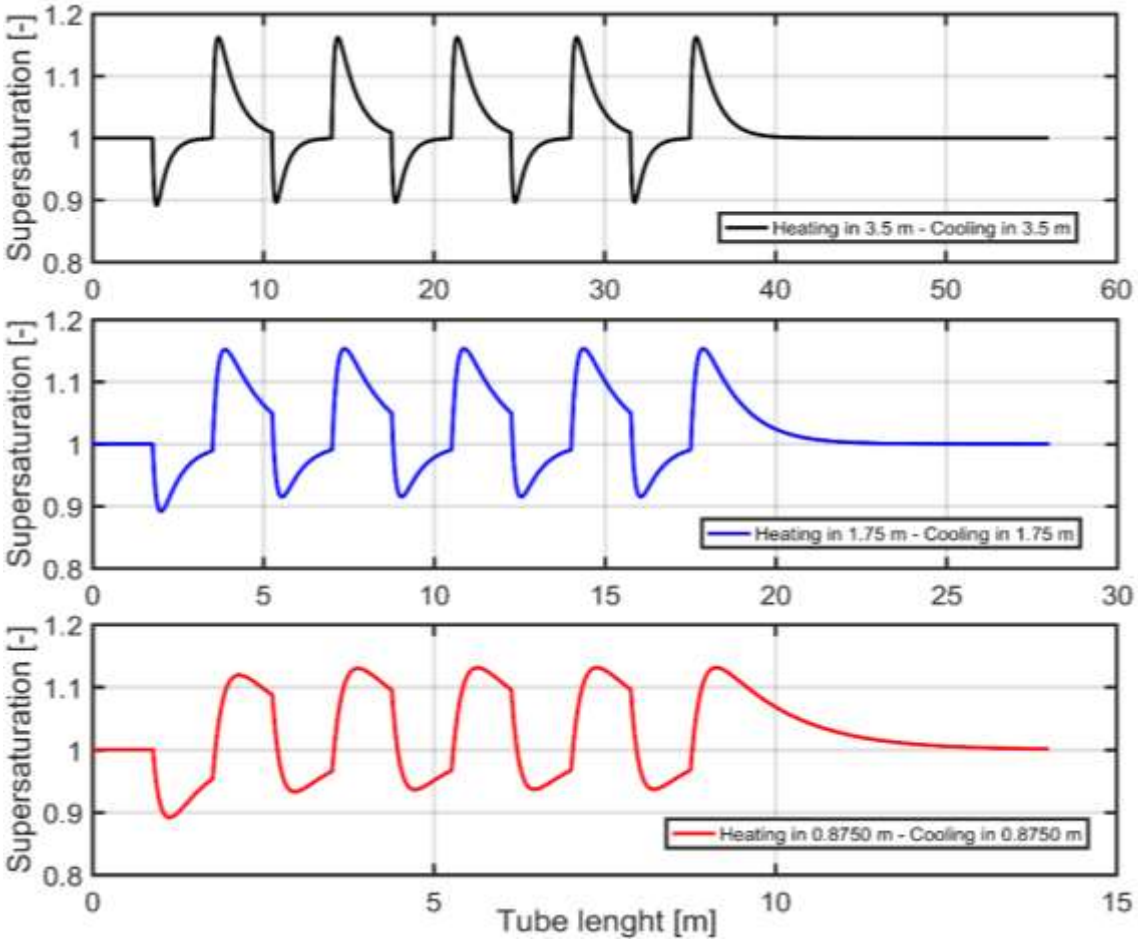

Figure 23: Supersaturation profiles during temperature cycling in different tube length but identical flow rates and temperature gradients (calculated using the size dependent dissolution model).

Quantification of α- and β-polymorph ratio via Raman spectroscopy and multivariate analysis

A multivariate approach, i.e., a PLS model, was chosen to quantify the fraction of the α polymorph in a powder mixture consisting of the α- and β-polymorph via Raman spectroscopy. The part of the Raman spectra used for multivariate analysis is shown in Figure 24.

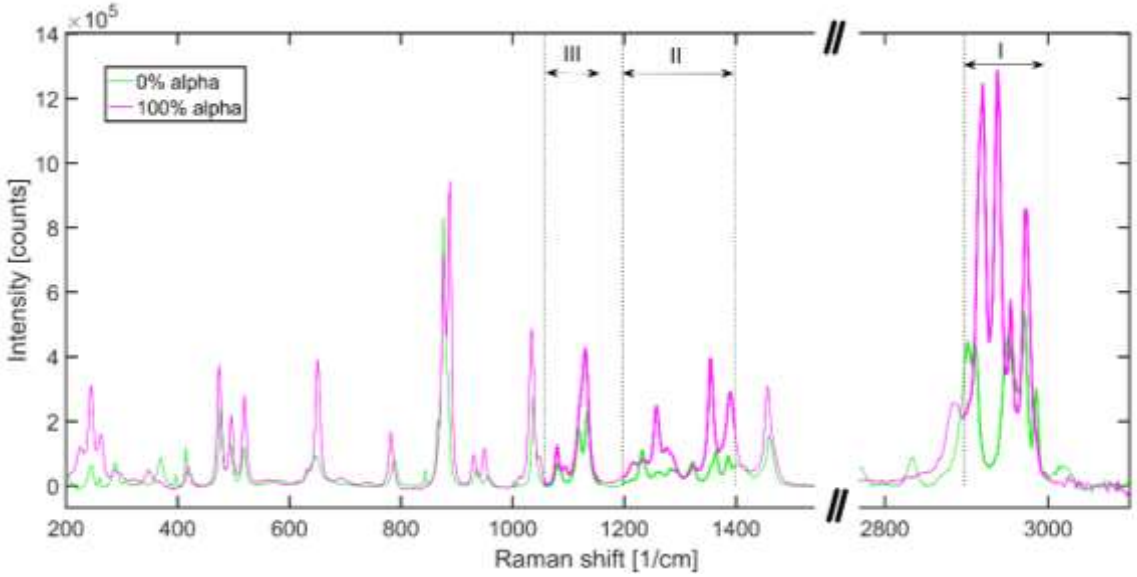

Figure 24: Raman spectra of α and β (= 0% α) polymorph (α-form: spray-dried type, non – commercial; β-form: Pearlitol 160C, both from Roquette, France, as received). The multivariate model used spectral data from regime I (2900-3000 cm1), II (1200-1400 cm1) and III (1060-1160 cm1) only.

To calibrate the PLS model 13 powder blends of a known α and β composition were prepared to record their Raman spectra. For each powder blend ten spectra where recorded at 100 different positions (= 1000 measurements per blend/sample) and then averaged. This was necessary to achieve consistent results, especially when the fraction of the α- or β polymorph was low. Before performing the PLS, the spectral data of regime I-III have been merged (203 wavenumbers 203 data points) and normalized by equalizing the area under the merged spectra. The normalized intensities in the selected parts of the Raman spectra of the samples used for calibration are shown in Figure 25.

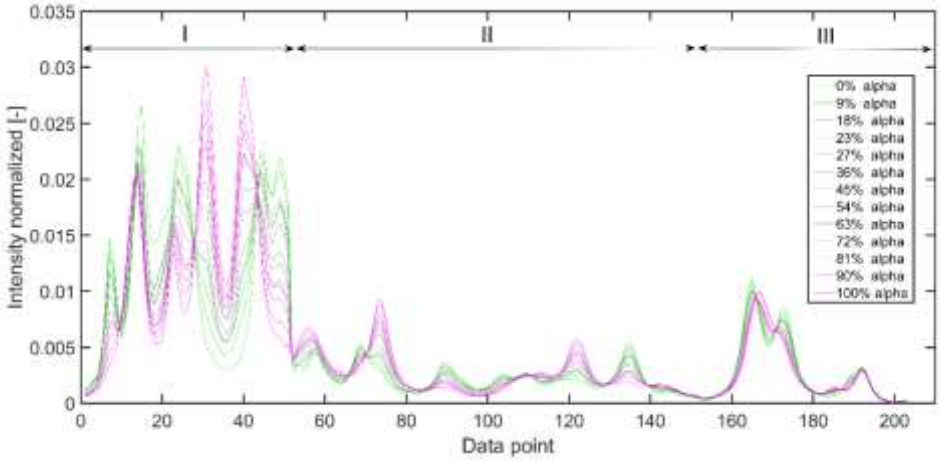

Figure 25: Normalized intensities of the selected parts of the Raman spectra. The arrows indicate the regime the data points originate from (same notation as in Figure 24).

These normalized intensities of the 13 samples were united in the matrix $\boldsymbol{X}$ (13 rows, 203 columns) and the data of each column were mean-centered and scaled to unit variance. The PLS as defined in equation S6 was calculated using Matlabs® (R2016a, Mathworks, Natick, USA) statistic toolbox and the inbuilt function *plsregress*.

$$\boldsymbol{X} = \sum_{a=1}^{A} t_a \boldsymbol{p}_a^{\mathrm{T}} + \boldsymbol{E}$$
$$\boldsymbol{Y} = \sum_{a=1}^{A} t_a \boldsymbol{q}_a^{\mathrm{T}} + \boldsymbol{F} \qquad \text{(S6)}$$

$\boldsymbol{Y}$ denotes the standardized (mean-centered and scaled to unit variance) observables, i.e., the fractions of the alpha polymorph. The exact fraction values are shown in Figure 26. a stands for the PLS dimension ($a = 1, 2, \ldots, 12, 13$). $\boldsymbol{p}_a$, $\boldsymbol{q}_a$ are the corresponding weighted loading vectors. $\boldsymbol{E}$ and $\boldsymbol{F}$ contain the remaining discrepancy between the PLS model and the data.

In order to avoid overfitting, the mean squared error of prediction using cross validation ($MSECV$) was determined as defined in equation S7. The $MSECV$ quantifies the discrepancy between the predicted α fraction $\widehat{\boldsymbol{Y}}_{PLS\,i}$ (calculated by a PLS model generated from data of the $13-3$ samples) and $\boldsymbol{Y}_i$, i.e., α fraction in the 3 samples not used for model generation in the cross validation. This cross validation was performed 100 times, i.e., 100 models have been generated to evaluate 300 spectra.

$$MSECV = \frac{1}{100 \cdot 3} \cdot \sum_{i=1}^{100} \left\{ \sum_{k=1}^{3} \left(\widehat{\boldsymbol{Y}}_{PLS\,i,k} - \boldsymbol{Y}_{i,k} \right)^2 \right\} \tag{S7}$$

As expected the minimum $MSECV$ of < 10 % α-fraction was achieved when using only the first latent variable ($a = 1$). This is because of the linear relation between Raman intensity and concentration. Since $MSECV$ was in the range of 10% the error in the predicted α content is expected to be in the range of $\pm\sqrt{10}$ % (i.e., error $< 4\%$). The model-prediction plot (using all 13 samples) is shown in Figure 26.

The Matlab files used for model development and spectra analysis are made available for download at the journals website.

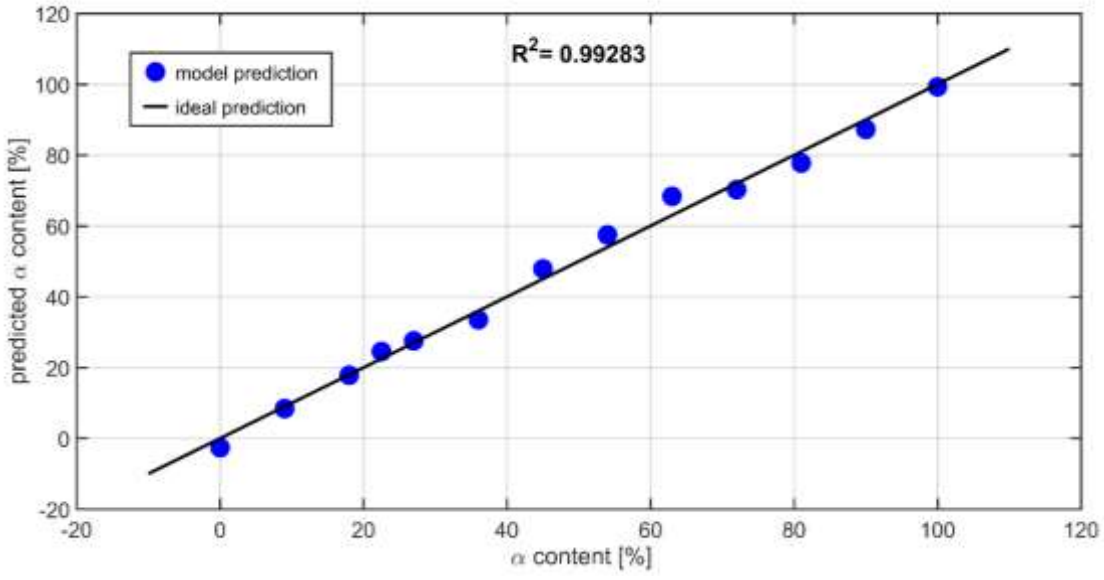

Figure 26: Model prediction of PLS model to quantify the α content. The ideal prediction is equivalent to the 1st median.

Determination of D-Mannitol solubility in water-ethanol solutions

The solubility of D-Mannitol (β-form) was obtained via density measurements as described by our group.2 Solutions of known D-mannitol (β-form, Pearlitol 160C, Roquette, France, as received) concentrations in a 50:50 water-ethanol mixture and 40:60 water-ethanol mixture were prepared and their density was measured via the DM4500 (Anton Paar, Graz, Austria) densitometer. Solution preparation and density measurements were performed at 45°C, i.e., a temperature higher that the highest temperature of interest for the solubility measurements. The high precision densitometer allowed to correlate the density of the solution accurately with the D-Mannitol concentration, see Figure 27 and Figure 28 (top). The solubility was measured by sampling the supernatant of a D-Mannitol (β-form) suspension that was stirred at the defined temperature for >2h through a filter. Density measurements of the withdrawn supernatants allowed to determine their concentration, see Figure 27 and Figure 28 and (bottom).

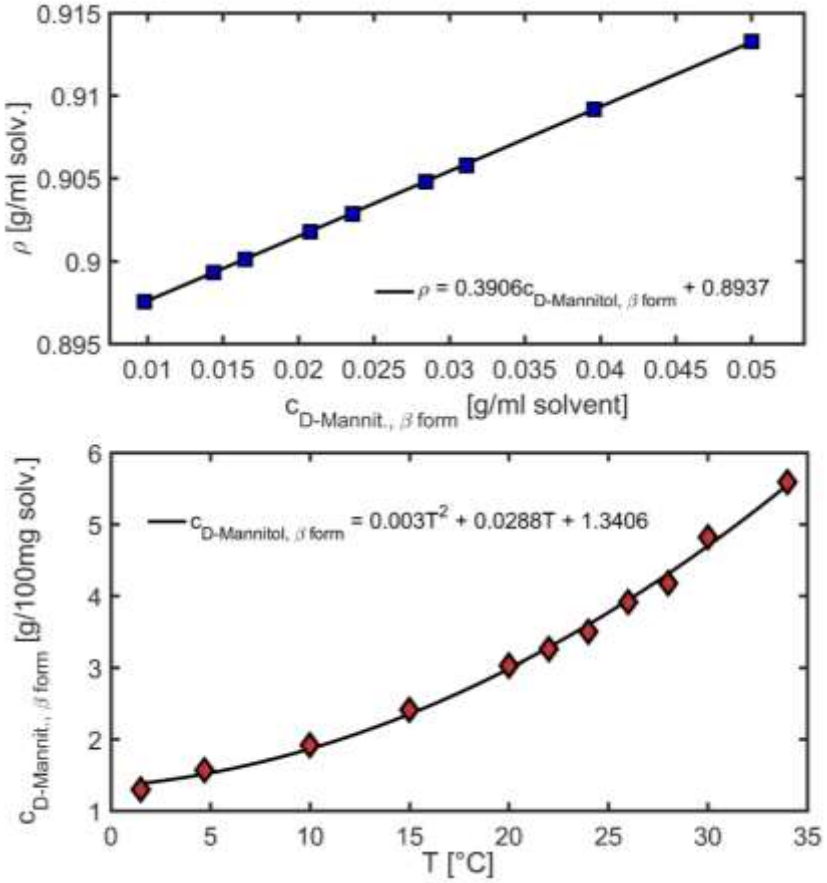

Figure 27: Solubility of D-Mannitol in a 50% water 50% ethanol (w/w). (top) Calibration curve, i.e., density of solutions with a known concentration measured at 45 °C. (bottom) Solubility curve obtained by measuring the density of the supernatant at 45 °C and the calibration curve (density of solvent = 0.8937 g/ml).

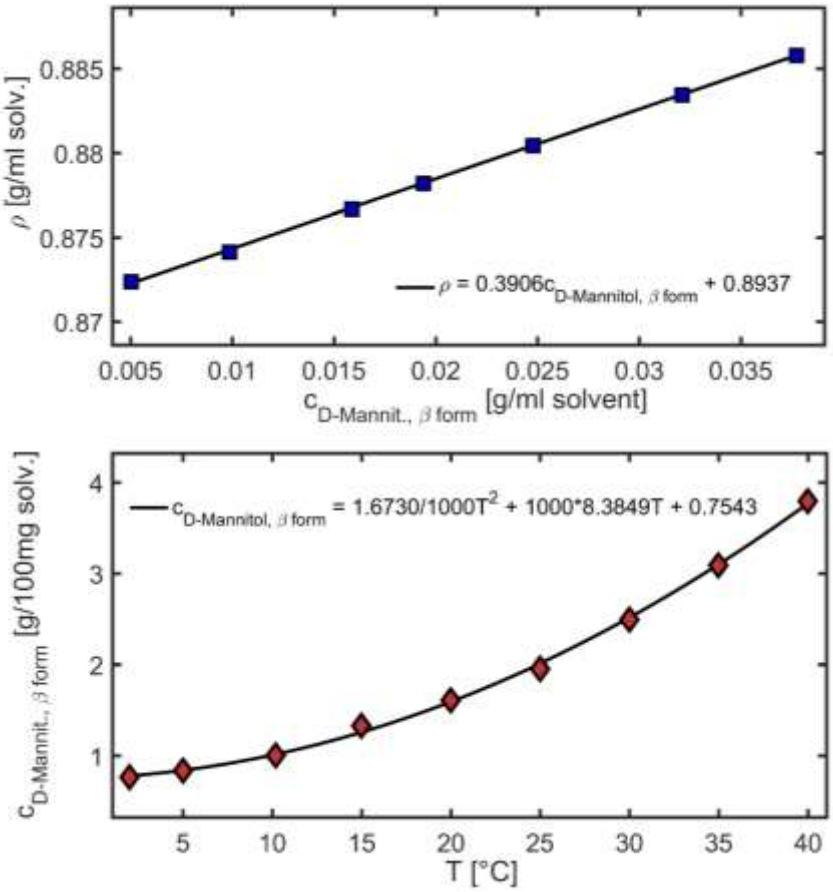

Figure 28: Solubility of D-Mannitol in a 40% water 60% ethanol (w/w). (top) Calibration curve, i.e., density of solutions with a known concentration measured at 45°C. (bottom) Solubility curve obtained by measuring the density of the supernatant at 45°C and the calibration curve (density of solvent = 0.8937 g/ml).

Estimation of temperature profiles

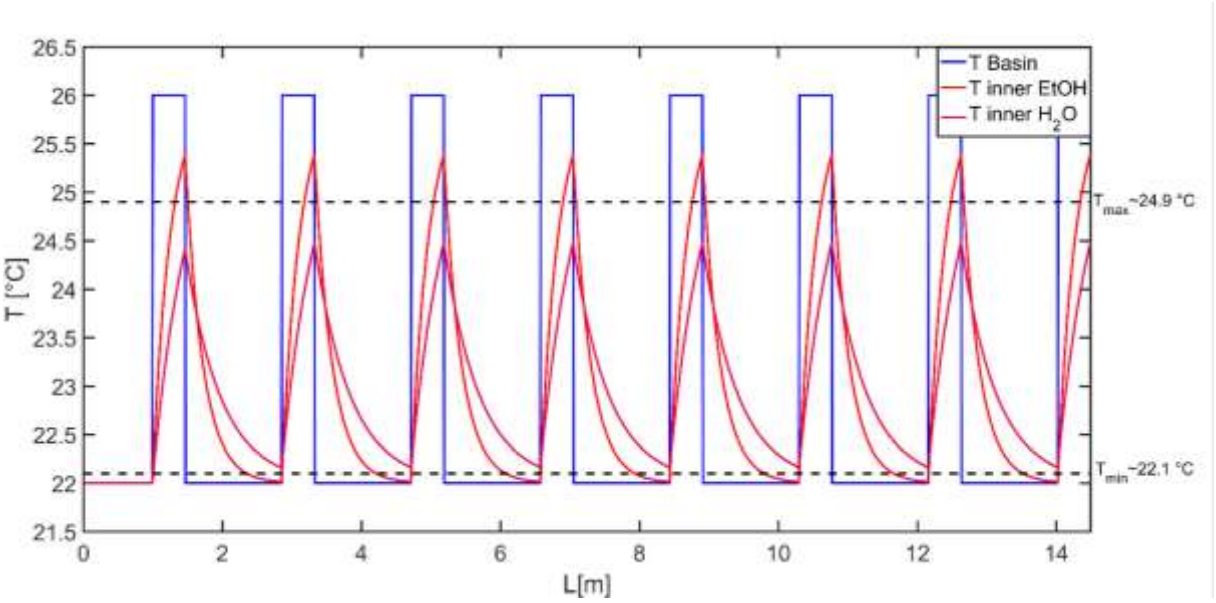

Figure 29: Estimated Temperature profile for pure water and ethanol in the tubing using the settings of the fine frapping studies (Delta T=6 °C).

Based on the temperature profile (calculated as described in section 3.3 and previously by our group) and the process settings of the fine trapping studies (see section 3.3), as well as the heat capacities, densities, thermal conductivities and viscosities (the last three are used to calculate the Nusselt numner/heat transfer coefficient) of pure water and ethanol, the maximum temperature was estimated as T_max= 24.9°C and T_min= 22.1°C, (see Figure 29). T_max was estimated as in the middle of the maximal temperature obtained during cycling of a pure ethanol and a pure water solution. The minimum temperature was estimated similar but with a slight offset to the higher temperature. The latter is because the air gap (2 X 10 cm), i.e., the part of the tube that was not immersed in the water bed, was added to the 22°C batch although the heat transfer coefficient in air is lower (hence cooling is slower). Using the solubility for 50% water 50% ethanol (w/w) solutions shown in Figure 27 these temperatures correspond to a maximum under saturations of S_min= 0.85 (S_(22°C)=1).

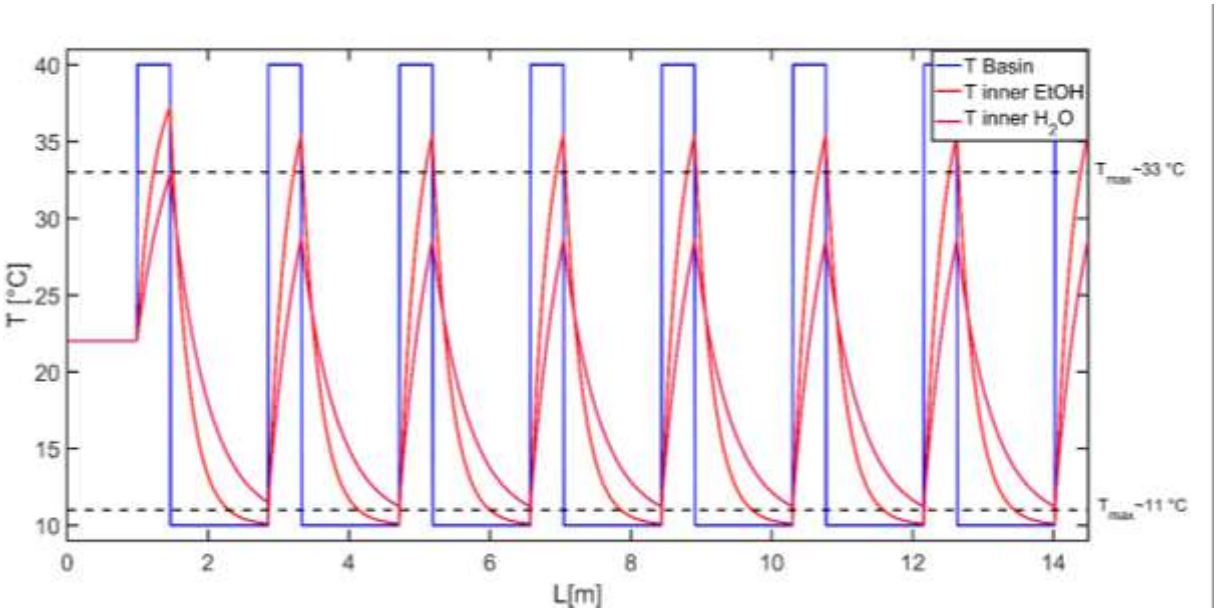

Figure 30: Estimated Temperature profile for pure water and ethanol in the tubing using the settings of the polymorphism control studies (Delta T=30 °C). Maximal and min

Using the same concept as in the previous section but the process settings of the polymorphism control studies (see section 3.5) the maximum temperature was estimated as T_min= 11°C and T_max= 33°C, see Figure 30). Using the solubility for 40% water 60% ethanol (w/w) solutions shown in Figure 28 these temperatures correspond to a maximum under saturations of S_min= 0.7 and S_max= 1.9 (S_(22°C)=1).

4 Crystal Shape Modification via Cycles of Growth and Dissolution in a Tubular Crystallizer[d]

Abstract. Besides size and polymorphic form, crystal shape takes a central role in engineering advanced solid materials for pharmaceutical and chemical industry. This work demonstrates how multiple cycles of growth and dissolution can manipulate the habit of an acetylsalicylic acid crystal population. Considerable changes of the crystal habit could be achieved within minutes due to rapid cycling, i.e., up to 25 cycles within <10 min. The required fast heating and cooling rates were facilitated using a tubular reactor design allowing for superior temperature control. Furthermore, the effect of the solvent on the crystal habit was studied testing commonly used solvents of different polarities. The face specific interactions between solvent and the crystals' surface result in face specific growth and dissolution rates and hence alterations of the final shape of the crystals in solution.

Accurate quantification of the crystal shapes was essential for this work, but is everything except simple. A commercial size and shape analyser had to be adapted to achieve the required accuracy. Online size, and most important shape, analysis was achieved using an automated microscope equipped with a flow-through cell, in combination with a dedicated image analysis routine for particle tracking and shape analysis. Due to the implementation of this analyser, capable of obtaining statistics on the crystals' shape while still in solution (no sampling and manipulation required), the dynamic behaviour of the size shape distribution could be studied. This enabled a detailed analysis of the solvent's effect on the change in crystal habit.

[d] This chapter is based on a journal paper by Neugebauer et al. submitted to Crystal Growth and Design.

4.1 *Introduction*

In addition to being a technique for separation and purification, crystallization from solution has become an important tool for the production of advanced solid materials with well-defined, "engineered" properties. Depending on the respective end-use of crystalline materials, crystal engineering targets three key aspects that determine the functionality/quality of the material: i) crystal size and size distribution, including the issue of fines material minimization, ii) control of molecular arrangement in the crystal lattice (polymorphic state) and the associated defect structure, and iii) the crystal shape distribution. The first two issues have received much attention for many decades. Recently however, shape control (i.e., control of the crystal habit) has become a field of increasing interest due to its central importance for specialty applications. Handling and mechanical stability issues, as well as difficulties associated with solid-liquid separation are concerns for certain shapes, including needles, acicular or dendritic shapes, platelets or flakes. Thus, a robust three-dimensional growth to form stout crystals of approximately similar dimensions is the desired mode of crystal formation. For some applications, however, high specific surface areas are desired, e.g., associated with plate-like or reticulated crystal shapes, since this enhances the dissolution rates of dissolution-rate limited APIs. Also other specific applications make use of fragile crystal forms, e.g., ZnO nanowires in solar cells.[144] Besides geometric preferences, the changing presence and relative exposure of different crystal faces influences face-specific properties. Molecular crystals expose different sets of atoms or functional groups on each face, causing different interactions with the environment, e.g., the solute and solvent molecules. For example, the wetting behaviour of crystal faces, being related to the specific surface energy via Young's equation, has shown to be anisotropic.[48] Other properties of interest for the pharmaceutical industry are the dissolution behaviour[145], the catalytic potential and the chemical stability[146].

During crystallization many parameters govern the final shape of the product. Early studies correlated the final shape with the internal structure of the crystalline lattice.[147,148] In the case of strong lateral interactions between molecules of a certain face the surface density increases, leading to higher stabilities and slower perpendicular growth rates of the respective face. Therefore, it eventually becomes a dominant face.[149] Early research about the interaction of molecules in the solid state facilitated equilibrium shape calculations using force-fields implemented in computer programs, such as HABIT[150] and Morang[151]. Yet, these theoretical approaches could not take into account the influence of foreign molecules, such as the solvent, and, therefore, could not predict the shape of solution-grown crystals. Factors, such

as solvent, additives, impurities and supersaturation, impact the mechanism of the incorporation of molecules into the crystal's surface, which is neglected by these models. The mechanism of crystal growth can change between spiral growth, 2D nucleation and growth, and rough growth - all differing in terms of rate of incorporation of solute molecules into the crystalline lattice.[152,153] Microscopic techniques can be used to determine each face's steady-state growth kinetics, based on the measured crystal size and shape distributions under constant process conditions.[53,154] *A priori* predictions of the exact perpendicular growth rates for each face of a faceted crystal (e.g., using the Frank-Chernov condition[155,156]), though, are still not feasible, particularly regarding the influence of supersaturation. At low supersaturations crystal growth is diffusion limited and spiral growth is the prevailing mechanism.[154,157] Kink sites, being positions were molecules will incorporate most readily on the surface appear only in a small number on flat faces during spiral growth. Therefore, respective growth rates are low. At high supersaturations (when crystal growth is surface-integration limited) growth rates are at least one order of magnitude higher. This is due to a high surface nucleation rate and the high density of kink sites present, resulting in so-called "rough growth".[53] The transition between these mechanisms, though, is hard to predict.

Also, the number of kink sites on a specific surface of a crystal is not only influenced by the supersaturation: All molecules present in a given solution will interact with a crystal's surface. In the case of molecules for which the free energy of the system decreases upon interaction, the number of kink sites on the respective face is increased (and vice versa in the case of dissimilar molecules).[149]An overview of solvent effects can be found in the work of Lahav and Leiserowitz[152] and Davey[158] and is reviewed in the paper of Lovette et al.[53], underlining the fact that the fastest growing face governs the steady-state crystal shape.

Due to the many parameters influencing the incorporation of molecules into surface in a yet unclear manner, modeling depends on certain simplifications. For example, Zhang et al.[159], while modeling the shapes of a population of crystals grown in a homogeneous solution, assumed constant kink free energies over the whole crystallization process. The associated calculations resulted in crystals developing towards a fixed (steady-state) shape, i.e., all crystals follow the same shape evolution trajectory.[149,154,160]

In the present work, the attainable shapes of acetylsalicylic acid crystals are investigated when exposed to cycles of growth and dissolution using a tubular crystallizer. In contrast to experiments where growth alone determines the final shape of a crystal population, the number of attainable shapes is significantly expanded, due to crystal dissolution mechanisms differing from mechanisms of crystal growth.[161] In contrast to crystal growth, during

dissolution crystal shapes are generally dominated by fast moving planes or, in other words, the planes with the fastest rate of dissolution will eventually become visible/dominant. This was elaborated by Snyder and Doherty[153], discussing mechanisms of dissolution at low undersaturation in detail. Similar to crystal growth, concerning most real organic crystals, at low undersaturation the spiral dislocation mechanism is prevailing, whereas at higher undersaturation 2-D nuclei become the main source of steps and kinks.

Unique for dissolution though, is the event of creating new faces bifurcating from edges and vertices. These stepped and kinked faces are assumed to have not only high relative perpendicular growth rates but also high relative dissolution rates (due to their diffusion-limited nature instead of slow surface-integration-limitation).[149] Therefore, during growth they become "virtual" faces and are not visible in the habit of the crystal, but eventually become dominant during dissolution.

Based on the 3D evolution models developed by Snyder et al.[54] numerous different shapes can appear for a faceted crystal after multiple cycles of growth and dissolution (assuming regrowth to the original crystal volume after each cycle). Clearly, the central requirement for a shape change to happen is that the rates of growth and dissolution for at least one crystal face are not equal. This can be realized via one of the following ways: I) As discussed above additives and specific solvents have face-specific interactions with the crystal surface. This interaction will generally be less important for dissolution, resulting in unequal rates. II) Different mechanisms for growth and dissolution may occur due to super-/undersaturation effects. III) During dissolution faces which are present in the steady-state growth shape might disappear, therefore becoming "virtual" faces, showing different perpendicular growth rates during regrowth until they reappear on the surface. Simultaneously, new faces might appear during dissolution due to bifurcating edges and vortices.

In the present work, cycles of growth and dissolution for a starting population of acetylsalicylic acid (ASA) crystals suspended in their saturated solution resulted in a change of shape via usage of solvents of different polarities. The known crystal morphologies of ASA grown in different solvents can be found in literature. Following the indexing by Aubrey-Medendorp et al.[162] throughout this work, the two major faces appearing during ASA crystal growth are referred to as the (100) and the (001) face, besides two minor faces, referred to as the (011) and the (110) face[113], see Figure 31.

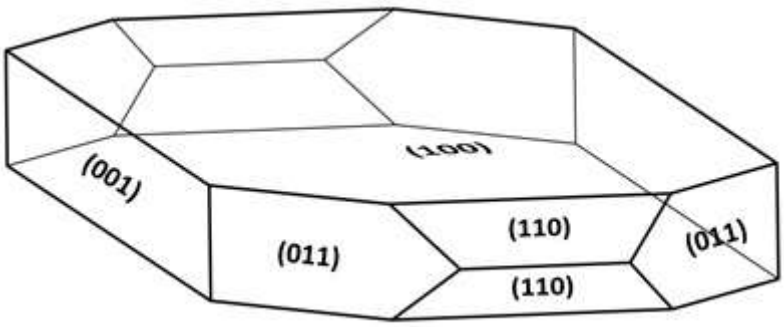

Figure 31: Growth morphology of acetylsalicylic acid (adapted from ref.[162])

The relative exposure of these faces, though, is strongly influenced by the solvent in which crystals grow. Polar solvents, such as ethanol, methanol and acetone were shown to result in plate-like crystals of ASA with a dominant (100) face. Non-polar solvents like hexane and n-heptane are reported to yield needle- or rod-like shapes, with fast molecule addition remaining on the (011) face, therefore becoming a small face relative to the major faces.[113,163–165]

The interaction of solvent molecules with the ASA crystal's faces was investigated for ethanol and hexane using molecular dynamics simulations.[166] According to the specific arrangement of strong H-bonds between ASA molecules' carboxyl groups in the crystal, their exposure on the (100) face is unfavorable, leading to the (100) face being less hydrophilic, i.e. less polar, than the (001) face. Therefore, while being in contact with a polar solvent like ethanol, growth on the (100) face occurs in a layer-by-layer manner being kinetically unfavorable. The more hydrophilic nature of the (001) face prefers the interaction with a polar solvent and thus growth along this face is accelerated when in contact with ethanol. On the (011) plane, the interlaced arrangement of hydrophilic hydroxyl groups and hydrophobic phenyl groups enables fast thermodynamically and kinetically favored single molecular addition.[162,166]

In this study, the first set of experiments focused on a single solvent (ethanol) to induce shape tuning by applying 5, 10, 15, 20 and 25 temperature cycles We show that a continuously operated crystallizer, including a setup for temperature cycling, can alter the habit of a crystalline population due to the relative rates of growth and dissolution of various crystal faces. In a second set of experiments, we focused on the effect of three different solvents to induce shape tuning by applying 25 temperature cycles within a short time range of several minutes. The individual effect of ethanol, isopropanol and hexanol, which are part of the homologous series of alcohols was compared. The experimental studies of the dynamic change of crystal shapes were facilitated by the implementation of an automated microscope and the development of dedicated particle tracking and shape analysis routine.

4.2 *Materials and Methods*

4.2.1 Set-up and Equipment

In the present study, cycles of growth and dissolution are made possible using a continuous tubular crystallizer set-up. Among many advantages of tubular crystallizers, substantiated experimentally in earlier publications of our group[35–38,58,65,167–171], high heat-transfer rates enable fast temperature changes and, therefore, changes of the saturation. A set-up allowing rapid change of the saturation levels, with the aim to continuously engineer crystals, has been presented recently[5] and was adapted for this study focusing on shape tuning and online image analysis. A schematic of the tubular temperature cycler is given in Figure 32. To implement alternating heating and cooling stages for dissolution and growth of crystals, water baths were used in which successive parts of the tubular crystallizer were immersed.

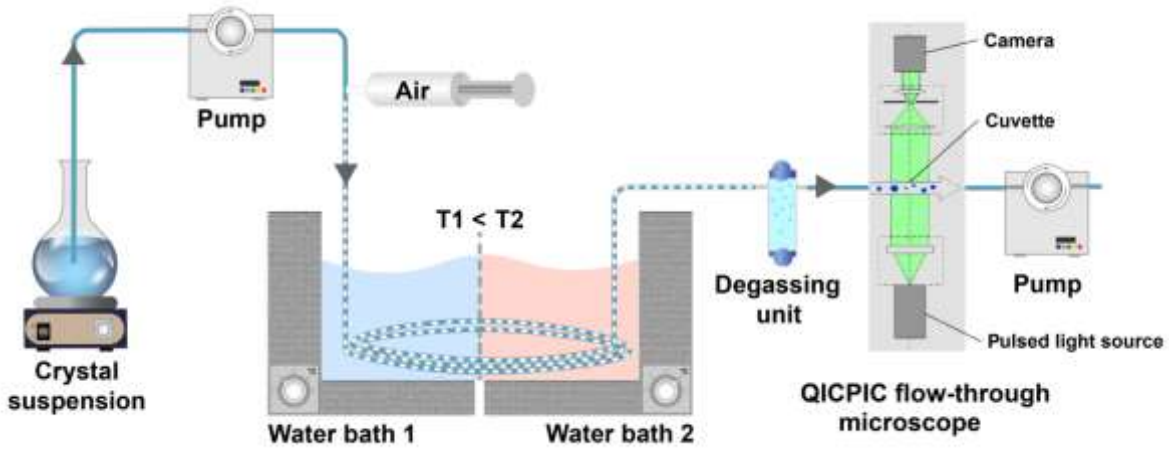

Figure 32: Setup of the tubular crystallizer

In the setup a polysiloxane tubing with an inner diameter of d_{in}=2 mm was used, cycling the crystal suspension between water baths, resulting in sections of 1.86 m per cycle (2 × 83 cm inside the cold and warm water baths, and 2 × 10 cm for the connections in between). For each loop, the suspension first passed the section immersed in the cold bath, followed by the warm water bath. Depending on the respective experiment, the overall number of loops varied from 5 to 25, with 1 m of tube at the inlet and 1 m at the outlet. The maximum overall length therefore was 48.5 m.

To achieve controlled transport of crystals in the crystallizer a segmented flow was established. Using two syringe pumps (LA-120, HLL Landgraf, Germany), a continuous air supply to the crystallizer was facilitated via a T-fitting. The suspension was pumped through

the tubing using a peristaltic pump (Digital MS-2/6, Ismatec, USA) at $\dot{V}_{Susp}$ = 7.0 mL/min. Flow rate of air was 2.8 mL/min.

Commercial ASA (ASS3020, GL Pharma, Austria) was used as a model substance in all experiments. By sieving the received ASA (sieve fraction between 90µm and 200 µm), rod-like crystals were separated and subsequently suspended in a saturated aqueous solution, i.e., the starting suspension. The starting suspension was continuously stirred at 22°C at sufficient speed to simultaneously prevent sedimentation and to avoid breakage of the crystals (stir bar: 4 × 0.5 cm, 500 rpm). To study the influence of the solvent's polarity on the resulting shape three different solvents were selected: 1) 1-hexanol (≥ 98%, Carl Roth GmbH, Germany), 2) 2-propanol (isopropanol, laboratory reagent grade, Fisher Scientific GmbH, Austria) 3) ethanol 99.8% (≥ 99.8% denatured, Carl Roth GmbH, Germany). The chemical and physical properties of the used solvents are listed in Table 1. In these solvents, ASA shows a decreasing solubility with increasing length of the hydrocarbon backbone and decreasing polarity.

Table 10: Properties of pure solvents at room temperature

Solvent	T_s [°C]	ρ [kg/L]	µ [mPas]	ε [-]
Ethanol	78	0.789	1.2	25
Isopropanol	82	0.78	2.2	18
Hexanol	157	0.81	5.9	13

For online product analysis a QICPIC automated microscope (pixel size = 19.63 µm, software version: WINDOX 5.6.0.0, Sympatec, GmbH, Germany) was installed, equipped with a flow cell (LIXELL, optical path length = 2 mm, diameter of window = 33 mm, Sympatec GmbH, Germany). At the outlet of the tubular temperature cycler, a stirred 50 mL round-bottomed flask kept at 22°C via a thermostatic bath beaker was installed for degassing. Whenever 35 mL of product suspension were collected in the beaker, they were pumped at a higher flowrate of 90 mL/min through the QICPIC system, which recorded videos at 450 fps (measurement duration: 20 s each, range of size: 4.5 – 800 µm). The videos were analyzed using an in-house Matlab routine as described below.

Figure 33 shows details of single frames from the videos taken by Sympatec's QICPIC, which were the basis for all further analysis.

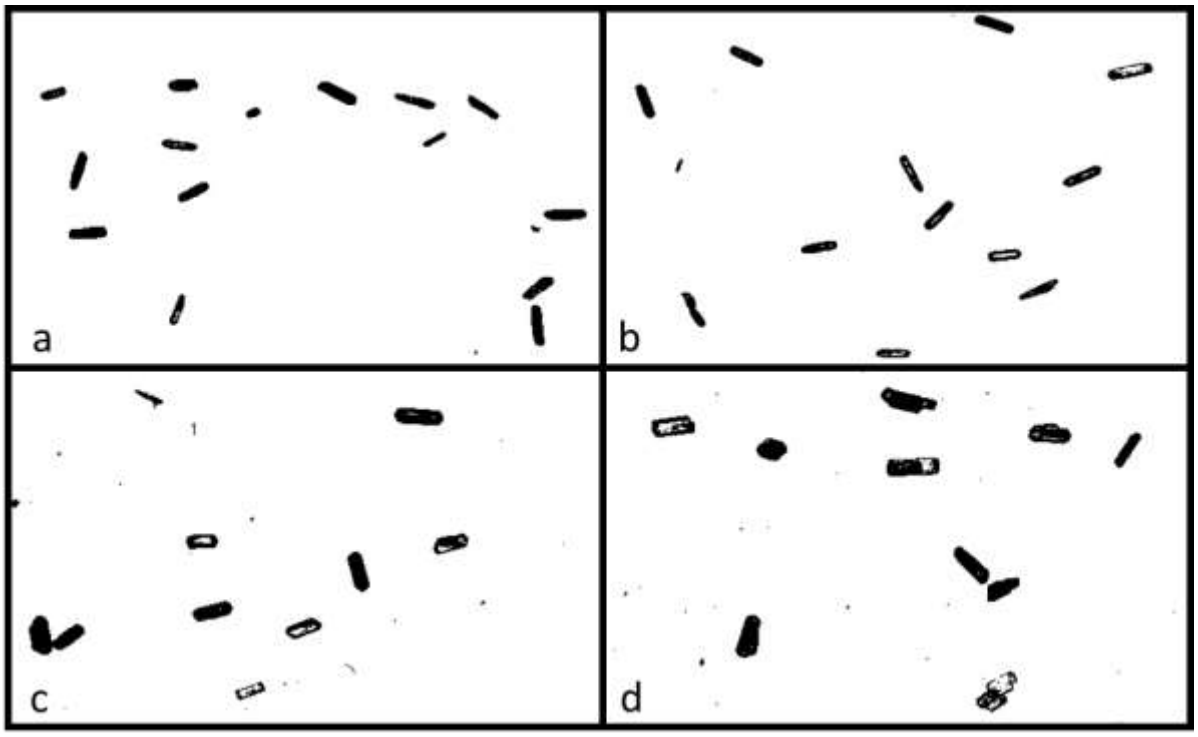

Figure 33: Details of single non-consecutive frames captured by QICPIC, showing a) the seed crystals, b) product in 1-hexanol, c) product in isopropanol, d) product in ethanol.

4.2.2 Process Settings

During the first set of experiments the change of crystal shape after 5, 10, 15 and 20 cycles was investigated using ethanol as a solvent and compared to the results after 25 cycles. The second set of experiments were focused on crystal-shape tuning via temperature cycling utilizing three different solvents, i.e., ethanol, isopropanol and hexanol. In order to easily compare results, the temperatures in the water baths were chosen such that for all solvents the same maximum under- and supersaturation of S_{min} = 0.89 and S_{max} = 1.23 were achieved. The supersaturation S is defined as the ratio of concentration and true solubility $S = c/c^*$.

Due to the different solubility for each solvent, the amount of dissolved material (solute) available for deposition during crystal growth varies, dependent on the solvent. To compensate for this effect, the ratio of $m_{Seeds}/m_{ASA\ dissolved}$ was kept constant at 1% for all solvents used. Thereby, the concentration of seeds in the starting suspension was low enough to minimize aggregation of the particles and, in addition, did not exceed the critical optical density for QICPIC measurements. Due to the small amount of seeds and the short residence times in each water bath, the solution concentration (as a means for calculation of the super- and under-saturation) was considered constant along the tubular crystallizer. The settings for each experiment are summarized in Table 2. Solubility data of ASA were either taken from

literature (ethanol and isopropanol)[142], or determined via density measurements (hexanol, see SI).

Table 11: Experimental settings used for first set of experiments, i.e., varying the solvent but keeping equal levels of supersaturation during temperature cycling. c* (22°C) = solubility of ASA in the respective solvent at the temperature of the starting suspension.

Solvent	**c* (22°C) [g/100 g solv.]**	**T (water baths) warm / cold**	**S_{max}**	**S_{min}**	**Amount of seeds (g seeds/100 g sat. sol.)**	$\frac{m_{seeds}}{m_{ASA\ dissolved}}$
Ethanol 99.8%	22.6	25.0 / 17.0°C	1.23	0.89	0.189	1%
Isopropanol	11.6	23.9 / 19.0°C	1.23	0.89	0.107	1%
1-Hexanol	5.4	24.3 / 18.6°C	1.23	0.89	0.053	1%

In a recent study[5] we reported on a computational approach to model the temperature profile in the tubular reactor during heating and cooling. For the present study, in combination with the solubility data of ASA in ethanol[142], isopropanol[142] and hexanol (see SI) the supersaturation profiles along the temperature cycler were calculated accordingly. This supports the determination of temperatures in the water baths to minimize net changes in crystal volume after each cycle, i.e. dissolved crystal mass in the warm water bath should be compensated by regrowth in the cold water bath (see Figure 34). During the cycling process the crystal's surface roughness and the relative exposure of different crystal faces (including their differing inherent perpendicular growth rates) vary. Therefore, face-specific perpendicular growth rates are non-constant and an exact prediction of crystal size behavior is not feasible. Accordingly, suitable levels of under- and supersaturation were determined via preliminary experiments using isopropanol, showing a polarity between the one of ethanol and hexanol. For the cold-water bath, its lowest temperature was given by the metastable limit of ASA, since nucleation should be excluded in all experiments. In the warm water bath, complete dissolution of the crystals had to be avoided.

As can be seen in Figure 34, the temperature and supersaturation change along the tubular crystallizer in a periodic manner. Despite the high heat transfer rates, the respective bath temperatures are only (asymptotically) reached at the end of each segment, and thus, for most of the crystallizer there is a transient change of supersaturation.

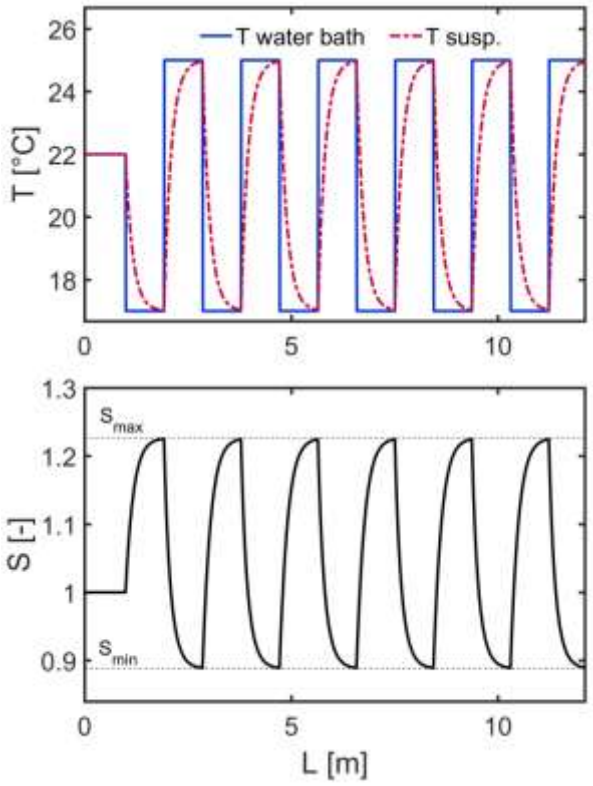

Figure 34: Modelled temperature- (top) and supersaturation (bottom) profile of ASA using ethanol as solvent during six temperature cycles

4.2.3 Image Analysis

Static image analysis, i.e., the standard post processing procedure, is generally performed offline, after a process of sampling, drying and dispersion, which possibly leads to some degree of particle change (e.g., via attrition) and thus, to biased results. Furthermore, only a small fraction of the entire crystal population can be observed. The QICPIC system collects 2D videos of particles at a rate of 450 frames per second (fps) as they pass through the LIXELL flow cell. Using this setup, particles are not exposed to mechanical stress. Moreover, the entire population is analyzed and consequently, the results are more representative. Finally, within a flow cell, particles revolve as they transit through the field of view of the camera and are observed from random directions, while static image analysis "sees" only the lowest energy orientation. Out-of-plane dimensions cannot be analyzed with standard microscopes.

Sympatec's QICPIC-software offers a frame-by-frame identification of particles. However, concerning shape analysis of particles, it has three major drawbacks: I) Since particle velocities in the flow cell are not constant (laminar velocity profile), particles that move slower are "seen" more often and, therefore, have a more significant contribution towards the

final size and shape distributions. II) During the passage of a single particle through the flow cell's field of view it is captured by the camera on several consecutive frames. Its revolving motion in the liquid stream and QICPIC's frame-by-frame identification of particles result in multiple sets of size characteristics for each particle, as illustrated in Figure 35a. The particle's dimensions and the true size of the major face, which can only be identified from the projection with its principal axis of inertia parallel to the line of inspection, are hereby generally underestimated. III) The software analyzes the maximum and minimum Feret diameters (f_{max} and f_{min}) of each particle in each frame to calculate its aspect ratio. Although similar approaches have also been used to estimate particle shape distributions from inline imaging probes,[172] for the analysis of single faces of facetted crystals, using f_{min}/f_{max} of the crystal as aspect ratio is inadequate. As shown in Figure 35b, f_{max} correlates with the space diagonal of the particle, being substantially longer than the length of the largest crystal face. Depending on the respective projection, f_{min} will range from the thickness of the particle to its width, generally underestimating the aspect ratio of the largest face.

Therefore, the recorded sequences of images taken from QICPIC's video were analyzed via an in-house Matlab routine. The main improvements over standard image-processing algorithms are: I) the introduction of a particle tracking mechanism, II) the evaluation of particle length and width using an appropriately oriented bounding box resulting in more accurate sizing, III) the identification of the particle's thickness and IV) the implementation of a solidity filter to discard aggregates.

The ability to record a large number of images from different angles for each particle is a major advantage. However, not all the views are relevant for particle sizing purposes and it is important to yield only one single set of size and shape characteristics for every given particle. Therefore, our image analysis algorithm incorporates a particle tracking mechanism by which objects are followed across consecutive frames until they leave the field of vision. This allows many images of a particle to be assigned to that individual particle. The *Motion-based Multi Object Tracking* module[173] from Matlab®'s *Computer Vision System Toolbox™* was used as the basis for the particle tracking algorithm, although some modifications were introduced. In order to ensure that every crystal is well characterized, only objects that have been detected in N_{views} or more consecutive frames are included in the analysis. The value of the minimum number of views N_{views} is experimentally evaluated in the present work. Particles colliding or overlapping in the flow cell were removed from the analysis based on abrupt changes in particle size. Using trajectory prediction, overlapping particles are reassigned to their original track after diverging.

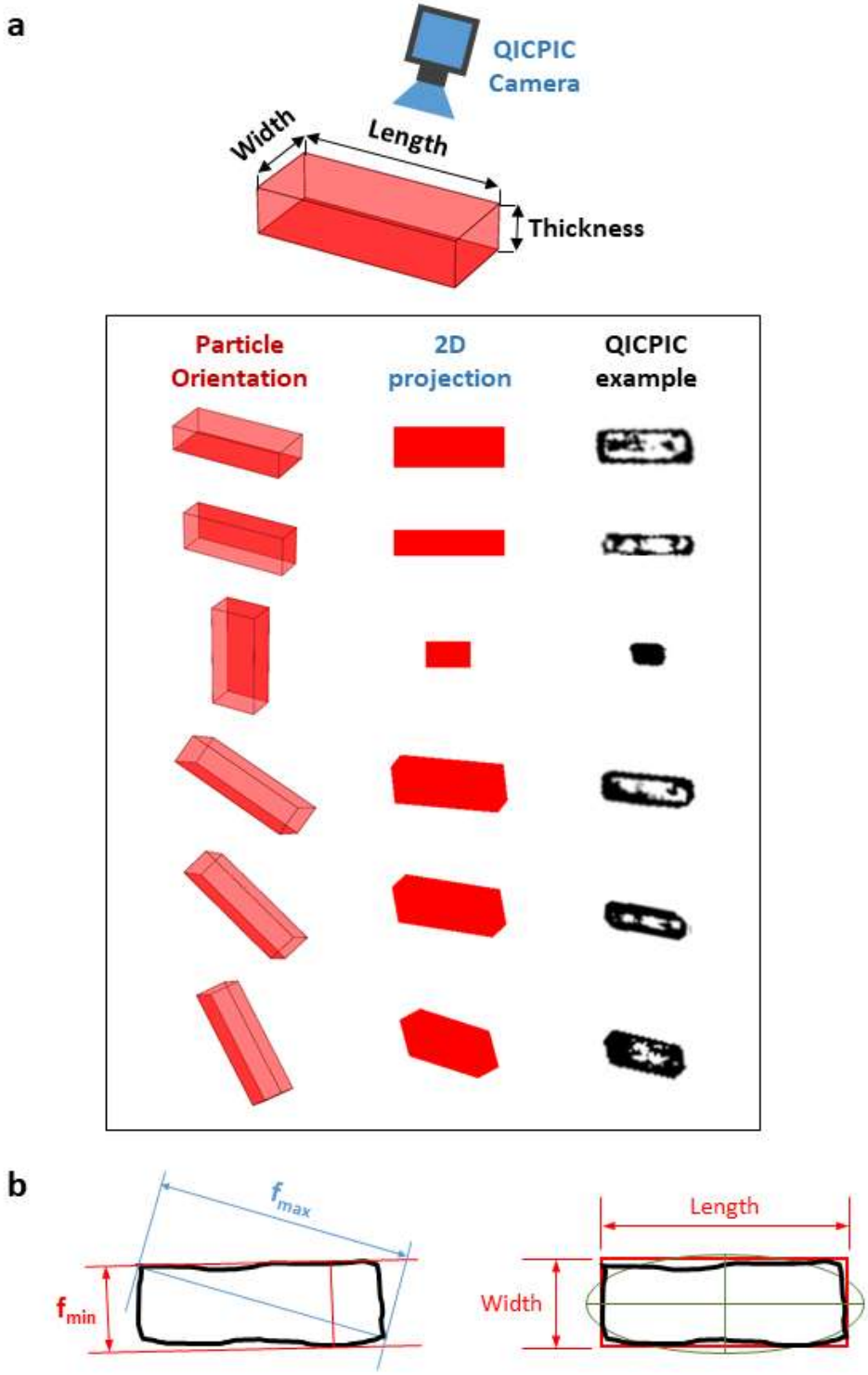

Figure 35: a) Illustration of multiple projections of the same particle depending on the orientation with respect to the plane of inspection of the camera, which is fixed at the top. One of the faces of the cuboid is shaded for easier visualization of the particle's rotation. Using particle tracking a single set of size characteristics is taken from all the projections observed. b) Scheme of the particle sizing algorithm utilizing length and width (right) instead of f_{min} and f_{max} (left) to measure the aspect ratio. The thickness is defined as the smallest width among all the projections of every individual particle.

In the present work, crystal habits range from rod-shaped to elongated cuboids and plate-like sheets. In order to make crystal dimensions comparable, all crystals were assumed to be cuboids, differing in length (longest dimension of the cuboid), width (second longest dimension) and thickness (shortest dimension), as shown in Figure 35a. However, the individual frames collected by the QICPIC instrument only contain 2D projections of the original three-dimensional particles. Generally, image analysis algorithms extract particle size and shape characteristics from these projections. A visual comparison of Sympatec's software particle sizing method and our approach is given in Figure 35b. In contrast to the original determination of the particle size via f_{max} and $f_{min,}$ the dimensions of the particles are established through appropriately oriented bounding boxes. The *regionprops* function[174] from Matlab® was used as an intermediary to establish the dimensions of each individual projection. The function operates through ellipse fitting, by which the center, size and orientation of an ellipse are optimized in order to achieve the representation that has the closest second moments as the particle (see Figure 35b). The length of the major and minor axes of the ellipse could be used as a measure of particle length and width. However, these axes are generally longer than the particle itself, as seen in Figure 35b. Instead, a bounding box around the particle with the same orientation as the ellipse is a more accurate representation. The length and width of the particles used in the present work correspond to the sides of this bounding box. The aspect ratio of the particle is calculated as the ratio of its width and its length. These size and shape characteristics of each particle are extracted from the projection with the largest area among the different views of this particle as it is tracked across several frames. This projection is more likely to correspond to the view of the particle with its central principal axis of inertia parallel to the line of inspection. Therefore, the resulting length and width will be the best representation of the actual dimensions of the particle. The area of the different projections can be determined by counting the number of pixels that form these objects and by then applying the corresponding transformation into physical dimensions using the known pixel size (i.e. 19.63 μm/pixel).

Using our particle tracking approach, not only the true size of the particle in terms of its length and width becomes accessible, but also its thickness can be determined being the smallest width found among the different projections observed for that particle. However, due to the measuring principle, the identification of the particle's thickness is most sensitive to capturing the projection aligned with the thickness facet, particularly in the case of plate-like particles, as is the case in this work. For crystals for which width and thickness are significantly different, the ratio of thickness to width – denominated T/W ratio in this work –

is a good indicator of the level of rotation of the particles. Values close to unity would imply that the particles do not revolve significantly and the same face is continuously exposed to the camera.

Another important feature incorporated in the algorithm is a solidity filter. The solidity of an object is defined as the ratio of the area of an object to the area of its convex hull. Typically, individual ASA crystals are not concave. Therefore, low solidity indicates the presence of concave parts of a structure, i.e., being a sign for particle aggregation or overlap. Previous studies[121,175] have used solidity filters to classify the particles in terms of their level of aggregation. According to those studies, the solidity threshold above which an absence of aggregation is assumed varies from 0.85 to 0.95. In our work, it was decided to discard any object with a solidity lower than 0.9.

Finally, to avoid the influence of fines on the results, only objects with an area larger than 50 square-pixels (length of 138.8 μm for objects of aspect ratio 1) are considered in the analysis. A filter is also applied to objects larger than 1600 square-pixels (length of 785.2 μm for objects of aspect ratio 1) to be sure that aggregates are not considered in the analysis.

4.3 *Results and Discussion*

This section presents the results obtained in this work. First, the importance of the particle tracking and aggregate rejection features included in our image analysis algorithm is demonstrated. Then, the influence of the number of cycles of growth and dissolution and the nature of the solvent on the particle size and shape distributions of the final product is analyzed. To ensure that the measured size and shape distributions are statistically representative, the analysis requires a minimum population of 500 particles.[176,177] Moreover, the reported distributions are the result of averaging three independent cycling experiments. The standard deviations of these averages are shown as error bars in the respective figures.

4.3.1 Importance of Particle Tracking and Aggregate Rejection

The high image acquisition rates of the QICPIC instrument provide the opportunity to observe several views of every individual particle as they transit through the flow cell. However, different particles move at different velocities depending on their position within the flow cell and their alignment with respect to the direction of the flow. Therefore, the slower particles are observed at more occasions and have a larger contribution toward size and shape distributions. In addition, the dimensions of the particles are only representative when the appropriate crystal face aligns with the camera inspection plane. Any tilt of the particle will result in views that might not correspond to an actual crystal face. Including the size and

shape of these elements in the analysis also alters the final size and shape distributions. Particle tracking avoids these statistical biases by reducing the contribution of each particle to a single set of features representing its true dimensions, allowing a more accurate characterization of the crystals. Figure 36 shows the influence of the particle tracking algorithm on the a) length and b) width number-based cumulative distributions of ASA in isopropanol, as well as on the c) aspect ratio distribution, where the aspect ratio of each particle is defined as the ratio of its width and length.

The raw size distributions (black lines), that include all possible views of each particle, shift to larger sizes when particle tracking is applied (blue lines). This is a consequence of discarding the length and width of tilted and smaller projections of the particle that do not correspond to the major crystal face. Similarly, the aspect ratio distribution also shifts to larger values since the effect of particle tracking on the particle width distribution is more significant than that on the particle length distribution.

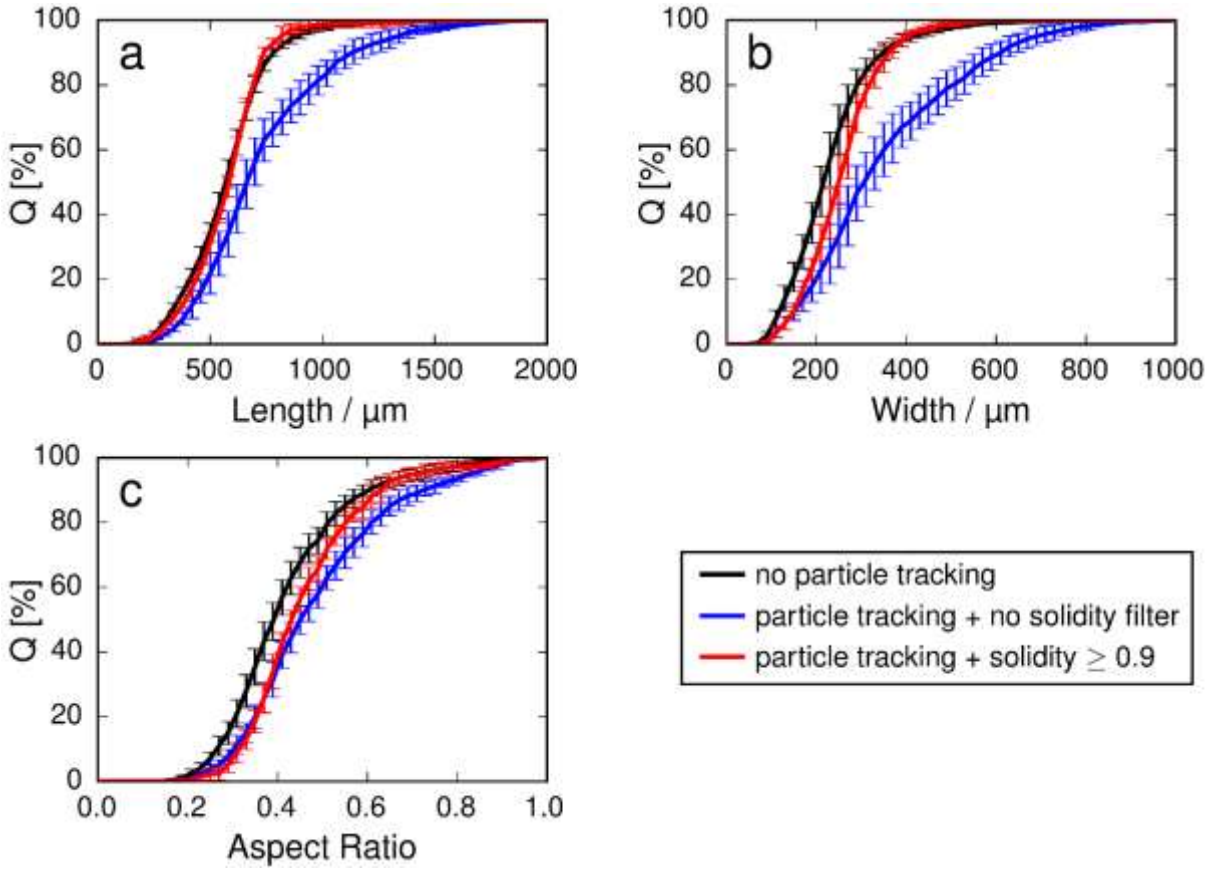

Figure 36: : Influence of the implementation of particle tracking and solidity filter on the number-based cumulative distribution of a) length, b) width and c) aspect ratio in shape tuning experiments of ASA in isopropanol after 25 cycles.

Depending on the revolving speed of the particles as they pass through the flow cell, the more views are recorded for each particle the more representative the measured dimensions of the particles will be since the alignment of the crystal's faces with the camera inspection plane will be more probable. In order to ensure the representability of the results, particles that are being tracked in only a minor number of frames are excluded from the analysis. Figure 37 shows how a distinct shift towards larger lengths and widths is observed as the minimum number of views required for each particle is increased. This shift continues until only particles with a minimum of 40 views (i.e., 40 pictures of the same particle in different orientations as it passes through the flow cell) are considered in the evaluation. Increasing the minimum number of views after this point does not yield a statistically significant change in length and width. Although the effect on the aspect ratio distribution is not critical (see Figure 37c), using only objects with at least 40 views ensured both a reliable measurement of the particles' dimensions and a minimum of 500 objects detected in each of our experiments.

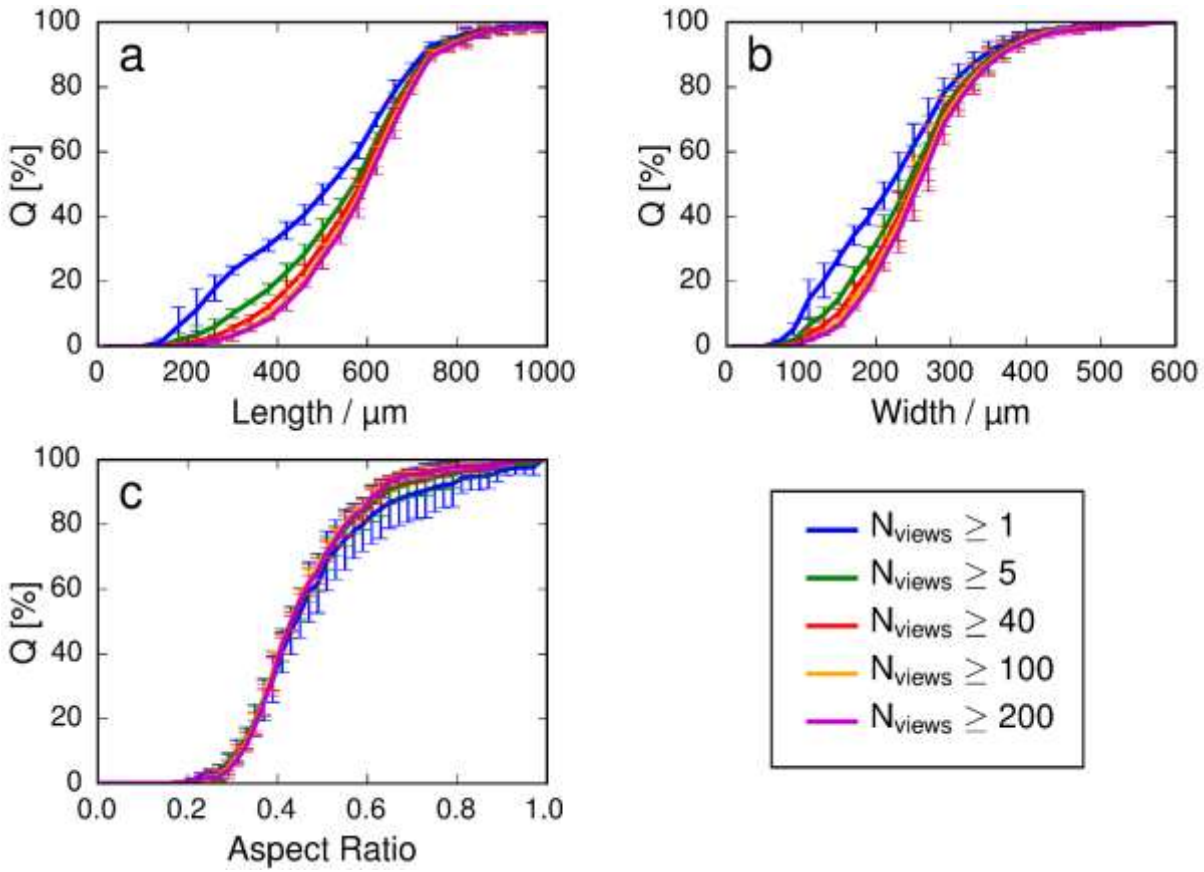

Figure 37: Influence of the minimum number of views of each individual particle on the number-based cumulative distribution (including the solidity filter) of a) length, b) width and c) aspect ratio in shape tuning experiments of ASA in isopropanol after 25 cycles.

Finally, aggregates of crystals and overlaps occurring during the particle's motion through the flow cell introduce a bias in particle size and shape measurements. As mentioned previously in Section 4.2.3, a solidity filter is incorporated in the image analysis algorithm to treat this issue. Figure 38 shows the distribution of solidity and length for all the particles detected in a shape tuning experiment of ASA in isopropanol. For individual particles, the solidity approaches the value of 1 while aggregates and overlaps, which generally present concavities, tend to have lower solidities. Effective implementation of a solidity filter with a threshold at solidity values of 0.9 allowed for discarding of these objects. As a consequence, the length and width distributions narrow down towards smaller and more representative sizes (shown as red lines in Figure 36a and Figure 36b). The aspect ratio distribution also shifts to lower values than that corresponding to the simple application of particle tracking (see Figure 36c). However, it still shows a significant increase with respect to the original results without particle tracking.

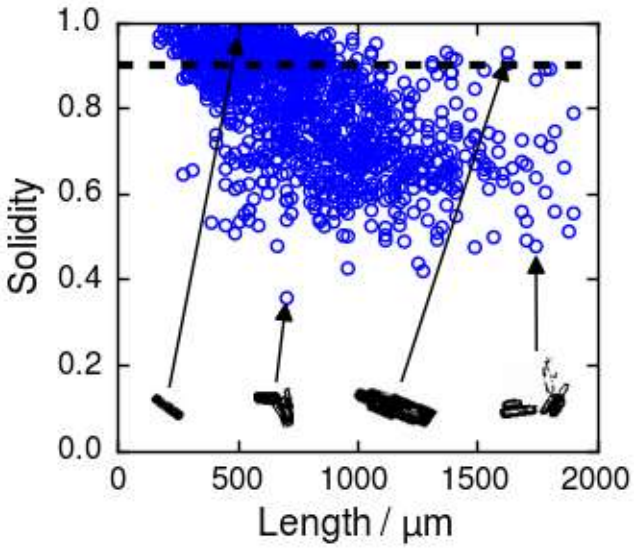

Figure 38: Scatter plot of solidity vs. length for product crystals after 25 cycles in isopropanol. The black dashed line corresponds to the solidity threshold applied in our analysis for the rejection of agglomerats and overlaps.

Both the particle tracking mechanism, as well as the solidity filter included in our algorithm have a significant influence on the particle size and aspect ratio distributions. This approach is applied to the results presented below since it provides the best representation of the crystal population.

4.3.2 Shape and Volume Changes of Crystals after Different Numbers of Cycles

The change of crystal shape of ASA crystals by temperature cycling in ethanol was investigated using an increasing number of cycles of growth and dissolution. Generally, during growth crystals evolve towards an equilibrium shape, which is in contrast to dissolution.[54] Thus, during cycles of growth and dissolution crystals do not asymptotically evolve towards a steady state shape but rather show a continuous change in shape.

Accordingly, due to the higher relative perpendicular growth rate of the (001) face compared to the (100) face the measured aspect ratio will reach a maximum when the major face becomes a square (see Figure 39Figure 42). If the cycling proceeds the width will become the longest dimension of the crystal and the aspect ratio will decrease again.

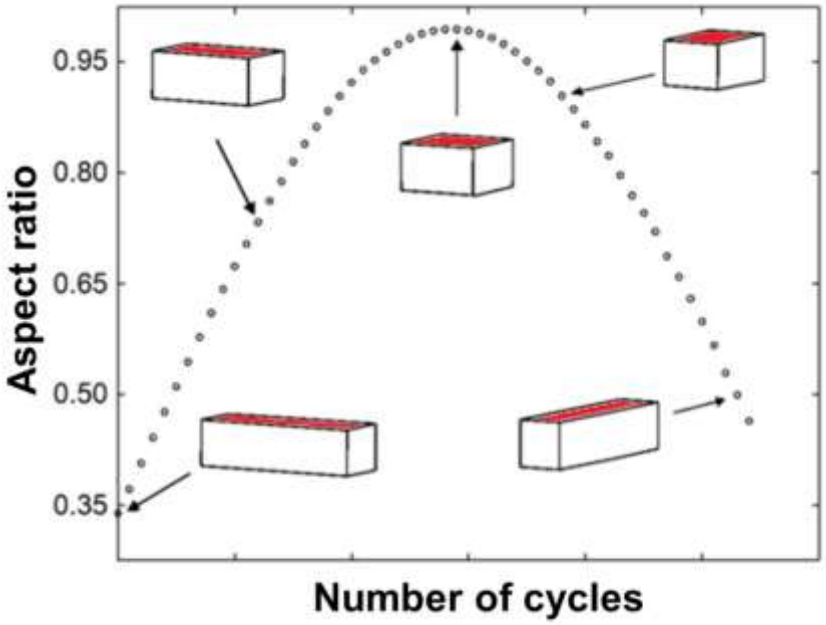

Figure 39: Development of the aspect ratio of the major (100) face (marked red) after each cycle of growth and dissolution. ASA crystals are assumed to have a cuboid habit with constant thickness (adapted from ref.21).

The results of our experiments varying the number of cycles between 5 and 25 are summarized in Figure 40 as number-based cumulative distributions of size, aspect ratio and thickness to width (T/W) ratio. While the length and width grow considerably with respect to the original ASA seeds after 25 cycles, during the initial ~5-10 cycles the length exhibits a distinct decrease and the width is not greatly affected, as shown in Figure 40a and Figure 40b, respectively. SEM images (Figure 41a) illustrate a high surface roughness on all sides of the seed crystals. This could induce an accelerated dissolution rate during the first cycles.

Following this overall shrinkage of the crystals, the results show strong growth of both the length and width after 15 cycles, corresponding to an anticipated overall increase in crystal volume for cycling in ethanol under the present conditions. The smooth surface of the crystals faces after this number of cycles, visualized by SEM in Figure 41b for the major (100) face is assumed to be responsible for the decrease in overall dissolution rate. Both the initial decrease in particle length for the first 5-10 cycles and the overall growth of the particle after 15-20 cycles (with a larger relative growth of particle width) result in an increase of aspect ratio, as shown in Figure 40d. The sample QICPIC images in Figure 40d show a clear transition from the rod-like seeds to plate-like crystals after 25 cycles, confirmed by the SEM images in Figure 41. Despite an initial decrease after 5 cycles, the particle thickness does not seem to be significantly affected by the consecutive cycles of growth and dissolution during the initial 20 cycles (see Figure 40c). However, a noticeable increase is observed after 25 cycles. It is possible that after an initial growth of the particle's width, further growth occurs in the direction perpendicular to the (100) face leading to larger particle thickness. The results shown in Figure 40e for the evolution of the T/W ratio with increasing number of cycles seem to confirm this hypothesis. Initially, the larger growth of the particle width with respect to its thickness, which even shrinks during the first 20 cycles, yields a decrease of the T/W ratio. After 25 cycles, the particles tend to grow in thickness rather than in width which results in an increase of the T/W ratio. However, the same effect would be observed if the rotation of the crystals within the LIXELL flow cell was somehow hindered and the thickness face was not accessible to the camera. The plate-like crystals formed after 25 cycles are more prone to a certain alignment with the flow than the initial rod-like particles which rotation is less impeded. The introduction of static mixers to promote turbulence within the flow could be a possible solution to discard particle alignment and confirm the results obtained after 25 cycles of growth and dissolution.

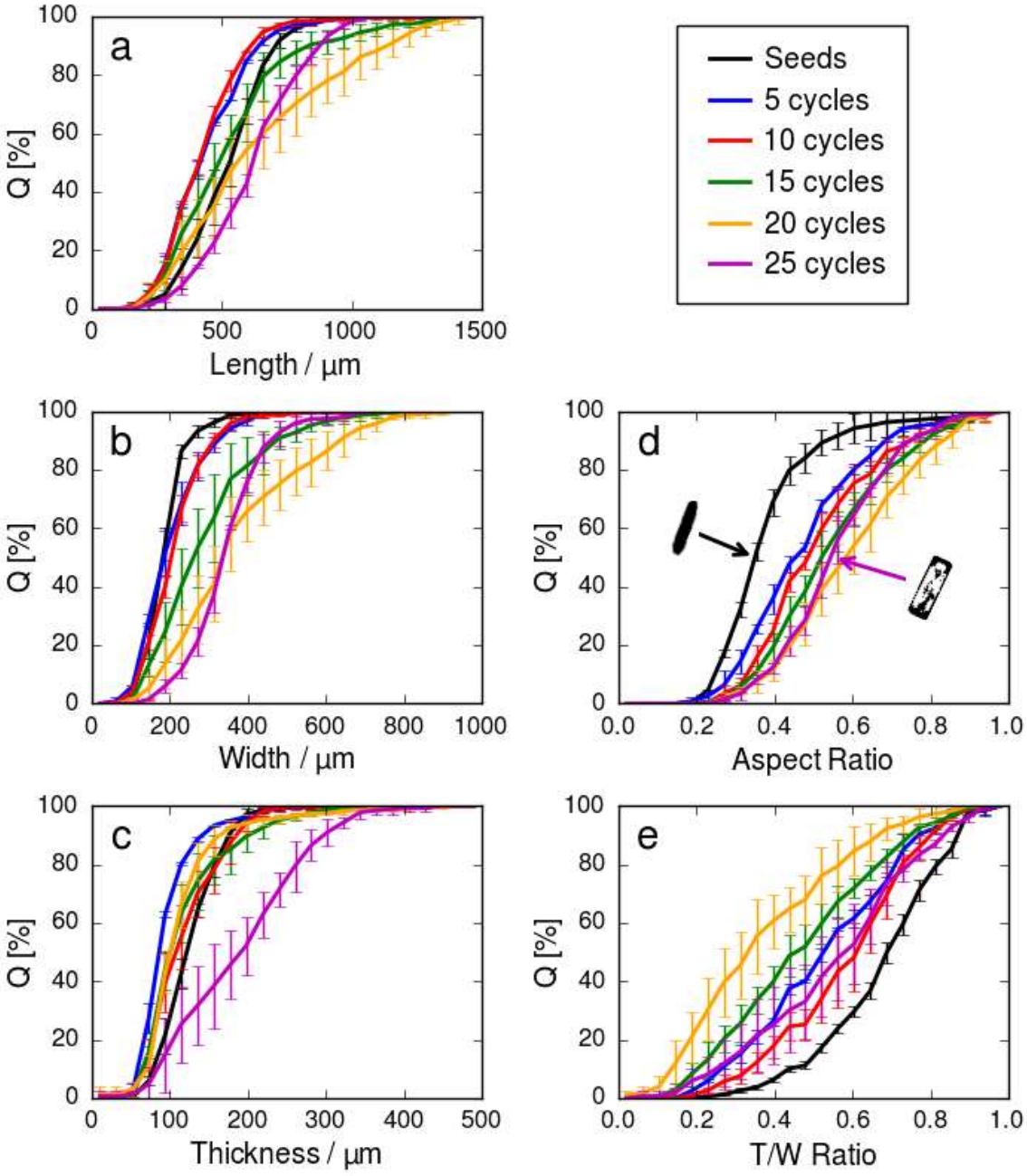

Figure 40: Influence of the number of cycles of growth and dissolution on the number-based cumulative distribution of a) length, b) width, c) thickness, d) aspect ratio and e) T/W ratio of ASA crystals suspended in ethanol.

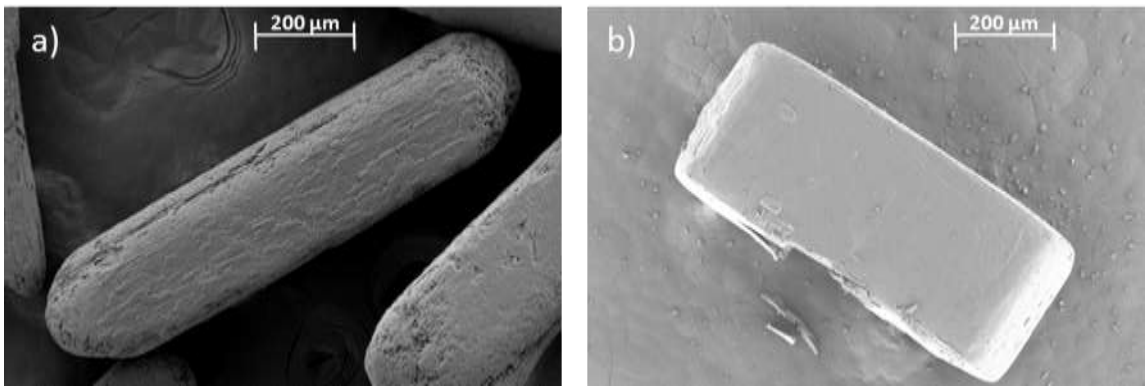

Figure 41: SEM images of a) seed and b) product crystal (after 25 cycles in ethanol). SEM: Zeiss Ultra 55, Zeiss, Oberkochen, Germany operated at 5 kV. Sputtering of particles with gold-palladium prior to analysis.

4.3.3 Solvent-influenced Shape Tuning

This section shows the results obtained for shape tuning experiments of ASA carried out in three different solvents (hexanol, isopropanol and ethanol). During these experiments, the suspensions underwent a total of 25 cycles of growth and dissolution between S_{max} = 1.23 and S_{min} = 0.89. The effect of the properties of the solvent on the final size and shape distributions of the product was studied by comparing the cycled crystals to the seeds.

The polarity of the solvent has a significant influence on the final product crystal's shapes. In order to ascribe resulting shapes after temperature cycling (considering the (100), (001) and (011) faces) to the respective solvent (and its polarity), other effects on crystal shape had to be minimized. On the one hand, during the dissolution steps the complete disappearance of one of the three groups of faces of interest was avoided by short residence times in each of the water baths. On the other hand, we assumed that growth on faces appearing on the crystal surface during dissolution by bifurcating from edges and vortices is much faster than on the faces of interest, insuring their rapid disappearance during regrowth. Also, if the same relative rates of growth and dissolution are present for each face, the final product will differ in the overall volume but each face will experience proportional growth maintaining its shape.

Figure 42 shows the results of the cycling experiments using the three different solvents (see Table 10 for their properites). As can be seen in Figure 42a and Figure 42b, for the polar solvent ethanol, both the length and width shift to larger sizes relative to the seed material. In addition, the aspect ratio distribution in Figure 42d shows a distinct shift to the right. This is equivalent to a larger relative increase in width, resulting from a major face appearing after

cycling the rod-like seeds in ethanol, as discussed in Section 4.3.2. Microscope images of a single product crystal were taken from three different angles (see Figure 43) and compared to the growth morphology of ASA (see Figure 31). Thus, the major face formed when cycling in ethanol was identified to be the (100) face. According to the shape of the seed material and the shape evolution during different numbers of cycles, changes in particle length are associated with the (011) face and net growth or dissolution on the (001) are associated with the crystal's width.

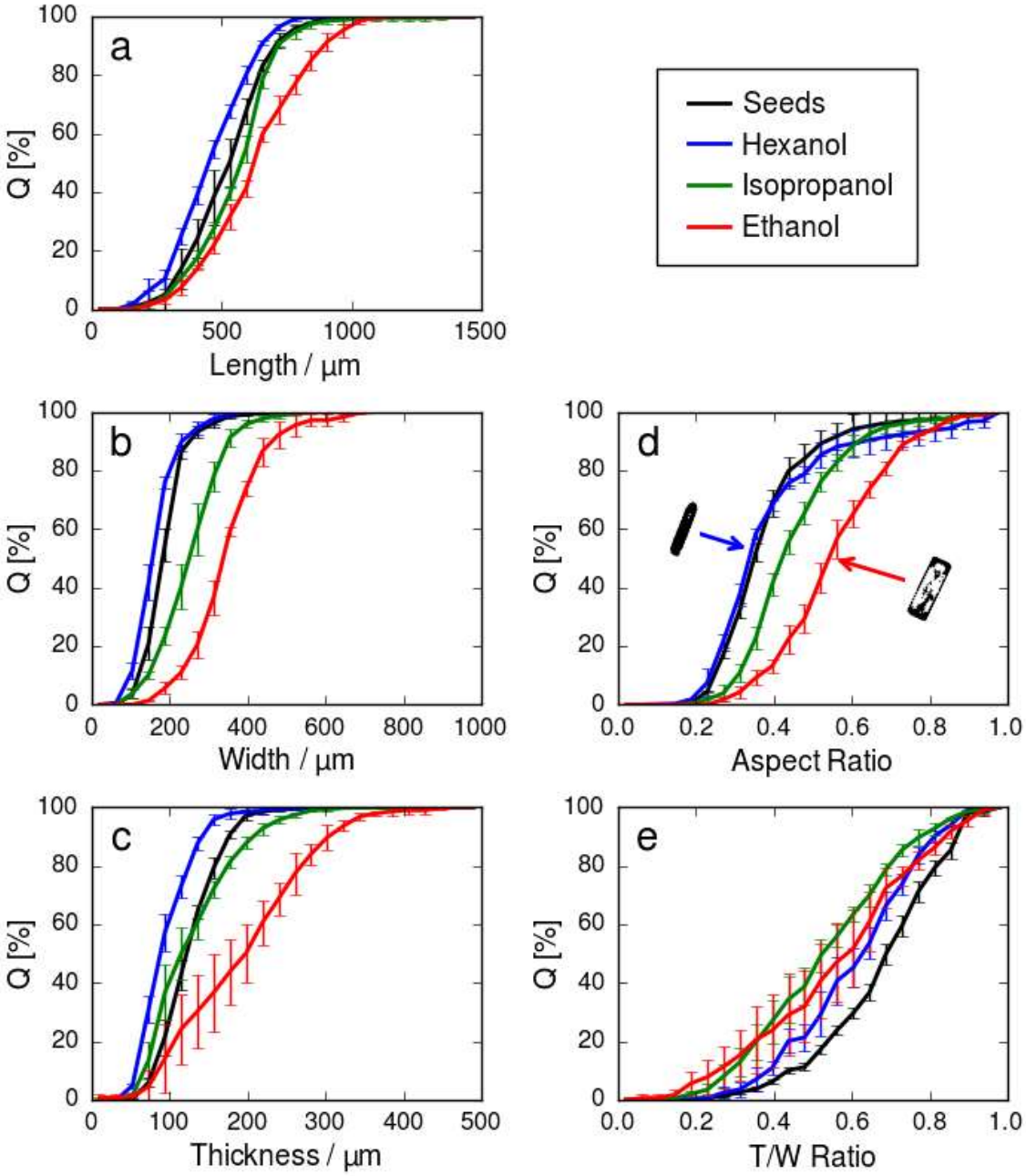

Figure 42: Influence of solvent-influenced shape tuning on the number-based cumulative distributions of a) length, b) width, c) thickness, d) aspect ratio and e) T/W ratio of ASA in different solvents.

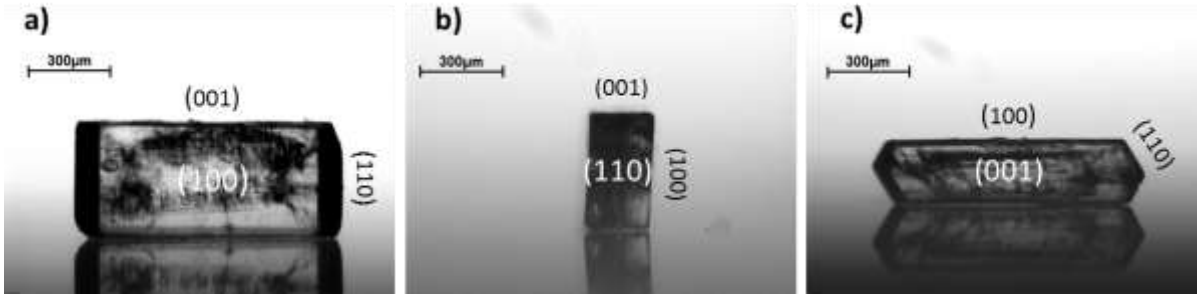

Figure 43: Horizontally taken microscope images of a single product crystal (length = 975 µm, width = 415 µm and thickness = 240 µm) temperature cycled in ethanol. The crystal is photographed with its principal axes of inertia parallel to the line of inspection, showing a) its (100) face, b) its (011) faces and c) its (001) face. Neighboring faces are indicated in black font. The faces could be assigned to their respective indices according to the relative position of the sloped (011) face.

Similar to ethanol, also for isopropanol a transformation to a plate-like habit was observed. The shift of the aspect ratio to the right is less pronounced and the length and width show less relative growth. This indicates that for both faces the perpendicular growth rates are less increased relative to their respective dissolution rates compared to ethanol. As the effect is still more pronounced for the (001) face, crystals evolve towards a plate-like shape. In contrast, for hexanol (the least polar solvent) the width, as well as the length, of the crystals decrease. This exhibits rates of growth being smaller than rates of dissolution for all three types of faces under the conditions chosen in this study. The (001) face shows a slightly more pronounced deceleration of the perpendicular growth rate, and therefore, crystals eventually tend to transform into more needle-like shapes. Therefore, the polarity of the solvent has a clear influence on the shape of ASA crystals, as observed in the QICPIC sample images in Figure 42d.

Assuming cuboid-like particles, their volume can be calculated via the product of length, width and thickness of the crystals. The accuracy, though, is limited by the number of different views captured by the camera for each particle, i.e. the different orientations accessible to the analysis. The more plate-like the crystals are, the more the calculation of the actual thickness and hence the volume depends on capturing the particle's smallest dimension which becomes less likely to be observed. According to the results presented in Figure 42c, the thickness of ASA particles suspended in hexanol decreases with respect to the original seeds after 25 cycles of growth and dissolution. The initial smoothing of the seeds observed during the first cycles when ethanol is used as a solvent, which translates in a reduction of particle thickness (see Figure 40c), might occur similarly in hexanol. However, this

phenomenon is not followed by growth rates higher than dissolution rates, as it was the case in ethanol, due to the less polar nature of hexanol. Therefore, the particles tend to shrink with respect to the original seeds. The results obtained using isopropanol as a solvent show again an intermediate behavior. After 25 cycles, the process in isopropanol appears to be in a phase where the relative growth on the (001) face is still more intense than the one on the (100) face, as suggested by the low T/W ratios observed in Figure 42e.

Concerning crystal volume distributions, results from our experiments show significant deviations of the product crystal with respect to the seeds, as observed in Figure 44. It is noted that the proposed approach can accurately estimate the width and the length of the crystals. However, thickness measurements are more sensitive to the angle of inspection and may impact the absolute measurement of volume. Nevertheless, the volume shifts can in part be explained by the effect of the solvents polarity-dependent growth rates and are in line with results obtained in molecular dynamics simulations[166]: In non-polar solvents ransition into a more needle-like shape is caused by, decelerated (re-)growth at the (001) surface rather than by accelerated growth at the (110) surface. Therefore, the overall volumetric growth rate of the crystals is expected to be smaller the less polar the solvent is. As dissolution rates are comparatively less affected by the solvent's polarity, imposing the same saturation trajectory for all solvents used in this study leads to different mean product crystal volumes.

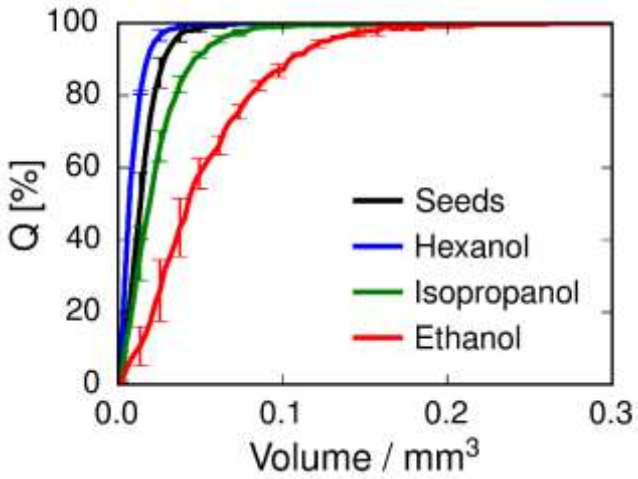

Figure 44: Number-based cumulative distribution of crystal volume V calculated via V= length×width×thickness for seed crystals and for product crystals after temperature cycling in different solvents.

It can be concluded, that in each solvent multiple faces of ASA show varying relative rates of growth and dissolution, offering a method to achieve target crystal habits that are not

accessible by growth alone. According to our results, particularly the (001) face is affected by the solvent polarity. Cycling in more polar solvents enhances growth on the (001) face in relation to its dissolution. Using rod-like seeds, this leads to an increase in particle's width. By using a less polar solvent (such as hexanol) the perpendicular growth on the (001) face can be minimized, resulting in a slow evolution towards a needle-like shape.

4.4 *Summary*

In the present study, a unique setup for rapidly altering saturation levels was developed. The system was shown to be able to change the shape of crystals via cycles of growth and dissolution. While the solvent factor is generally less important on dissolution of crystal faces, it has a strong impact on the face-specific incorporation of molecules during growth. Therefore, due to the (001) face of ASA crystals being most affected by the polarity, changes in crystal shape could be achieved using three different solvents.

While theoretical approaches and simulations of crystal shape changes via cycles of growth and dissolution deal with single particles, the present experimental work deals with distributions of sizes and shapes as are present in real-life manufacturing settings. Non-uniform starting material exhibiting differences in the presence and relative exposure of faces might cause a relevant variation in the product crystal shape. Particularly, for the dissolution rate, the volume and the specific surface area of the individual particles of a population are critical. While for one crystal a certain face might disappear completely (therefore becoming a virtual face) it is still present on the surface of another one. During re-growth, real and virtual faces show different perpendicular growth rates, resulting in broadening of the shape distribution.

We showed that rapid temperature cycling in different solvents can be a valuable mechanism for generating crystal shapes that are not obtainable through either growth or dissolution alone. By understanding the interplay between the face-specific functional groups and the solvents properties and its effect on the relative rates of growth and dissolution of single faces, the crystal shape can be tailored. Employing different solvents successively provides the opportunity to obtain virtually any convex shape for facetted crystals.

Due to their superior heat transfer properties tubular crystallizers are well suited for particle engineering, owing to the ability to rapidly change the temperature, a field of applications where conventional batch crystallizers quickly reach their operational limits.

While some of the resulting crystal shapes of ASA crystals obtained during this study might not reflect the typical requirements from industry concerning powder handling (e.g. flowability, filtration, capsule filling, tableting and further downstream processes), particles with increased specific surface area as is typical for plate-like crystals might be interesting for fast dissolution dosage forms. Furthermore, the presented setup can easily be adapted for other crystallization systems.

Based on an automated microscope, in the present study a particle imaging technique was established that allows assigning a large number of different projections to each single particle via particle tracking. Besides 2D characteristics, such as length and width, using our dedicated analysis routine facilitates the determination of the particle thickness and the associated derivative parameters, such as particle volume, sphericity and solidity, although its application is limited in the case of plate-like crystals as the analysis is highly sensitive on capturing the required projection. Improvement of our method could be achieved via increasing the fluid recirculation in the flow cell, enhancing the ability to take images with a higher number of orientations/projections. A static mixer installed at the entrance of the flow cell could increase the mixing, leading to enhanced revolving of the particles. This is promising regarding the identification of the true 3D habit of irregularly formed particles.

Furthermore, our setup could be used to change crystal shape by altering the saturation trajectory alone. However, experiments with this goal have shown that differences in the saturation trajectory large enough to achieve different relative rates are not feasible for ASA, due to limitations concerning the nucleation in the cold-water bath and complete dissolution in the warm-water bath.

5 Summary of Major Findings

The content of this thesis can be divided into two main sections: The first part addresses the continuous nucleation and crystallization of proteins, generally exhibiting particularly slow growth rates compared to crystals from small molecules. Building on prior work on continuous crystallization in this section a novel tubular crystallizer consisting of silicone tubing was described, having an overall length of 13 m and an inner diameter of 2 mm. Using segmented flow (g/l) a total linear flow rate of 1.9 mm/s was sufficient to facilitate efficient crystal transport while crystal growth rates remain high, similar to the level found in quiescent conditions. Lysozyme was chosen as a model protein and production rates of close to a gram per hour could be realized. By using water baths with various temperatures for supersaturation control, the nucleation zone of the crystallizer was separated from the growth zone where supersaturation was kept at S ≈ 8-5. Moreover, the solute's solubility could be controlled efficiently over a wide range.

Specifically, the main results of our work were:

- Lysozyme crystals of 15 - 40 µm with intact shapes were produced with a residence time of less than 2 hours in a continuous system.
- Production rates of 0.72 g/h were obtained.
- Shear forces inside the reactor proofed to be low enough to allow crystal growth at a high rate and crystal breakage was prohibited.
- Formation of amorphous precipitate was prevented during the process.

In the second section of this thesis a completely new approach for manipulating crystals was designed and tested.

The principle was based upon a tubular crystallizer with warmer and cooler zones to shift rapidly between dissolution and growth, via temperature cycling. A suspension of crystalline starting material suspended in its saturated solution was transported through a tubular reactor using a peristaltic pump. The tube was coiled up into loops, which were immersed into two water baths (compartments). The suspension was alternatingly cooled and heated in a defined way, i.e., the temperature difference and the residence time in each bath could be exactly tailored. Passing through the warmer compartment the suspension became undersaturated and crystals started to dissolve. Depending on the saturation level and the length of the tubing in this compartment, crystals dissolved to a desired size, before they entered the cooler compartment where the suspension became supersaturated. Here, recrystallization took place

on the existing crystals. Via a mass flow controller air bubbles were added to establish a segmented flow for enhanced particle transport. Settings were chosen in a way to allow growth of crystals without inducing primary nucleation. By varying the overall length of the crystallizer and by adjusting the temperature difference of the two compartments the results were tuneable according to desired specifications.

The main results of this part of the thesis were:

- While increasing the flow rates is an obvious choice for improving the dispersion of particles in the liquid segments separated by gas, also the wall film thickness increases with increasing flow rates. Crystals can pass from one slug to another via the wall film if sedimented crystals are of similar or smaller size compared to the film thickness. As the film thickness increases at higher flow rates, larger crystals might travel between slugs, despite the improved dispersion. The consequence is a broader residence time distribution (RSD) of particles.
- High average super- and undersaturations facilitated a more significant change in the CSD via rapid temperature cycling in the tubular crystallizer than via a single temperature cycle performed in batch. By varying the temperature difference in the water baths during different experiments, the number of fines decreased with increasing temperature differences. Simultaneously particles of more than 400 µm appeared in the product stream.
- By using the temperature cycling approach mixtures of mannitol's α- and β-polymorphs enriched in the more stable β-form of the substance. Raman microphotographs allowed identification of secondary nucleation of the β-form on the surface of α-form crystals, resulting in sea-urchin-like product particle shapes.
- In order to develop a tool for image analysis we extended the options provided by the QICPIC manufacturer, employing a particle tracking algorithm. Thereby, the statistical bias of considering the contribution of the different views of a single particle towards particle size and shape distributions could be avoided. Hence, an accurate identification of the crystals' thickness and true axis length was feasible, resulting in (cumulative) axis length distributions shifted towards larger sizes and being narrower.
- Concerning the polar solvent ethanol both the major and minor axis lengths shift to larger sizes relative to the starting seed material while also the aspect ratio distribution shows a distinct shift to the right. This is equivalent to a relative increase in width, resulting from a major face appearing after cycling the rod-like seeds in ethanol.

6 Outlook[e]

The first operational tubular crystallizer designs for continuous crystallization of active pharmaceutical ingredients were developed by the end of last decade; meanwhile, such systems have started to penetrate industry, such as the DN15 continuous oscillatory flow reactor developed and commercialized by NiTech Solutions®.[178]

However, current systems, while making it possible to continuously produce crystalline substance, have not been designed to enable scientists and companies to continuously engineer crystal properties. In the present work we successfully demonstrated that a continuous tubular reactor can be used in order to tailor particle properties. However, in future work two more quality attributes could be focused on to be optimized via our continuous crystallization system:

First, the shape of crystals is directly related to the handling of powders on the one hand, but also physicochemical properties, such as dissolution kinetics, catalytic properties and crystal stability due to chemical reactions, on the other one. Theoretical work by Snyder et al.[54] has shown the feasibility to optimize particle shape for specified purposes by using tailored temperature trajectories. In such investigations the focus could be placed on how to achieve desired shapes by variations of the temperatures in the warm and cold water bath and hence the saturation trajectory, keeping the solvent and the total seed crystal density constant. Since (perpendicular) face-specific growth rates depend on the level of supersaturation during growth, the crystal habit can be engineered during the growth stages by designed supersaturation profiles. Particularly the change from diffusion-limited growth at low supersaturation to surface-integration-limited growth at high supersaturation will likely change the growth mechanism of crystals, thereby extending the range of attainable variations in growth rates. Subsequent dissolution will be less effected by varitions in undersaturation, facilitating different relative face-specific rates of growth and dissolution.

Secondly, enantiomeric purity is another quality attribute, for which Viedma et al.[179] unraveled the underlying mechanism only a few years ago. Chirality, the presence of stereocenters in a molecule, impeding superimposability of image and mirror-image, plays a key role in nature. Although energetically equal, most natural compounds appear in a single

[e] The chapter 5 of this work is to some extend based on the FWF proposal Continuous Crystal Engineering in an Advanced Plug-Flow Crystallizer System' by Neugebauer, Khinast and Gruber-Wölfler. It has to be acknowledged that all parts included in this thesis were written by the author of this thesis.

enantiomeric form, e.g., life on earth utilizes only one type of amino acids (L-amino acids) and only one type of sugars (D-sugars). Accordingly, chirality is present in all proteins, enzymes, carbohydrates and nucleosides and in many alkaloids and hormones.[180] Today, also most active pharmaceutical ingredients (APIs) carry chiral centers, enabling the substance to be present in two (or more, depending on the number of chiral centers) different spatial arrangements. Due to the discriminative interaction between two chiral molecules, these APIs often show different pharmaceutical effects, depending on their respective chiral form. While one enantiomer shows the desired pharmaceutical activity, the other one might be far less effective, like for Ibuprofen (and other NSAID), or even harmful as was found for the case of Thalidomide. For racemically unresolved pharmaceuticals this either necessitates a higher drug dosage, thereby adding to the production costs, or might even prevent the drug from being marketed.

The driving mechanism for natural compounds appearing only in a single enantiomeric form was described only a few years ago and is also known as the process of "symmetry breaking".[179] This autocatalytic mechanism starts with crystals from a substance being able to racemize in its dissolved form. The prerequisite of the method is that enantiomers must crystallize as separate crystals, that is, a racemic conglomerate. Ostwald ripening, a process already known for more than 120 years[125] governs the reduction of overall crystal surface, eventually producing one single crystal, which in case of conglomerates, means enantiomeric purity. The rate of this process, though, is inversely proportional to the size of the crystals and therefore slows down extremely for macroscopic crystals. Repeated grinding of the crystals has shown to greatly accelerate this process. By inducing a slight enantio-imbalance the shift to a single solid chiral state can be directed, as the reincorporation of the clusters into crystals occurs more frequently for the "majority" crystalline population. By now, this mechanism has only been shown for batch processes.[181–183] Although symmetry breaking is limited to conglomerates and depends on racemization in the dissolved state, by establishing a robust continuous process this could help paving the way towards enantioselective pharmaceuticals.

In a proposed setup, shown in Figure 45, the temperature cycling approach is complemented with one crystallizer section in a temperature-regulated ultrasonic bath, which, besides cooling of the suspension, is employed to induce breakage of the crystals passing through the respective compartment. Depending on the hardness of the model compound different ultrasound intensities could be selected via designed experiments. For growth of the enantiopure product crystals to a desired size another crystallizer section in a water bath might be added at the end. A slight enantio-imbalance towards the desired enantiomer is required

before continuous temperature cycling and crushing could commence. Otherwise, due to the stochastic nature of the process, the undesired enantiomer might be produced. Therefore, a recycle stream should be included in the setup. Model substances during initial studies might be aspartic acid and the biologically relevant enantiomeric imine of 2-methyl-benzaldehyde and phenylglycinamide.

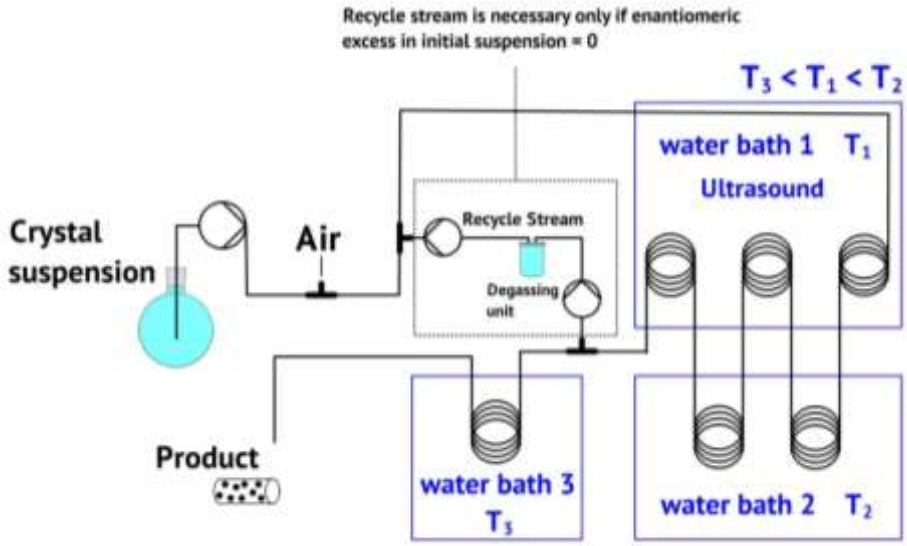

Figure 45: Schematic of a tubular setup for continuous temperature cycling and grinding via ultrasound

In summary, the benefits of such a system may be:

- Continuous engineering of crystalline particles with online monitoring and strict real-time quality control to produce crystals with desired properties regarding shape, enantiomeric form and/or fines content
- The ability to make products continuously that cannot be manufactured via simple growth from nuclei
- The absence of scale-up issues due to the possible parallelization of several tubular reactors, or scale up by increasing operational time. This is particularly relevant for use in the pharmaceutical industry were production rates are often “low”, in the range of liters (and grams) per hour. Robustness and long-term stability are important criteria for success in this context.
- As the temperature levels (baths) are kept at constant temperature the process will be highly economical. Since process models are developed in parallel to the experimental work, it may be easy to automate the system. Lastly, floor space is reduced, compared to batch processes with similar throughputs.

References

(1) Desiraju, G.; Vittal, J. J.; Ramanan, A. *Crystal engineering: a textbook*; World Scientific, 2011.

(2) Savjani, K. T.; Gajjar, A. K.; Savjani, J. K. Drug Solubility: Importance and Enhancement Techniques. *ISRN Pharm.* **2012**, 1–10.

(3) Blagden, N.; de Matas, M.; Gavan, P. T.; York, P. Crystal engineering of active pharmaceutical ingredients to improve solubility and dissolution rates. *Adv. Drug Deliv. Rev.* **2007**, *59*, 617–630.

(4) Modi, S. R.; Dantuluri, A. K. R.; Puri, V.; Pawar, Y. B.; Nandekar, P.; Sangamwar, A. T.; Perumalla, S. R.; Sun, C. C.; Bansal, A. K. Impact of Crystal Habit on Biopharmaceutical Performance of Celecoxib. *Cryst. Growth Des.* **2013**, *13*, 2824–2832.

(5) Besenhard, M. O.; Neugebauer, P.; Scheibelhofer, O.; Khinast, J. G. Crystal Engineering in Continuous Plug-Flow Crystallizers. *Cryst. Growth Des.* **2017**, *17*, 6432–6444.

(6) Protein Data Bank in Europe http://www.rcsb.org.

(7) Nanev, C. N. Protein crystal nucleation: Recent notions. *Cryst. Res. Technol.* **2007**, *42*, 4–12.

(8) Zang, Y.; Kammerer, B.; Eisenkolb, M.; Lohr, K.; Kiefer, H. Towards Protein Crystallization as a Process Step in Downstream Processing of Therapeutic Antibodies: Screening and Optimization at Microbatch Scale. *PLoS One* **2011**, *6*, 1–8.

(9) Margolin, A. L.; Navia, M. Proteinkristalle als neue Katalysatoren. *Angew. Chemie* **2001**, *113*, 2262–2281.

(10) Jegan Roy, J.; Emilia Abraham, T. Strategies in Making Cross-Linked Enzyme Crystals. *Chem. Rev.* **2004**, *104*, 3705–3722.

(11) Govardhan, C. P. Crosslinking of enzymes for improved stability and performance. *Curr. Opin. Biotechnol.* **1999**, *10*, 331–335.

(12) Basu, S. K.; Govardhan, C. P.; Jung, C. W.; Margolin, A. L. Protein crystals for the delivery of biopharmaceuticals. *Expert Opin. Biol. Ther.* **2004**, *4*, 301–317.

(13) Pechenov, S.; Shenoy, B.; Yang, M. X.; Basu, S. K.; Margolin, A. L. Injectable controlled release formulations incorporating protein crystals. *J. Control. release* **2004**, *96*, 149–158.

(14) Brange, J.; Langkjaer, L.; Havelund, S.; Volund, A. Chemical Stability of Insulin. 1. Hydrolytic Degradation During Storage of Pharmaceutical Preperations. *Pharm. Res.*

1992, *9*, 715–726.

(15) Shenoy, B.; Wang, Y.; Shan, W.; Margolin, A. L. Stability of Crystalline Proteins. *Biotechnol. Bioeng.* **2001**, *73*, 358–369.

(16) Clair, N.; Shenoy, B.; Jacob, L. D.; Margolin, A. L. Cross-linked protein crystals for vaccine delivery. *Proc. Natl. Acad. Sci. U. S. A.* **1999**, *96*, 9469–9474.

(17) Harrison, R. G.; Todd, P.; Rudge, S. R.; Petrides, D. P. *Bioseperations Science and Engineering*; Oxford University Press: New York, 2003.

(18) Pusey, M. L.; Witherow, W.; Naumann, R. Preliminary Investigations into Solutal Flow about Growing Tetragonal Lysozyme Crystals. *J. Cryst. Growth* **1988**, *90*, 105–111.

(19) Nyce, T.; Rosenberger, F. Growth of protein crystals suspended in a closed loop thermosyphon. *J. Cryst. Growth* **1991**, *110*, 52–59.

(20) Vekilov, P. G.; Rosenberger, F. Protein crystal growth under forced solution flow: experimental setup and general response of lysozyme. *J. Cryst. Growth* **1998**, *186*, 251–261.

(21) Durbin, S. D.; Feher, G. Crystal Growth Studies of Lysozyme as a Model for Protein Crystallization. *J. Cryst. Growth* **1986**, *76*, 583–592.

(22) Grant, M. L.; Saville, D. A. Long-term studies on tetragonal lysozyme crystals grown in quiescent and forced convection environments. *J. Cryst. Growth* **1995**, *153*, 42–54.

(23) Schmidt, S.; Havekost, D.; Kaiser, K.; Kauling, J.; Henzler, H.-J. Kristallisation für die Aufarbeitung von Proteinen. *Chemie Ing. Tech.* **2003**, *76*, 819–822.

(24) Smejkal, B.; Helk, B.; Rondeau, J.-M.; Anton, S.; Wilke, A.; Scheyerer, P.; Fries, J.; Hekmat, D.; Weuster-Botz, D. Protein Crystallization in Stirred Systems--Scale-Up Via the Maximum Local Energy Dissipation. *Biotechnol. Bioeng.* **2013**, *110*, 1956–1963.

(25) Howard, S. B.; Twigg, P.; Baird, J.; Meehan, E. The Solubility of Hen Egg-White Lysozyme. *J. Cryst. Growth* **1988**, *90*, 94–104.

(26) Forsythe, E. L.; Judge, R. A.; Pusey, M. L. Tetragonal Chicken Egg White Lysozyme Solubility in Sodium Chloride Solutions. *J. Chem. Eng. Data* **1999**, *44*, 637–640.

(27) Schall, C.; Riley, J.; Li, E.; Arnold, E.; Wiencek, J. Application of temperature control strategies to the growth of hen egg-white lysozyme crystals. *J. Cryst. Growth* **1996**, *165*, 299–307.

(28) Christopher, G. K.; Phipps, a. G.; Gray, R. J. Temperature-dependent solubility of selected proteins. *J. Cryst. Growth* **1998**, *191*, 820–826.

(29) Rosenberger, F.; Meehan, E. Control of Nucleation and Growth in Protein Crystal

Growth. *J. Cryst. Growth* **1988**, *90*, 74–78.

(30) DeMattei, R.; Feigelson, R. Thermal methods for crystallizing biological macromolecules. *J. Cryst. Growth* **1993**, *128*, 1225–1231.

(31) Astier, J.; Veesler, S. Using Temperature To Crystallize Proteins : A Mini-Review. *Cryst. Growth Des.* **2008**, *8*, 4215–4219.

(32) Jones, W. .; Wiencek, J.; Darcy, P. . Improvements in lysozyme crystal quality via temperature-controlled growth at low ionic strength. *J. Cryst. Growth* **2001**, *232*, 221–228.

(33) McPherson, A. *Preperation and Analysis of Protein Crystals*; Krieger: Malabar, 1989.

(34) Ries-Kautt, M.; Ducruix, A. *Crystallization of Nucleic Acids and Proteins*; Ducruix, A.; Giegé, R., Eds.; 2nd ed.; IRL Press: New York, 1992.

(35) Eder, R. J. P.; Schrank, S.; Besenhard, M. O.; Roblegg, E.; Gruber-Woelfler, H.; Khinast, J. G. Continuous Sonocrystallization of Acetylsalicylic Acid (ASA): Control of Crystal Size. *Cryst. Growth Des.* **2012**, *12*, 4733–4738.

(36) Besenhard, M. O.; Hohl, R.; Hodzic, A.; Eder, R. J. P.; Khinast, J. G. Modeling a seeded continuous crystallizer for the production of active pharmaceutical ingredients. *Cryst. Res. Technol.* **2014**, *49*, 92–108.

(37) Eder, R. J. P.; Radl, S.; Schmitt, E.; Innerhofer, S.; Maier, M.; Gruber-Woelfler, H.; Khinast, J. G. Continuously Seeded, Continuously Operated Tubular Crystallizer for the Production of Active Pharmaceutical Ingredients. *Cryst. Growth Des.* **2010**, *10*, 2247–2257.

(38) Eder, R. J. P.; Schmitt, E.; Grill, J.; Radl, S.; Gruber-Woelfler, H.; Khinast, J. G. Seed loading effects on the mean crystal size of acetylsalicylic acid in a continuous-flow crystallization device. *Cryst. Res. Technol.* **2011**, *46*, 227–237.

(39) Lorber, B. A versatile reactor for temperature controlled crystallization of biological macromolecules. *J. Cryst. Growth* **1992**, *122*, 168–175.

(40) Forsythe, E. L.; Ewing, F.; Pusey, M. L. Studies on Tetragonal Lysozyme Crystal Growth Rates. *Acta Crystallogr. D. Biol. Crystallogr.* **1994**, *50*, 614–619.

(41) Guilloteau, J.; Ries-Kautt, M.; Ducruix, A. Variation of lysozyme solubility as a function of temperature in the presence of organic and inorganic salts. *J. Cryst. Growth* **1992**, *122*, 223–230.

(42) Cacioppo, E.; Pusey, M. L. The solubility of the tetragonal form of hen egg white lysozyme from pH 4.0 to 5.4. *J. Cryst. Growth* **1991**, *114*, 286–292.

(43) Hekmat, D.; Hebel, D.; Schmid, H.; Weuster-Botz, D. Crystallization of lysozyme:

From vapor diffusion experiments to batch crystallization in agitated ml-scale vessels. *Process Biochem.* **2007**, *42*, 1649–1654.

(44) Forsythe, E. L.; Pusey, M. L. The effects of temperature and NaCl concentration on tetragonal lysozyme face growth rates. *J. Cryst. Growth* **1994**, *139*, 89–94.

(45) Pusey, M. L. An Apparatus for Protein Crystal Growth Studies. *Anal. Biochem.* **1986**, *158*, 50–54.

(46) Chang, B. S.; Yeung, B. Physical Stability of Protein Pharmaceuticals; In *Formulation and Process Development Strategies for Manufacturing Biopharmaceuticals*; Jameel, F.; Hershenson, S., Eds.; John Wiley & Sons, Inc.: New Jersey, 2010; pp. 69–104.

(47) DeFelippis, M. R.; Akers, M. J. *Pharmaceutical Formulation Development of Peptides and Proteins: Peptides and Proteins as Parenteral Suspensions: An Overview of Design, Development, and Manufacturing Considerations*; Hovgaard, L.; Frokjaer, S.; van de Weert, M., Eds.; CRC Press, 2012.

(48) Heng, J. Y. Y.; Bismarck, A.; Williams, D. R. Anisotropic Surface Chemistry of Crystalline Pharmaceutical Solids. *AAPS PharmSciTech* **2006**, *7*, E1–E9.

(49) Muster, T. H.; Prestidge, C. A. Face Specific Surface Properties of Pharmaceutical Crystals. *J. Pharm. Sci.* **2002**, *91*, 1432–1444.

(50) Danesh, A.; Connell, S. D.; Davies, M. C.; Roberts, C. J.; Tendler, S. J. B.; Williams, P. M.; Wilkins, M. J. An In Situ Dissolution Study of Aspirin Crystal Planes (100) and (001) by Atomic Force Microscopy. *Pharm. Res.* **2001**, *18*, 299–303.

(51) Roeffaers, M. B. J.; Sels, B. F.; Uji-I, H.; De Schryver, F. C.; Jacobs, P. a; De Vos, D. E.; Hofkens, J. Spatially resolved observation of crystal-face-dependent catalysis by single turnover counting. *Nature* **2006**, *439*, 572–575.

(52) Yu, K.; Schmidt, J. R. Elucidating the Crystal Face- and Hydration-Dependent Catalytic Activity of Hydrotalcites in Biodiesel Production. *J. Phys. Chem. C* **2011**, *115*, 1887–1898.

(53) Lovette, M. A.; Browning, A. R.; Griffin, D. W.; Sizemore, J. P.; Snyder, R. C.; Doherty, M. F. Crystal Shape Engineering. *Ind. Eng. Chem. Res.* **2008**, *47*, 9812–9833.

(54) Snyder, R. C.; Studener, S.; Doherty, M. F. Manipulation of Crystal Shape by Circles of Growth and Dissolution. *AIChE J.* **2007**, *53*, 1510–1517.

(55) Green, D. C.; Ihli, J.; Thornton, P. D.; Holden, M. A.; Marzec, B.; Kim, Y.-Y.; Kulak, A. N.; Levenstein, M. A.; Tang, C.; Lynch, C.; Webb, S. E. D.; Tynan, C. J.; Meldrum, F. C. 3D visualization of additive occlusion and tunable full-spectrum fluorescence in calcite. *Nat. Commun.* **2016**, *7*.

(56) Anwar, J.; Boateng, P. K.; Tamaki, R.; Odedra, S. Mode of action and design rules for additives that modulate crystal nucleation. *Angew. Chemie - Int. Ed.* **2009**, *48*, 1596–1600.

(57) Klapwijk, A. R.; Simone, E.; Nagy, Z. K.; Wilson, C. C. Tuning Crystal Morphology of Succinic Acid Using a Polymer Additive. *Cryst. Growth Des.* **2016**, *16*, 4349–4359.

(58) Besenhard, M. O.; Neugebauer, P.; Da-Ho, C.; Khinast, J. G. Crystal Size Control in a Continuous Tubular Crystallizer. *Cryst. Growth Des.* **2015**, *15*, 1683–1691.

(59) Pèrez-Calvo, J.-F.; Kadam, S. S.; Kramer, H. Determination of Kinetics in Batch Cooling Crystallization Processes - A Sequential Parameter Estimation Approach. *AIChE J.* **2016**, *62*, 3992–4012.

(60) Burns, M.; Natividad Marin, L.; Schneider, P. A. Investigations of a continuous Poiseuille flow struvite seed crystallizer - Mixer performance and aggregate disruption by sonication. *Chem. Eng. J.* **2016**, *295*, 552–562.

(61) Jiang, M.; Zhu, Z.; Jimenez, E.; Papageorgiou, C. D.; Waetzig, J.; Hardy, A.; Langston, M.; Braatz, R. D. Continuous-Flow Tubular Crystallization in Slugs Spontaneously Induced by Hydrodynamics. *Cryst. Growth Des.* **2014**, *14*, 851–860.

(62) Alvarez, A. J.; Myerson, A. S. Continuous Plug Flow Crystallization of Pharmaceutical Compounds. *Cryst. Growth Des.* **2010**, *10*, 2219–2228.

(63) Lawton, S.; Steele, G.; Shering, P.; Zhao, L.; Laird, I.; Ni, X. W. Continuous Crystallization of Pharmaceuticals Using a Continuous Oscillatory Baffled Crystallizer. *Org. Process Res. Dev.* **2009**, *13*, 1357–1363.

(64) Méndez Del Río, J. R.; Rousseau, R. W. Batch and Tubular-Batch Crystallization of Paracetamol: Crystal size Distribution and Polymorph Formation. *Cryst. Growth Des.* **2006**, *6*, 1407–1414.

(65) Neugebauer, P.; Khinast, J. G. Continuous Crystallization of Proteins in a Tubular Plug-Flow Crystallizer. *Cryst. Growth Des.* **2015**, *15*, 1089–1095.

(66) Wiedmeyer, V.; Anker, F.; Bartsch, C.; Voigt, A.; John, V.; Sundmacher, K. Continuous Crystallization in a Helically Coiled Tube: Analysis of Flow Field, Residence Time Behavior and Crystal Growth. *Ind. Eng. Chem. Reasearch* **2016**.

(67) McGlone, T.; Briggs, N. E. B.; Clark, C. A.; Brown, C. J.; Sefcik, J.; Florence, A. J. Oscillatory Flow Reactors (OFRs) for Continuous Manufacturing and Crystallization. *Org. Process Res. Dev.* **2015**, *19*, 1186–1202.

(68) Hohmann, L.; Gorny, R.; Klaas, O.; Ahlert, J.; Wohlgemuth, K.; Kockmann, N. Design of a Continuous Tubular Cooling Crystallizer for Process Development on Lab-Scale.

Chem. Eng. Technol. **2016**, *39*, 1268–1280.

(69) Roberge, D. M.; Ducry, L.; Bieler, N.; Cretton, P.; Zimmermann, B. Microreactor Technology: A Revolution for the Fine Chemical and Pharmaceutical Industries?. *Chem. Eng. Technol.* **2005**, *28*, 318–323.

(70) Rasche, M. L.; Jiang, M.; Braatz, R. D. Mathematical modeling and optimal design of multi-stage slug-flow crystallization. *Comput. Chem. Eng.* **2016**, *95*, 240–248.

(71) Rossi, D.; Jamshidi, R.; Saffari, N.; Kuhn, S.; Gavriilidis, A.; Mazzei, L. Continuous-Flow Sonocrystallization in Droplet-Based Microfluidics. *Cryst. Growth Des.* **2015**, *15*, 5519–5529.

(72) Angeli, P.; Gavriilidis, A. Hydrodynamics of Taylor flow in small channels: a review. *J. Mech. Eng. Sci.* **2008**, *222*, 737–751.

(73) Kawaji, M.; Mori, K.; Bolintineanu, D. The Effects of Inlet Geometry and Gas-Liquid Mixing on Two-Phase Flow in Microchannels. *J. Fluids Eng.* **2009**, *131*, 1–7.

(74) Rajesh, V. M.; Buwa, V. V. Experimental characterization of gas-liquid-liquid flows in T-junction microchannels. *Chem. Eng. J.* **2012**, *207–208*, 832–844.

(75) Yagodnitsyna, A. A.; Kovalev, A. V.; Bilsky, A. V. Flow patterns of immiscible liquid-liquid flow in a rectangular microchannel with T-junction. *Chem. Eng. J.* **2016**, *303*, 547–554.

(76) Kacker, R.; Regensburg, S. I.; Kramer, H. J. M. Residence time distribution of dispersed liquid and solid phase in a continuous oscillatory flow baffled crystallizer. *Chem. Eng. J.* **2017**, *317*, 413–423.

(77) Mandhane, J. M.; Gregory, G. A.; Aziz, K. A flow pattern map for gas-liquid flow in horizontal pipes. *Int. J. Multiph. Flow* **1974**, *1*, 537–553.

(78) Jayawardena, S. S.; Balakotaiah, V.; Witte, L. C. Flow Pattern Transition Maps for Microgravity Two-Phase Flows. *AIChE J.* **1997**, *43*, 1637–1640.

(79) Suo, M.; Griffith, P. Two-Phase Flow in Capillary Tubes. *J. Basic Eng.* **1964**, 576–582.

(80) Hewitt, G. F.; Roberts, D. N. *Studies of Two-Phase Flow Patterns by Simultaneous X-Ray and Flash Photography*; United Kingdom Atomic Energy Authority, 1969.

(81) Rezkallah, K. S. Weber number based flow-pattern maps for liquid-gas flows at microgravity. *Int. J. Multiph. Flow* **1996**, *22*, 1265–1270.

(82) El-Sebakhy, E. A. Flow regimes identification and liquid-holdup prediction in horizontal multiphase flow based on neuro-fuzzy inference systems. *Math. Comput. Simul.* **2010**, *80*, 1854–1866.

(83) Günther, A.; Kreutzer, M. T. *Micro Process Engineering, Vol. 1: Fundamentals,*

Operations and Catalysis; Hessel, V.; Renken, A.; Schouten, J. C.; Yoshida, J.-I., Eds.; WILEY-VCH Verlag GmbH & Co.: Weinheim, 2009.

(84) Liu, H.; Vandu, C. O.; Krishna, R. Hydrodynamics of Taylor Flow in Vertical Capillaries: Flow Regimes, Bubble Rise Velocity, Liquid Slug Length, and Pressure Drop. *Ind. Eng. Chem. Res.* **2005**, *44*, 4884–4897.

(85) Triplett, K. a.; Ghiaasiaan, S. M.; Abdel-Khalik, S. I.; Sadowski, D. L. Gas–liquid two-phase flow in microchannels Part I: two-phase flow patterns. *Int. J. Multiph. Flow* **1999**, *25*, 377–394.

(86) Jayanti, S.; Hewitt, G. F. Hydrodynamics and heat transfer in wavy annular gas-liquid flow: a computational fluid dynamics study. *Int. J. Heat Mass Transf.* **1997**, *40*, 2445–2460.

(87) Asadi, M.; Xie, G.; Sunden, B. A review of heat transfer and pressure drop characteristics of single and two-phase microchannels. *Int. J. Heat Mass Transf.* **2014**, *79*, 34–53.

(88) Tan, J.; Lu, Y. C.; Xu, J. H.; Luo, G. S. Mass transfer performance of gas-liquid segmented flow in microchannels. *Chem. Eng. J.* **2012**, *181–182*, 229–235.

(89) Kreutzer, M. T.; Kapteijn, F.; Moulijn, J. A.; Kleijn, C. R.; Heiszwolf, J. J. Inertial and interfacial effects on pressure drop of Taylor flow in capillaries. *AIChE J.* **2005**, *51*, 2428–2440.

(90) Irandoust, S.; Andersson, B. Liquid film in Taylor Flow through a Capillary. *Ind. Eng. Chem. Res.* **1989**, *28*, 1684–1688.

(91) Fairbrother, F.; Stubbs, A. E. 119. Studies in Electro-endosmosis. Part VI. The "Bubble-tube" Method of Measurement. *J. Chem. Soc.* **1935**, 527–529.

(92) Bretherton, F. P. The motion of long bubbles in tubes. *J. Fluid Mech.* **1961**, *12*, 166–188.

(93) Leung, S. S. Y.; Gupta, R.; Fletcher, D. F.; Haynes, B. S. Gravitational effect on Taylor flow in horizontal microchannels. *Chem. Eng. Sci.* **2012**, *69*, 553–564.

(94) Majumder, A.; Nagy, Z. K. Fines Removal in a Continuous Plug Flow Crystallizer by Optimal Spatial Temperature Profiles with Controlled Dissolution. *AIChE J.* **2013**, *59*, 4582–4594.

(95) Loï Mi Lung-Somarriba, B.; Moscosa-Santillan, M.; Porte, C.; Delacroix, a. Effect of seeded surface area on crystal size distribution in glycine batch cooling crystallization: a seeding methodology. *J. Cryst. Growth* **2004**, *270*, 624–632.

(96) Kim, S.; Wei, C.; Kiang, S. Crystallization Process Development of an Active

Pharmaceutical Ingredient and Particle Engineering via the Use of Ultrasonics and Temperature Cycling. *Org. Process Res. Dev.* **2003**, *7*, 997–1001.

(97) Saleemi, A.; Rielly, C. D.; Nagy, Z. K. Automated direct nucleation control for in situ dynamic fines removal in batch cooling crystallization. *CrystEngComm* **2012**, *14*, 2196–2203.

(98) Abu Bakar, M. R.; Nagy, Z. K.; Rielly, C. D. Seeded Batch Cooling Crystallization with Temperature Cycling for the Control of Size Uniformity and Polymorphic Purity of Sulfathiazole Crystals. *Org. Process Res. Dev.* **2009**, *13*, 1343–1356.

(99) Nagy, Z. K.; Aamir, E.; Rielly, C. D. Internal Fines Removal Using Population Balance Model Based Control of Crystal Size Distribution under Dissolution, Growth and Nucleation Mechanisms. *Cryst. Growth Des.* **2011**, *11*, 2205–2219.

(100) Kacker, R.; Radoiu, M.; Kramer, H. J. M. Novel design integrating a microwave applicator into a crystallizer for rapid temperature cycling . A direct nucleation control study. **2017**.

(101) Wu, Z.; Yang, S.; Wu, W. Application of temperature cycling for crystal quality control during crystallization. *CrystEngComm* **2016**, *18*, 2222–2238.

(102) Liu, J.; Rasmuson, Å. C. Influence of Agitation and Fluid Shear on Primary Nucleation in Solution. *Cryst. Growth Des.* **2013**, *13*, 4385–4394.

(103) Lakerveld, R.; Van Krochten, J. J. H.; Kramer, H. J. M. An air-lift crystallizer can suppress secondary nucleation at a higher supersaturation compared to a stirred crystallizer. *Cryst. Growth Des.* **2014**, *14*, 3264–3275.

(104) Lindenberg, C.; Krättli, M.; Cornel, J.; Mazzotti, M.; Brozio, J. Design and Optimization of a Combined Cooling/Antisolvent Crystallization Process. *Cryst. Growth Des.* **2009**, *9*, 1124–1136.

(105) Sarkar, D.; Rohani, S.; Jutan, A. Multiobjective Optimization of Semibatch Reactive Crystallization Processes. *AIChE J.* **2007**, *53*, 1164–1177.

(106) Sarkar, D.; Rohani, S.; Jutan, A. Multi-objective optimization of seeded batch crystallization processes. *Chem. Eng. Sci.* **2006**, *61*, 5282–5295.

(107) Noor, S.; Qamar, S. The space time CE/SE method for solving one-dimensional batch crystallization model with fines dissolution. *Chinese J. Chem. Eng.* **2015**, *23*, 337–341.

(108) Pantaraks, P.; Flood, A. E. Effect of Growth Rate History on Current Crystal Growth: A Second Look at Surface Effects on Crystal Growth Rates. *Cryst. Growth Des.* **2005**, *5*, 365–371.

(109) Mydlarz, J.; Jones, A. G. On the estimation of size-dependent crystal growth rate

functions in MSMPR crystallizers. *Chem. Eng. J. Biochem. Eng. J.* **1993**, *53*, 125–135.

(110) Iggland, M.; Mazzotti, M. Population Balance Modeling with Size-Dependent Solubility: Ostwald Ripening. *Cryst. Growth Des.* **2012**, *12*, 1489–1500.

(111) *Handbook of Industrial Crystallization*; Myerson, A. S., Ed.; Butterworth-Heinemann, 2002.

(112) Meenan, P. A.; Anderson, S. R.; Klug, D. L. The Influence of Impurities and solvents on crystallization; In *Handbook of Industrial Crystallization*; Elsevier B.V., 2002.

(113) Watanabe, A.; Yamaoka, Y.; Takada, K. Crystal Habits and Dissolution Behavior of Aspirin. *Chem. Pharm. Bull.* **1982**, *30*, 2958–2963.

(114) Jiang, M.; Zhu, X.; Molaro, M. C.; Rasche, M. L.; Zhang, H.; Chadwick, K.; Raimondo, D. M.; Kim, K. K. K.; Zhou, L.; Zhu, Z.; Wong, M. H.; O'Grady, D.; Hebrault, D.; Tedesco, J.; Braatz, R. D. Modification of Crystal Shape through Deep Temperature Cycling. *Ind. Eng. Chem. Res.* **2014**, *53*, 5325–5336.

(115) Bajcinca, N.; de Oliveira, V.; Borchert, C.; Raisch, J.; Sundmacher, K. Optimal control solutions for crystal shape manipulation. *Comput. Aided Chem. Eng.* **2010**, *28*, 751–756.

(116) Li, W.; Zhao, C.; Zou, B.; Zhang, X.; Yu, J.; Zhang, X.; Jie, J. Highly branched organic microcrystals via self-organization and growth kinetics manipulation. *CrystEngComm* **2012**, *14*, 8124.

(117) Patience, D. B.; Rawlings, J. B. Particle-shape Monitoring and Control in Crystallization Processes. *AIChE J.* **2001**, *9*, 2125–2030.

(118) Wang, X. Z.; Roberts, K. J.; Ma, C. Crystal growth measurement using 2D and 3D imaging and the perspectives for shape control. *Chem. Eng. Sci.* **2008**, *63*, 1173–1184.

(119) Simon, L. L.; Abbou Oucherif, K.; Nagy, Z. K.; Hungerbuhler, K. Bulk video imaging based multivariate image analysis, process control chart and acoustic signal assisted nucleation detection. *Chem. Eng. Sci.* **2010**, *65*, 4983–4995.

(120) Borchert, C.; Sundmacher, K. Morphology evolution of crystal populations: Modeling and observation analysis. *Chem. Eng. Sci.* **2012**, *70*, 87–98.

(121) Borchert, C.; Temmel, E.; Eisenschmidt, H.; Lorenz, H.; Seidel-Morgenstern, A.; Sundmacher, K. Image-Based in Situ Identification of Face Specific Crystal Growth Rates from Crystal Populations. *Cryst. Growth Des.* **2014**, *14*, 952–971.

(122) Kempkes, M.; Vetter, T.; Mazzotti, M. Monitoring the particle size and shape in the crystallization of paracetamol from water. *Chem. Eng. Res. Des.* **2010**, *88*, 447–454.

(123) Lee, E. H. A practical guide to pharmaceutical polymorph screening & selection. *Asian*

J. Pharm. Sci. **2014**, *9*, 163–175.

(124) Davey, R. J.; Back, K. R.; Sullivan, R. a. Crystal nucleation from solutions – transition states, rate determining steps and complexity. *Faraday Discuss.* **2015**, *179*, 9–26.

(125) Ostwald, W. Studien über die Bildung und Umwandlung fester Körper. *Zeitschirft für Phys. Chemie* **1897**, *22*, 289–330.

(126) Threlfall, T. Structural and Thermodynamic Explanations of Ostwald's Rule. *Org. Process Res. Dev.* **2003**, *7*, 1017–1027.

(127) Qu, H.; Louhi-Kultanen, M.; Rantanen, J.; Kallas, J. Solvent-Mediated Phase Transformation Kinetics of an Anhydrate/Hydrate System. *Cryst. Growth Des.* **2006**, *6*, 2053–2060.

(128) O'Sullivan, B.; Barrett, P.; Hsiao, G.; Carr, A.; Glennon, B. In Situ Monitoring of Polymorphic Transitions. *Org. Process Res. Dev.* **2003**, *7*, 977–982.

(129) Nguyen, D. L. T.; Kim, K. J. Solvent-Mediated Polymorphic Transformation of α-Taltirelin by Seeded Crystallization. *Chem. Eng. Technol.* **2016**, *39*, 1281–1288.

(130) Chow, K.; Tong, H. H. Y.; Lum, S.; Chow, A. H. L. Engineering of Pharmaceutical Materials: An Industrial Perspective. *J. Pharm. Sci.* **2008**, *97*, 2855–2877.

(131) O'Sullivan, B.; Glennon, B. Application of in Situ FBRM and ATR-FTIR to the Monitoring of the Polymorphic Transformation of D-Mannitol. *Org. Process Res. Dev.* **2005**, *9*, 884–889.

(132) Davey, R. J.; Guy, P. D.; Ruddick, A. J. The IV --> III Polymorphic Phase Transition in Aqueous Slurries of Ammonium Nitrate. *J. Colloid Interface Sci.* **1985**, *108*, 189–192.

(133) Botez, C. E.; Stephens, P. W.; Nunes, C.; Suryanarayanan, R. Crystal structure of anhydrous D-mannitol. *Powder Diffr.* **2003**, *18*, 214–218.

(134) Su, W.; Hao, H.; Glennon, B.; Barrett, M. Spontaneous Polymorphic Nucleation of D-Mannitol in Aqueous Solution Monitored with Raman Spectroscopy and FBRM. *Cryst. Growth Des.* **2013**, *13*, 5179–5187.

(135) Cornel, J.; Kidambi, P.; Mazzotti, M. Precipitation and transformation of the three polymorphs of d-mannitol. *Ind. Eng. Chem. Res.* **2010**, *49*, 5854–5862.

(136) Campbell Roberts, S. N.; Williams, A. C.; Grimsey, I. M.; Booth, S. W. Quantitative analysis of mannitol polymorphs. FT-Raman spectroscopy. *J. Pharm. Biomed. Anal.* **2002**, *28*, 1135–1147.

(137) Burger, A.; Henck, J. O.; Hetz, S.; Rollinger, J. M.; Weissnicht, A. a.; Stöttner, H. Energy/Temperature Diagram and Compression Behavior of the Polymorphs of D-

Mannitol. *J. Pharm. Sci.* **2000**, *89*, 457–468.

(138) Ohrem, H. L.; Schornick, E.; Kalivoda, A.; Ognibene, R. Why is mannitol becoming more and more popular as a pharmaceutical excipient in solid dosage forms?. *Pharm. Dev. Technol.* **2014**, *19*, 257–262.

(139) Wagner, C. M.; Pein, M.; Breitkreutz, J. Roll compaction of granulated mannitol grades and the unprocessed crystalline delta-polymorph. *Powder Technol.* **2015**, *270*, 470–475.

(140) Tao, J.; Jones, K. J.; Yu, L. Cross-Nucleation between D -Mannitol Polymorphs in Seeded Crystallization. *Cryst. Growth Des.* **2007**, *7*, 2410–2414.

(141) Speight, J. G. *Lange's Handbook of Chemistry*; 16th ed.; McGraw-Hill: New York, 2005.

(142) Maia, G.; Giulietti, M. Solubility of Acetylsalicylic Acid in Ethanol, Acetone, Propylene Glycol, and 2-Propanol. *J. Chem. Eng. Data* **2008**, *53*, 256–258.

(143) Kumar, S.; Ramkrishna, D. On the solution of population balance equations by discretization—I. A fixed pivot technique. *Chem. Eng. Sci.* **1996**, *51*, 1311–1332.

(144) Law, M.; Greene, L. E.; Johnson, J. C.; Saykally, R.; Yang, P. Nanowire dye-sensitized solar cells. *Nat. Mater.* **2005**, *4*, 455–459.

(145) Hammond, R. B.; Pencheva, K.; Roberts, K. J.; Auffret, T. Quantifying Solubility Enhancement Due to Particle Size Reduction and Crystal Habit Modification: Case Study of Acetyl Salicylic Acid. *J. Pharm. Sci.* **2007**, *96*, 1967–1973.

(146) Gressl, C.; Brunsteiner, M.; Davis, A.; Landis, M.; Pencheva, K.; Scrivens, G.; Sluggett, G. W.; Wood, G. P. F.; Gruber-Woelfler, H.; Khinast, J. G.; Paudel, A. Drug-Excipient Interactions in the Solid State: The Role of Different Stress Factors. *Mol. Pharm.* **2017**, *14*, 4560–4571.

(147) Hartman, P.; Perdok, W. G. On the relations between structure and morphology of crystals. I. *Acta Crystallogr.* **1955**, *8*, 49–52.

(148) Myerson, A. S.; Ginde, R. *Crystals, Crystal Growth, and Nucleation*; Butterworth-Heinemann: Boston, 1993.

(149) Winn, D.; Doherty, M. F. A new technique for predicting the shape of solution-grown organic crystals. *Aiche J.* **1998**, *44*, 2501–2514.

(150) Clydesdale, G.; Docherty, R.; Roberts, K. J. HABIT - a program for predicting the morphology of molecular crystals. *Comput. Phys. Commun.* **1991**, *64*, 311–328.

(151) Docherty, R.; Roberts, K. J.; Dowty, E. Morang - A computer program designed to aid in the determinations of crystal morphology. *Comput. Phys. Commun.* **1988**, *51*, 423–

430.

(152) Lahav, M.; Leiserowitz, L. The effect of solvent on crystal growth and morphology. *Chem. Eng. Sci.* **2001**, *56*, 2245–2253.

(153) Snyder, R. C.; Doherty, M. F. Faceted Crystal Shape Evolution During Dissolution or Growth. *AIChE J.* **2007**, *53*, 1337–1348.

(154) Zhang, Y.; Doherty, M. F. Simultaneous prediction of crystal shape and size for solution crystallization. *AIChE J.* **2004**, *50*, 2101–2112.

(155) Frank, F. C. On the kinematic theory of crystal growth and dissolution processes; In *Growth and Perfection of Crystals*; WILEY-VCH Verlag GmbH & Co.: New York, 1958; p. 411.

(156) Chernov, A. The Kinetics of the Growth Forms of Crystals. *Sov. physics, Crystallogr.* **1963**, *7*, 728–730.

(157) Burton, W. K.; Cabrera, N.; Frank, F. C. The Growth of Crystals and the Equilibrium Structure of their Surfaces. *Philos. Trans. R. Soc. A Math. Phys. Eng. Sci.* **1951**, *243*, 299–358.

(158) Davey, R. J. The role of the solvent in crystal growth from solution. *J. Cryst. Growth* **1986**, *76*, 637–644.

(159) Zhang, Y.; Sizemore, J. P.; Doherty, M. F. Shape Evolution of 3-Dimensional Faceted Crystals. *Aiche* **2006**, *52*, 1906–1915.

(160) Winn, D.; Doherty, M. F. Modeling crystal shapes of organic materials grown from solution. *AIChE J.* **2000**, *46*, 1348–1367.

(161) Lovette, M. A.; Muratore, M.; Doherty, M. F. Crystal Shape Modification Through Cycles of Dissolution and Growth: Attainable Regions and Experimental Validation. *AIChE J.* **2011**, *58*, 1465–1474.

(162) Aubrey-Medendorp, C.; Parkin, S.; Li, T. The Confusion of Indexing Aspirin Crystals. *J. Pharm. Sci.* **2008**, *97*, 1361–1367.

(163) Glasby, J.; Ridgeway, K. The crystallization of aspirin from ethanol. *J. Pharm. Pharmacol.* **1968**, *20*, 94–103.

(164) Danesh, A.; Davies, M. C.; Hinder, S. J.; Roberts, C. J.; Tendler, S. J. B.; Williams, P. M.; Wilkins, M. J. Surface Characterization of Aspirin Crystal Planes by Dynamic Chemical Force Microscopy. *Anal. Chem.* **2000**, *72*, 3419–3422.

(165) Heng, J. Y. Y.; Bismarck, A.; Lee, A. F.; Wilson, K.; Williams, D. R. Anisotropic Surface Chemistry of Aspirin Crystals. *J. Pharm. Sci.* **2007**, *96*, 2134–2144.

(166) Li, T.; Li, B.; Tomassone, M. S. Surface characterization of aspirin crystal planes using

molecular dynamics simulations. *Chem. Eng. Sci.* **2006**, *61*, 5159–5169.

(167) Eder, R. J. P.; Radl, S.; Schmitt, E.; Innerhofer, S.; Maier, M.; Gruber-Woelfler, H.; Khinast, J. G. Crystallization of APIs in a Continuously Seeded Tubular Crystallizer. *Sci. Pharm.* **2010**, *78*, 664.

(168) Besenhard, M. O.; Chaudhury, A.; Vetter, T.; Ramachandran, R.; Khinast, J. G. Evaluation of Parameter Estimation Methods for Crystallization Processes Modeled via Population Balance Equations. *Chem. Eng. Res. Des.* **2015**, *94*, 275–289.

(169) Eder, R. J. P.; Schmitt, E.; Radl, S.; Gruber-Woelfler, H.; Khinast, J. G. Kontinuierliches Wachstum von API Impf- zu Produktkristallen in einem Rohrkristallisator. *Chemie Ing. Tech.* **2010**, *82*, 1469–1470.

(170) Besenhard, M. O.; Thurnberger, A.; Hohl, R.; Faulhammer, E.; Rattenberger, J.; Khinast, J. G. Continuous API-crystal coating via coacervation in a tubular reactor. *Int. J. Pharm.* **2014**, *475*, 198–207.

(171) Eder, R. J. P.; Gruber-Woelfler, H.; Khinast, J. G. Kontinuierliche Kristallisation in einem Rohrkristallisator. *Chemie Ing. Tech.* **2009**, *81*, 1171–1171.

(172) Agimelen, O. S.; Jawor-Baczynska, A.; McGinty, J.; Dziewierz, J.; Tachtatzis, C.; Cleary, A.; Haley, I.; Michie, C.; Andonovic, I.; Sefcik, J.; Mulholland, A. J. Integration of in situ imaging and chord length distribution measurements for estimation of particle size and shape. *Chem. Eng. Sci.* **2016**, *144*, 87–100.

(173) The MathWorks, I. MATLAB® and Computer Vision System ToolboxTM Release 2016a, 2016.

(174) Matlab Regionprops Tool https://uk.mathworks.com/help/images/ref/regionprops.html.

(175) Borchert, C.; Sundmacher, K. Crystal aggregation in a flow tube: Image-based observation. *Chem. Eng. Technol.* **2011**, *34*, 545–556.

(176) Faria, N.; Pons, M. N.; Feyo de Azevedo, S.; Rocha, F. A.; Vivier, H. Quantification of the morphology of sucrose crystals by image analysis. *Powder Technol.* **2003**, *133*, 54–67.

(177) Ferreira, A.; Faria, N.; Rocha, F.; Teixeira, J. A. Using an online image analysis technique to characterize sucrose clystal morphology durring a crystallization run. *Ind. Eng. Chem. Reasearch* **2011**, *50*, 6990–7002.

(178) NiTech Solutions www.nitechsolutions.co.uk (accessed May 8, 2017).

(179) Viedma, C. Chiral symmetry breaking during crystallization: Complete chiral purity induced by nonlinear autocatalysis and recycling. *Phys. Rev. Lett.* **2005**, *94*, 3–6.

(180) Nguyen, L. A.; He, H.; Pham-Huy, C. Chiral drugs: an overview. *Int. J. Biomed. Sci.*

2006, *2*, 85–100.

(181) Noorduin, W. L.; Izumi, T.; Millemaggi, A.; Leeman, M.; Meekes, H.; Van Enckevort, W. J. P.; Kellogg, R. M.; Kaptein, B.; Vlieg, E.; Blackmond, D. G. Emergence of a single solid chiral state from a nearly racemic amino acid derivative. *J. Am. Chem. Soc.* **2008**, *130*, 1158–1159.

(182) Viedma, C.; Ortiz, J. E.; de Torres, T.; Izumi, T.; Blackmond, D. G. Evolution of solid phase homochirality for a proteinogenic amino acid. *J. Am. Chem. Soc.* **2008**, *130*, 15274–15275.

(183) Suwannasang, K.; Flood, A. E.; Coquerel, G. A Novel Design Approach to Scale Up the Temperature Cycle Enhanced Deracemization Process: Coupled Mixed-Suspension Vessels. *Cryst. Growth Des.* **2016**, *16*, 6461–6467.

THE END

7 Publications

Publications in refereed journals

- Neugebauer, P.; Khinast, J. G. Continuous Crystallization of Proteins in a Tubular Plug-Flow Crystallizer. Cryst. Growth Des. 2015, 15, 1089–1095.
- Besenhard, M. O.; Neugebauer, P.; Da-Ho, C.; Khinast, J. G. Crystal Size Control in a Continuous Tubular Crystallizer. Cryst. Growth Des. 2015, 15, 1683–1691.
- Neugebauer, P.; Besenhard, M. O.; Scheibelhofer, O.; Khinast, J. G. Crystal Engineering in Continuous Plug-Flow Crystallizers. Cryst. Growth Des. 2017, 17, 6432–6444.
- In preparation: Neugebauer, P.; Cardona, A.; et al. Crystal Shape Modification via Cycles of Growth and Dissolution in a Tubular Crystallizer

Diploma-thesis (supervised):

- A. Peter, Crystal Shape Tuning in a Continuously Operated Crystallization Process; P. Neugebauer, H. Gruber-Wölfler, Technische Universität Graz, Austria, 2017
- H. Cheng-Da, Implementation of a Feedback Control for a Continuous Tubular Crystallizer, P. Neugebauer, J. Khinast, Technische Universität Graz, Austria, 2015

Bachelor thesis and undergraduate thesis (supervised):

- T. Jagiello, The Polymorphism of Mannitol; P. Neugebauer, H. Gruber-Wölfler, Technische Universität Graz, Austria, 2017
- E. Gerstl, Partikeltracking von Acetylsalicylsäure-Kristallen mittels Matlab; P. Neugebauer, H. Gruber-Wölfler, Technische Universität Graz, Austria, 2017
- F. Moreno-Lavin, Qualitative and Quantitative Analysis of Crystals and Yield in Continuous Protein Crystallization, P. Neugebauer, J. Khinast, Technische Universität Graz, Austria, 2015
- P. Kelz, Protein Crystallization in a Tubular Plug-Flow Crystallizer and Possible Improvements, P. Neugebauer, J. Khinast, Technische Universität Graz, Austria, 2014
- K. Waldenhofer, Experimentelle Untersuchung von Abkühlraten unterschiedlicher Stoffsysteme unter Verwendung eines standardisierten Aufbaus und Validierung eines

Modells zur Beschreibung von Temperaturverläufen in Silikonschläuchen, P. Neugebauer, M. Besenhard. J. Khinast, Technische Universität Graz, Austria, 2016